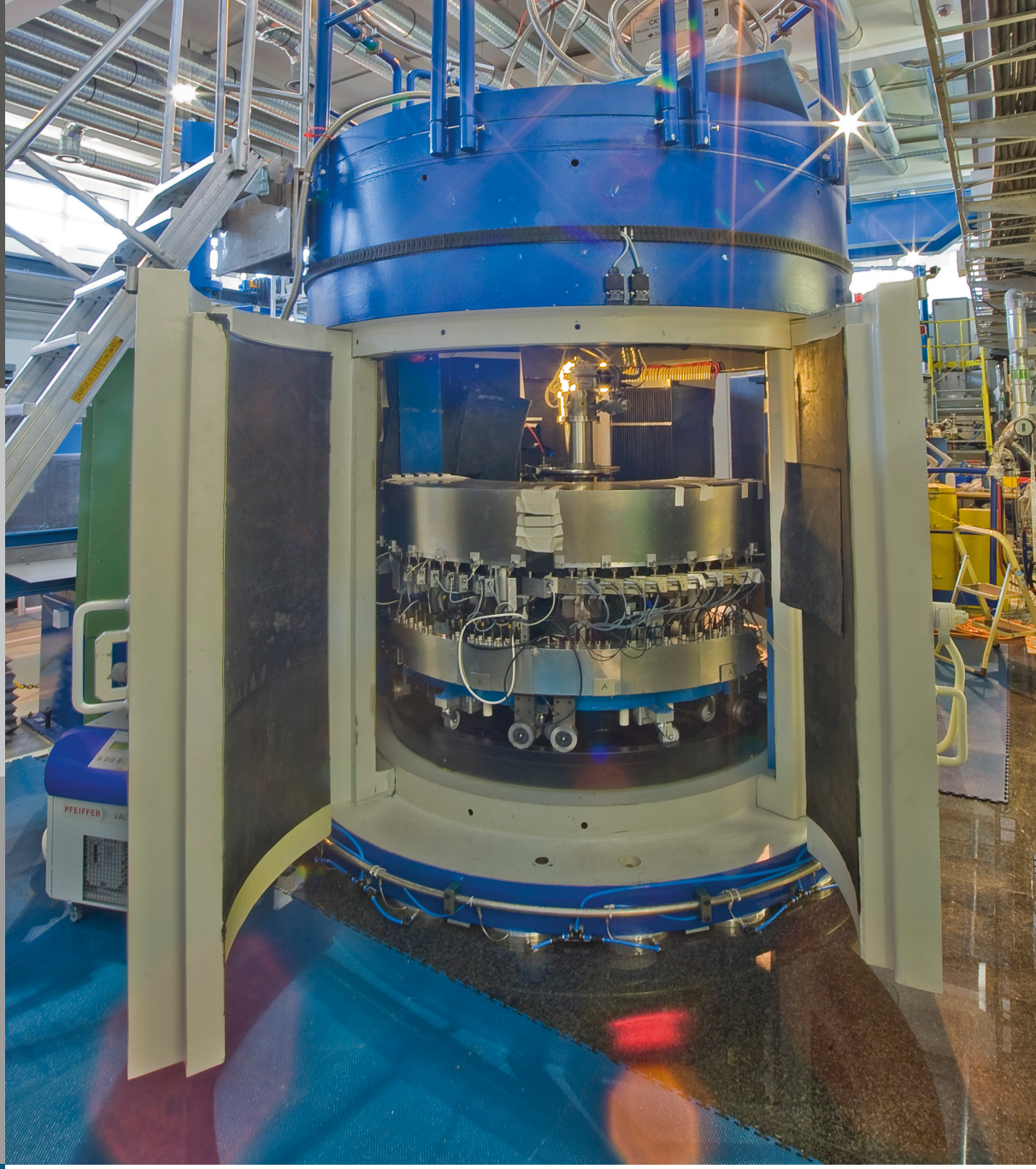

Laboratory Course

Neutron Scattering

Experiment Manuals

Thomas Brückel, Gernot Heger, Dieter Richter,
Georg Roth and Reiner Zorn (Editors)

RWTH Aachen
University Münster

JÜLICH
FORSCHUNGSZENTRUM

Member of the Helmholtz Association

Schriften des Forschungszentrums Jülich
Reihe Schlüsseltechnologien / Key Technologies Band / Volume 40

Forschungszentrum Jülich GmbH
Jülich Centre For Neutron Science (JCNS)

Thomas Brückel, Gernot Heger, Dieter Richter,
Georg Roth and Reiner Zorn (Editors)

Neutron Scattering

Experiment Manuals of the JCNS Laborator Course held at
Forschungszentrum Jülich and the research reactor
FRM II of TU Munich
In cooperation with
RWTH Aachen and University of Münster

Schriften des Forschungszentrums Jülich
Reihe Schlüsseltechnologien / Key Technologies Band / Volume 40

ISSN 1866-1807 ISBN 978-3-89336-790-0

Bibliographic information published by the Deutsche Nationalbibliothek.
The Deutsche Nationalbibliothek lists this publication in the Deutsche Nationalbibliografie; detailed bibliographic data are available in the Internet at http://dnb.d-nb.de.

Publisher and Distributor:	Forschungszentrum Jülich GmbH Zentralbibliothek 52425 Jülich Phone +49 (0) 24 61 61-53 68 · Fax +49 (0) 24 61 61-61 03 e-mail: zb-publikation@fz-juelich.de Internet: http://www.fz-juelich.de/zb
Cover Design:	Grafische Medien, Forschungszentrum Jülich GmbH
Printer:	Grafische Medien, Forschungszentrum Jülich GmbH
Copyright:	Forschungszentrum Jülich 2012

Schriften des Forschungszentrums Jülich
Reihe Schlüsseltechnologien / Key Technologies Band / Volume 40

ISSN 1866-1807
ISBN 978-3-89336-790-0

The complete volume ist freely available on the Internet on the Jülicher Open Access Server (JUWEL) at http://www.fz-juelich.de/zb/juwel

Contents

PUMA

Thermal Triple Axis Spectrometer

O. Sobolev, A. Teichert, N. Jünke

Forschungsneutronenquelle Heinz Maier-Leibnitz (FRM II)
Technische Universität München

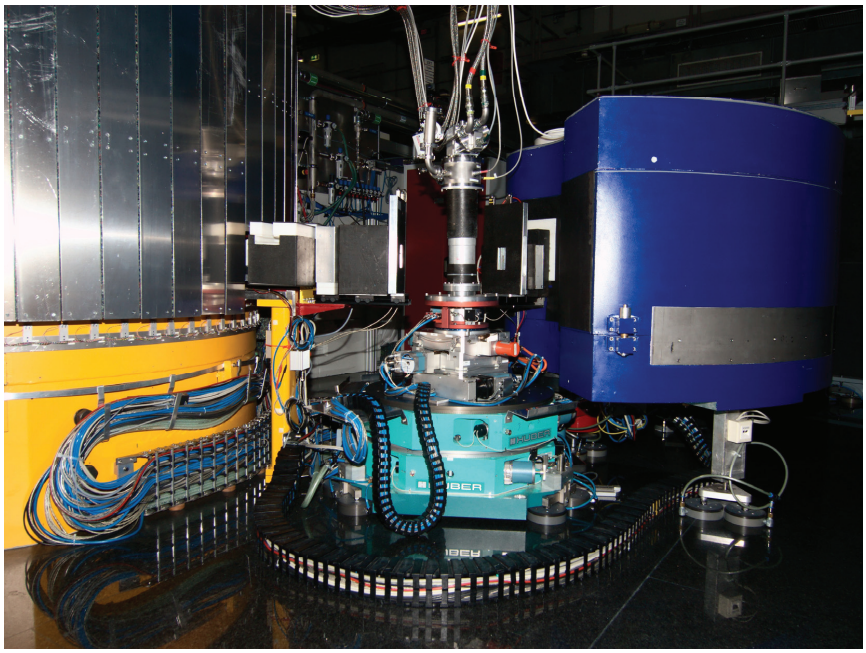

Manual of the JCNS Laboratory Course Neutron Scattering

Contents

1. Introduction

Excitations in crystals can be described using formalism of dispersion relations of the normal modes or quasi-particles (phonons, magnons, etc.). These relations contain the most detailed information on the intermolecular interactions in solids.

The result of a neutron scattering experiment is the distribution of neutrons that have undergone an energy exchange $\hbar\omega = E_i - E_f$, and a wave vector transfer, $\mathbf{Q} = \mathbf{k_i} - \mathbf{k_f}$, after scattering by the sample.:

$$\frac{\mathrm{d}^2\sigma}{\mathrm{d}\Omega \mathrm{d}\omega}(2\theta,\omega) = N\frac{k_f}{k_i}\left\{\frac{\sigma_{coh}}{4\pi}S_{coh}(\mathbf{Q},\omega)+\frac{\sigma_{inc}}{4\pi}S_{inc}(\mathbf{Q},\omega)\right\} \quad (1)$$

σ_{coh} is coherent scattering cross section, σ_{inc} is incoherent scattering cross section. They are constants that can be found in tables (http://www.ncnr.nist.gov/resources/n-lengths/). $S(\mathbf{Q},\omega)$ functions depend only on the structure and dynamics of the sample and do not depend on the interaction between neutrons and the sample. $S_{inc}(\mathbf{Q},\omega)$ reflects individual motions of atoms. $S_{coh}(\mathbf{Q},\omega)$ provides the information on the structure and collective excitations in the sample.

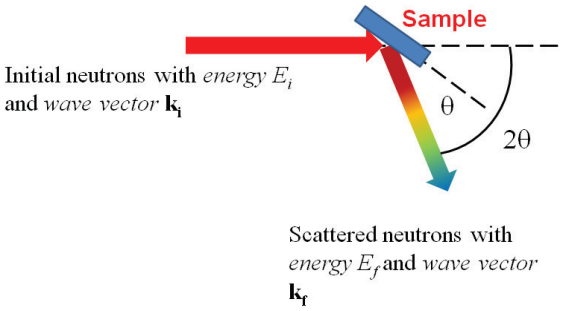

Energy transfer

$\hbar\omega = E_i - E_f$

Momentum transfer

$\mathbf{Q} = \mathbf{k_0} - \mathbf{k_f}$

$$k = \frac{\sqrt{2mE}}{\hbar} = \frac{2\pi}{\lambda}$$

$$Q = \sqrt{k_i^2 + k_f^2 - 2k_i k_f \cos 2\theta}$$

If $k_i = k_f$

$$Q = 2k_i \sin\theta = \frac{4\pi}{\lambda}\sin\theta$$

The triple axis spectrometer is designed for measuring the $S_{coh}(\mathbf{Q},\omega)$ in monocrystals. Therefore this function is of special interest for us.

2. Elastic scattering and Structure of Crystals

In the case of coherent *elastic scattering,* when $\omega = 0$ ($k_i = k_f$) only neutrons, that fulfill the Brags law are scattered by the sample:

$$n\lambda = 2d_{hkl}\sin\theta_{hkl}, \tag{2}$$

where λ is a wavelength of neutron, d_{hkl} is a distance between crystal planes described by corresponding Miller indexes *hkl*. θ_{hkl} denotes the angle between incoming (outgoing) scattering beam and the (hkl) plane.

For the analysis of the scattering processes in crystals it is convenient to use the concept of the *reciprocal space*. For an infinite three dimensional lattice, defined by its primitive vectors $\boldsymbol{a_1}$, $\boldsymbol{a_2}$ and $\boldsymbol{a_3}$, its reciprocal lattice can be determined by generating three reciprocal primitive vectors, through the formulae:

$$\begin{aligned}
\mathbf{g}_1 &= 2\pi \frac{\mathbf{a}_2 \times \mathbf{a}_3}{\mathbf{a}_1 \cdot \mathbf{a}_2 \times \mathbf{a}_3} \\
\mathbf{g}_2 &= 2\pi \frac{\mathbf{a}_1 \times \mathbf{a}_3}{\mathbf{a}_2 \cdot \mathbf{a}_1 \times \mathbf{a}_3} \\
\mathbf{g}_3 &= 2\pi \frac{\mathbf{a}_1 \times \mathbf{a}_2}{\mathbf{a}_3 \cdot \mathbf{a}_1 \times \mathbf{a}_2}
\end{aligned} \tag{3}$$

Note the denominator is the scalar triple product. Geometrically, the scalar triple product $\mathbf{a_1(a_2 \times a_3)}$ is the volume of the parallelepiped defined by the three vectors.

Let us imagine the lattice of points given by the vectors $\mathbf{g_1}$, $\mathbf{g_2}$ and $\mathbf{g_3}$ such that $\boldsymbol{\tau}$ is an arbitrary linear combination of these vectors:

$$\boldsymbol{\tau} = h\mathbf{g}_1 + k\mathbf{g}_2 + l\mathbf{g}_3\,, \tag{4}$$

where *h,k,l* are integers. Every point of the reciprocal lattice, characterized by $\boldsymbol{\tau}$ corresponds in the position space to the equidistant set of planes with Miller indices (*h,k,l*) perpendicular to the vector $\boldsymbol{\tau}$. These planes are separated by the distance

$$d_{hkl} = \frac{2\pi}{\left|\boldsymbol{\tau}_{hkl}\right|} \tag{6}$$

The Brag's condition for diffraction can be expressed in the following vector form:

$$\mathbf{Q} = \boldsymbol{\tau}_{hkl} \tag{7}$$

A useful construction for work with wave vectors in reciprocal space is the Brillouin zone (BZ). The BZ is the smallest unit in reciprocal space over which physical quantities such as phonon or electron dispersions repeat themselves. It is constructed by drawing vectors from one reciprocal lattice points to another and then constructing lines perpendicular to these vectors at the midpoints. The smallest enclosed volume is the BZ.

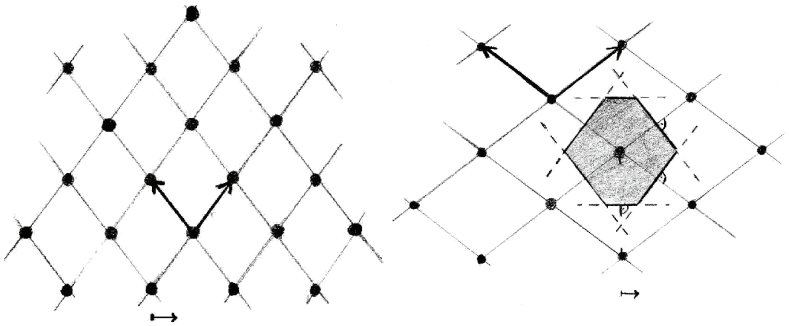

Fig.1 Real (left) and reciprocal (right) two dimensional lattices and BZ (gray area)

3. Inelastic Neutron Scattering and Phonons

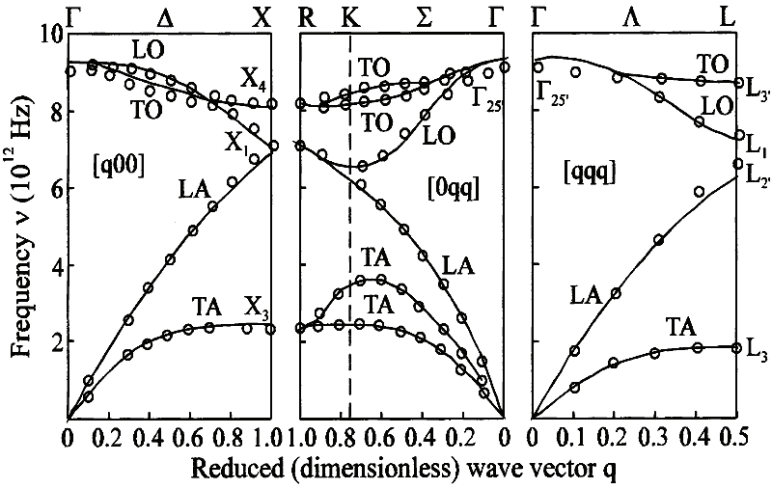

Fig.2 Phonon dispersion curves for Ge.

Atomic vibrations in a crystal can be analyzed in terms of lattice waves which are the normal modes of the crystal. The frequencies of normal modes ω are related to their wave vectors $\mathbf{q}$ ($q = 2\pi/\lambda$) by the dispersion relations

$$\omega = \omega_j(\mathbf{q}), \tag{7}$$

where the index j denotes a particular branch. For a crystal with N atoms per primitive unit cell there are $3N$ branches of the frequency spectrum. Three branches are acoustic ones for which $\omega \to 0$ as $\mathbf{q} \to 0$; the other $3N$-3 are branches are optical branches for which ω tends to a finite value as $\mathbf{q} \to 0$. In certain directions of high symmetry the normal vibrations are strictly transverse or longitudinal. The energy quantum $\hbar\omega$ is called *phonon* in analogy to the phonon for electromagnetic waves.

If we want to measure the frequency of a phonon ω for a certain **q**, the basic scattering conditions must fulfil the energy and momentum conservation laws:

$$E_i - E_f = \frac{\hbar}{2m_n}(k_i^2 - k_f^2) = \pm\hbar\omega(\mathbf{q}) \qquad (9)$$

$$\mathbf{Q} = \mathbf{k_i} - \mathbf{k_f} = \mathbf{G} \pm \mathbf{q}$$

When the above conditions are fulfilled, the function $S_{coh}(\mathbf{Q},\omega)$ shows a peak. We can held **Q** constant and vary $\mathbf{k_i}$ ($\mathbf{k_f}$) to measure intensity of scattered neutrons at different energy transfers. In order to keep **Q**, and thus **q**, constant while varying $\mathbf{k_i}$, the scattering angle must change as well as the relative orientation of the crystal with respect to $\mathbf{k_f}$.

The intensity of neutrons scattered by phonon is proportional to the square of the dynamical structure factor $F(\mathbf{Q})$:

$$S_{coh}(\mathbf{Q},\omega) \sim |F(\mathbf{Q})|^2 = \left|\sum_\kappa b_\kappa \frac{\mathbf{Q}\cdot\mathbf{e}_\kappa(\mathbf{q}_j)}{\sqrt{m_\kappa}} \exp(-W_k)\exp(-i\mathbf{q}\mathbf{r}_\kappa)\right|^2, \qquad (10)$$

Where sum is taken over all atoms in unit cell with coordinates $\mathbf{r}_k$, exp(-W) is a Debye-Waller factor, $\mathbf{e}_k$ denotes the polarization vector of the phonon. The scalar product $\mathbf{Q}\cdot\mathbf{e}_\kappa(\mathbf{q}_j)$ means that only lattice vibrations polarized along the momentum transfer are visible. This makes possible to distinguish transverse (TA) and longitudinal (LA) acoustic modes. For TA modes $\mathbf{e}\perp\mathbf{q}$, and therefore **Q** must be perpendicular to **q**, while for a LA mode, one must take $\mathbf{Q} \,||\, \mathbf{q}$ (Fig. 3)

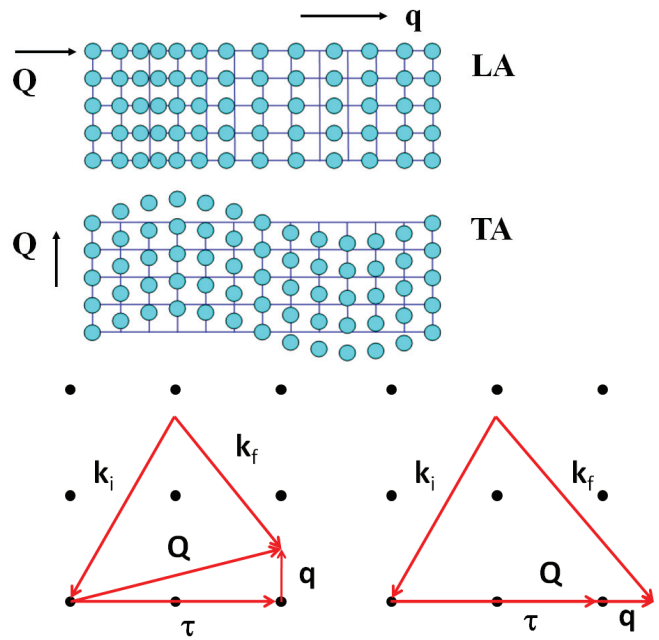

Fig. 3 Top: LA and TA phonons. Bottom: Neutron scattering diagram in the reciprocal space for TA (left) and LA phonons

4. Triple Axis Spectrometer PUMA

The three-axis instrument is the most versatile instrument for use in inelastic scattering because it allows one to probe nearly any coordinates in energy and momentum space in a precisely controlled manner. The three axes correspond to the axes of rotation of the *monochromator* (axis1), *the sample* (axis2), and *the analyzer* (axis3). The monochromator crystal selects neutrons with a certain energy from the white neutron beam emanating from the reactor. The monochromatic beam is then scattered off from the sample (second axis). The neutrons scattered by the sample can have a different energy from those incident on the sample. The energy of these scattered neutrons is then determined by the analyzer crystal (third axis). All three angles (θ_M, θ_S, θ_A) can vary during an experiment, the sample table and analyzer are equipped with air pads, so that they can glide over the "Tanzboden" (dancing floor). Below, we describe in detail each component of a triple-axis spectrometer.

Monochromator

A crystal monochromator is used to select neutrons with a specific wavelength. Neutrons with this wavelength interact with the sample and are scattered off at a similar (elastic) or different wavelength (inelastic). The energy of the neutrons both incident on and scattered from the sample is determined by Bragg reflection from the monochromator and analyzer crystals, respectively. For a specific Bragg plane (hkl) characterized by an interplanar spacing d_{hkl}, the crystal is rotated about a vertical axis. A pyrolytic graphite with d_{002} = 3.35 Å (PG(002)) and a copper with d_{220} = 1.28 Å (Cu(220)) monochromators are available at PUMA. The angular range of the monochromator $2\theta_M$ is of 15° - 115°. The PG(002) is usually used for energies below 50meV (λ>1.3Å). For higher incident energies the Cu(220) can be used.

Sample table

The sample table from the company Huber provides a possibility to vary independently both $2\theta_s$ and θ_S. It is equipped with a goniometer moving the sample in the three translation axes *x*, *y* and *z* and tilting. The tilt angle is ±15°. Single crystal experiments can be performed with an Euler cradle at PUMA. The sample environment includes magnets, pressure cells, cryostats and high temperature furnace.

Analyzer

Like the monochromator, the PG(002) analyzer consist of 20x5 separate analyzer crystal plates are mounted in an aluminum frame. There is an option to measure with the flat or horisontaly and verticaly focused analyser. The angular range of the analysator $2\theta_M$ is of -130° - 130°.

Detector and monitor

The detector consists of five counter tubes which are filled with a ^{3}He pressure of 5 bar. To be able to monitor the neutron flux incident on the sample, a low-efficiency neutron counter monitor is usually placed before the sample. Such a monitor is required so that flux variation caused by, for example, the reactor power fluctuations and the change in reflectivity of the monochromator with neutron wavelength can be automatically corrected for.

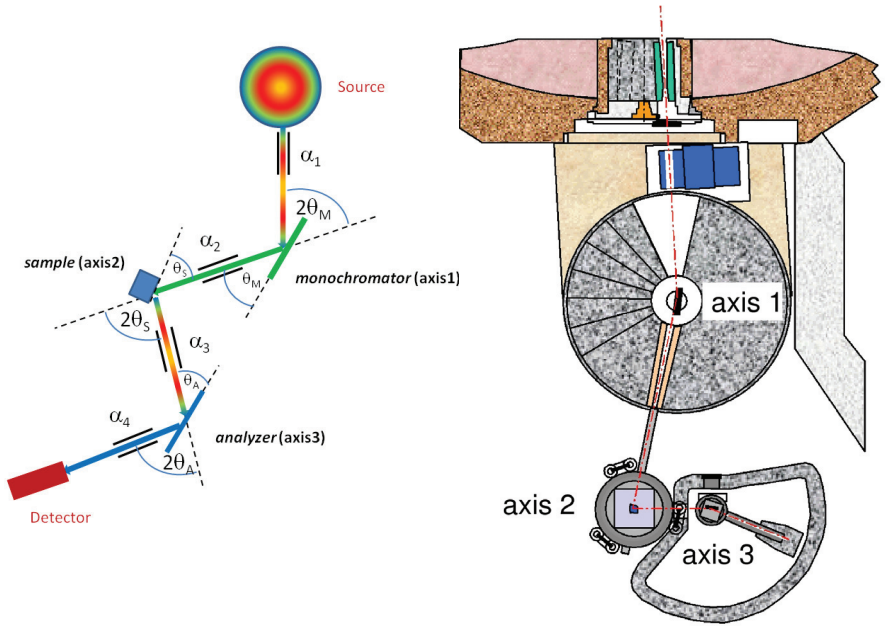

Fig.4 PUMA spectrometer.

Slits, Collimators, Filter

Additional components like slits or collimators are used to define the beam cross section. Collimators (α1- α4) are used for the improvement of the resolution and to specify the beam divergence. They consist of multiple parallel arranged Gd_2O_3 coated foils with a defined angle to the beam. The angular divergence of the collimator in the horizontal plane α is defined by the distance between foils Δd and the length of the collimator l (tan $\alpha = \Delta d / l$). Different collimators with a horizontal divergence between 10' and 60' are available at the instrument.

One of the problems of the TAS method is the possible presence of higher harmonics in the neutron beam. Higher harmonics arise from higher order (hkl) in Bragg's law (2). This means that if the monochromator (analyzer) crystal is set to reflect neutrons with a wavelength of λ from a given (hkl) plane, it will also reflect neutrons with wavelength λ/n. This leads to the appearance of several types of spurious peaks in the observed signal. Different filters are used to eliminate the high-order neutrons and to reduce the background. There are a sapphire filter (Al_2O_3) and an erbium filter (Er) at PUMA. They are installed in front of the monochromator. Sapphire filter is used wavelengths $\lambda > 1$ Å and reduce the background inducing by the epithermal neutrons. Erbium filter is suitable as $\lambda/2$ filter for λ between 0.5 and 1Å as well as $\lambda/3$ filter for λ between 0.7 and 1.6Å.

Components	Axis	PUMAs notation	Description
Monochromator M	θ_M	mth	Monochromator Theta
	$2\theta_M$	mtt	Monochromator 2Theta
		mtx, mty	Monochromator Translation x-, y- direction
		mgx, mgy	Monochromator Goniometer x-, y- direction
		mfh, mfv	Monochromator Focus horizontal, vertical
Sample S	θ_S	psi	Sample Theta
	$2\theta_S$	phi	Sample 2Theta
		stx, sty, stz	Sample Translation x-, y-, z- direction
		sgx, sgy	Sample Goniometer x-, y- direction
Analyzer A	θ_A	ath	Analyzer Theta
	$2\theta_A$	att	Analyzer 2Theta
		atx, aty	Analyzer Translation x-, y- direction
		agx, agy	Analyzer Goniometer x-, y- direction
		afh	Analyzer Focus horizontal
Collimators		alpha1 – alpha4	Collimation

5. Experiment Procedure

The aim of the experiment is to measure acoustic phonons in a germanium sample. The phonons will be measured for [110] (LA) and [001] (TA) directions in [220] BZ.
The experimental procedure shall contain the following steps:

Sample alignment

It is very difficult to align a sample with triple axis spectrometer, if the sample orientation is absolutely unknown. A sample must be pre-aligned, this means that the vertical axis of the sample must be known and roughly perpendicular to the 'Tanzboden'. Than we shall do the following steps:
- Inform the control program of the spectrometer about a scattering plane of the sample. One must set two reciprocal vectors (in our case [110] and [001]) laying in the scattering plane.
- Drive spectrometer (θ_M, $2\theta_M$, θ_S, $2\theta_S$, θ_A, $2\theta_A$,) to the position corresponding to [220] reflection.
- Scan θ_S and find the Brag's peak.
- Scan corresponding goniometer axes to maximize intensity of the peak.
- Do the same for other reflection [004].
- Change the offset of the θ_S so that the nominal θ_S values correspond to intensity maxima for the above reflections.

Phonons measurements

For our measurements we will chose the const-k_f configuration with $k_f = 2.662$ Å^{-1} ($E_f = 14.68$ meV). This means that we will scan the energy transfer $\hbar\omega = E_i - E_f$ by varying incident energy E_i (k_i). We are going to use PG(002) monochromator.

For LA phonon we will do constant-**Q** scans in the energy transfer range $\hbar\omega$ = 0 – 21 meV (0 – 8 THz) for the following points:
Q(r.l.u.) = (2.1, 2.1, 0), (2.2, 2.2, 0), (2.3, 2.3, 0), (2.4, 2.4, 0), (2.5, 2.5, 0), (2.6, 2.6, 0), (2.7, 2.7, 0), (2.75, 2.75, 0).

For TA phonon we will do constant-**Q** scans in the energy transfer range $\hbar\omega$ = 0 – 15 meV (0 – 3.6 THz) for the following points:
Q(r.l.u.) = (2, 2, 0.2), (2, 2, 0.3), (2, 2, 0.4), (2, 2, 0.5), (2, 2, 0.7), (2, 2, 0.8), (2, 2, 0.9), (2, 2, 1).

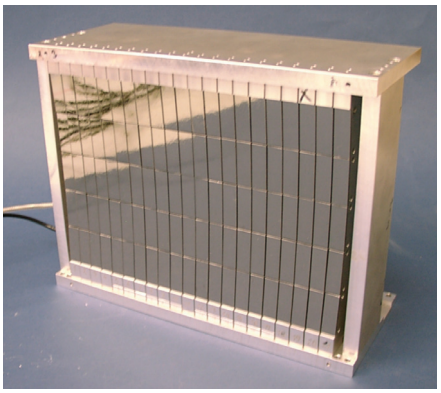

a) PG Analyzer

b) Soller collimator

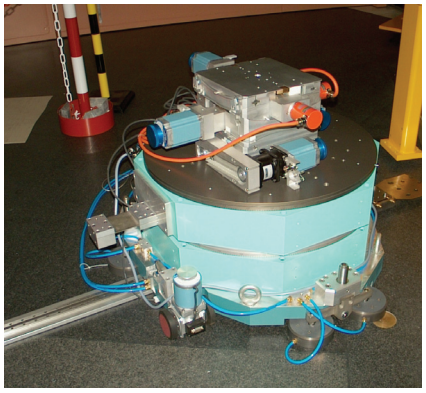

c) Sample table

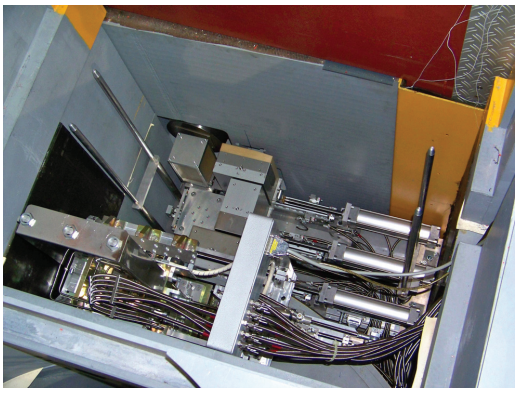

d) Shutter, filters and collimators

e) Analyzer and Detector

f) Detector, consists of 5 ^{3}He tubes

Fig 5 Elements of PUMA

6. Preparatory Exercises

1. Calculate angles θ_M, $2\theta_M$, θ_S, $2\theta_S$ for the reflections [220] and [004] of *germanium* (cubic-diamond, a = 5.66 Å), supposing that $k_f = 2.662$ Å^{-1} = const, monochromator is PG(002), and check, if this reflections are measurable with our experimental setup.

2. Before doing a scan it is important to check that all point in **Q** - $\hbar\omega$ space are available, instrument angles do not exceed high or low limits. Also, an experimental scientist must be sure that the moving instrument will not hit walls or any equipment. Calculate instrument parameters (θ_M, $2\theta_M$, θ_S, $2\theta_S$) for the momentum transfers **Q** (r.l.u.) = (2.1, 2.1, 0), (2.75, 2.75, 0) and energy transfers $\hbar\omega$ = 0 and 21 meV. This can be done using an online triple-axis simulator:
http://www.ill.eu/instruments-support/computing-for-science/cs-software/all-software/vtas/

7. Experiment-Related Exercises

1. Plot obtained spectra for each **Q** as a function of energy (THz). Fit the spectra with Gaussian function and find centers of the phopon peaks. The obtained phonon energies plot as a function of **q.**
2. Why triple-axis spectrometer is the best instrument to study excitations in single crystals?
3. During this practicum we do not consider some problems that are very important for planning experiments with a triple axis instrument such as *resolution* and *intensity zones* [2]. Persons who have a strong interest to the triple-axis spectroscopy should study these topics by oneself. Advanced students should be able to explain our choice of Brillouin zone and parameters of scans for the phonon measurements.

Useful formula and conversions

1 THz = 4.1.4 meV

$n\lambda = 2d_{hkl}\sin\theta_{hkl}$,

$$d_{hkl} = \frac{2\pi}{|\boldsymbol{\tau}_{hkl}|}$$

$$\mathbf{Q} = \mathbf{k_0} - \mathbf{k_f}$$

$$Q = \sqrt{k_i^2 + k_f^2 - 2k_i k_f \cos 2\theta}$$

If $k_i = k_f$ (elastic scattering) $Q = 2k_i \sin\theta = \frac{4\pi}{\lambda}\sin\theta$

E [meV] = 2.072 k^2 [Å^{-1}]

References

[1] Ch. Kittel, Einführung in die Festkörperphysik, Oldenburg, 14th ed., 2006
[2] G. Shirane, S.M. Shapiro, J.M. Tranquada, Neutron Scattering with a Triple-Axis Spektrometer, Cambridge University Press, 2002
[4] G. Eckold, P. Link, J. Neuhaus, Physica B, 276-278 (2000) 122- 123
[5] B.N.Brockhouse and P.K. Iyengar, Physikal Review 111 (1958) 747-754
[6] *http://www.ill.eu/instruments-support/computing-for-science/cs-software/all-software/vtas/*

Contact

PUMA

Phone: + 49 89 289 14914
Web: http://www.frm2.tum.de/wissenschaftliche-nutzung/spektrometrie/puma/index.html

Oleg Sobolev

Georg-August Universität Göttingen
Institut für Physikalische Chemie
Aussenstelle am FRM II
Phone: + 49 89 289 14754
Email: oleg.sobolev@frm2.tum.de

Anke Teichert

Georg-August Universität Göttingen
Institut für Physikalische Chemie
Aussenstelle am FRM II
Phone: + 49 89 289 14756
Email: anke.teichert@frm2.tum.de

Norbert Jünke

Forschungsneutronenquelle Heinz Maier-Leibnitz
ZWE FRM II
Phone: + 49 89 289 14761
Email: norbert.juenke@frm2.tum.de

SPODI

High-resolution powder diffractometer

M. Hoelzel, A. Senyshyn

Forschungsneutronenquelle Heinz Maier-Leibnitz (FRM II)
Technische Universität München

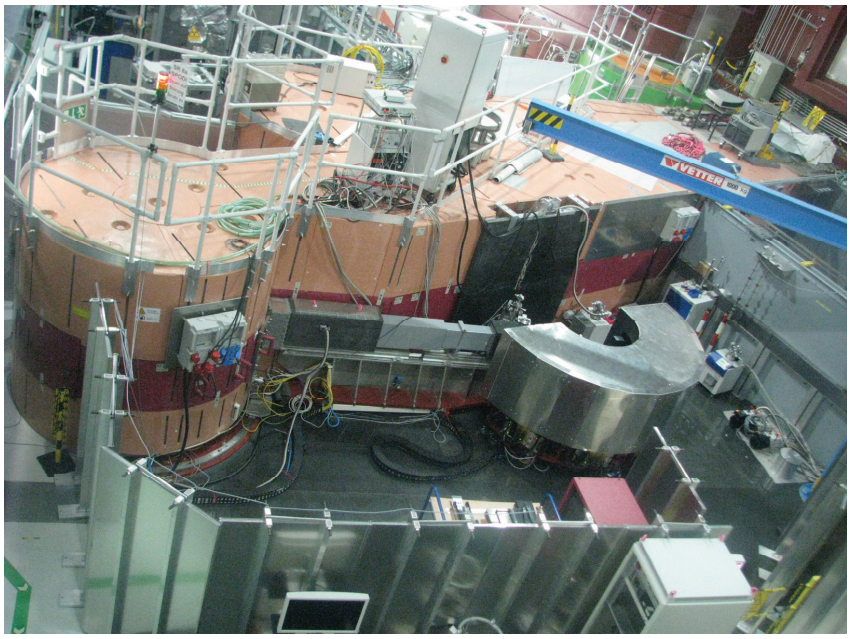

Manual of the JCNS Laboratory Course Neutron Scattering

Contents

1. **Applications of neutron powder diffraction**

Powder diffraction reveals information on the phase composition of a sample and the structural details of the phases. In particular, the positions of the atoms (crystallographic structure) and the ordering of magnetic moments (magnetic structure) can be obtained. In addition to the structural parameters, also some information on the microstructure (crystallite sizes/microstrains) can be obtained. The knowledge of the structure is crucial to understand structure – properties – relationships in any material. Thus, neutron powder diffraction can provide valuable information for the optimisation of modern materials.

Typical applications:

Material	**Task**
Lithium-ion battery materials	Positions of Li atoms, structural changes/phase transitions at the electrodes during operation, diffusion pathways of Li atoms
Hydrogen storage materials	Positions of H atoms, phase transformations during hydrogen absorption/desorption
Ionic conductors for fuel cells	positions of O/N atoms, thermal displacement paramteters of the atoms and disorder at different temperatures, diffusion pathways of O/N atoms
Shape memory alloys	stress-induced phase transforamtions, stress-induced texture development
materials with CMR effect	magnetic moment per atom at different temperatures
catalysers	Structural changes during the uptake of sorbents
Piezoelectric ceramics	Structural changes during poling in electric field, positions of O atoms
Nickel superalloys	Phase transformations at high temperatures, lattice mismatch of phases
magnetic shape memory alloys	Magneto-elastic effects, magnetic moment per atom at different temperatures and magnetic fields

2. Basics of Powder Diffraction

Diffraction can be regarded as detection of interference phenomena resulting from coherent elastic scattering of neutron waves from crystalline matter. Crystals can be imagined by a three-dimenional periodic arrangement of unit cells. The unit cell is characterised by the lattice parameters (dimensions and angles) and the positions of atoms or molecules.
For diffraction experiments the probe should have a wavelength comparable to interatomic distances: this is possible for X-rays, electrons or neutrons.

Structure factor

The structure factor describes the intensity of Bragg reflections with Miller indexes (*hkl*), based on the particular atomic arrangement in the unit cell

$$F_{hkl} = \sum_{j=1}^{n} b_j T_j \exp\left\{2\pi i \vec{H}\vec{R}_j\right\}$$

where
F_{hkl}: structure factor of Bragg reflection with Miller indexes *hkl*.
n: number of atoms in unit cell
$b_{j:}$ scattering lengths (in case of neutron scattering) or atomic form factor (in case of X-ray diffraction) of atom *j*
$T_{j:}$ Debye Waller factor of atom *j*

The scalar product H R_j consists of the reciprocal lattice vector H and the vector R_j, revealing the fractional atomic coordinates of atom j in the unit cell.

$$\vec{H}\vec{R}_j = \begin{pmatrix} h \\ k \\ l \end{pmatrix} \cdot \begin{pmatrix} x_j \\ y_j \\ z_j \end{pmatrix} = hx_j + ky_j + lz_j$$

Thus, the structure factor can also be given as follows:

$$F_{hkl} = \sum_{j=1}^{n} b_j T_j \exp\left\{hx_j + ky_j + lz_j\right\}$$

The intensity of a Bragg reflection is proportional to the square of the absolute value of the structure factor: $I \propto \left|F_{hkl}\right|^2$

Debye-Waller Factor

The Debye-Waller Factor describes the decrease in the intensity of Bragg reflections due to atomic thermal vibrations.

$$T_j(Q) = \exp\left\{-\frac{1}{2}\left\langle\left(\vec{Q}\vec{u}_j\right)\right\rangle\right\}$$

vector $\boldsymbol{u_j}$ reflects the thermal displacements of atom j

Braggs' Law

Braggs' Law provides a relation between distances of lattice planes with Miller indexes *hkl,* i.e. d_{hkl}, and the scattering angle 2θ of the corresponding Bragg peak. Braggs' law can be illustrated in a simplified picture of diffraction as reflection of neutron waves at lattice planes (figure 4). The waves which are reflected from different lattice planes do interfere. We get constructive interference, if the path difference between the reflected waves corresponds to an integer multiple of the wavelength.
The condition for constructive interference (= Braggs' law) is then:

$$2d_{hkl}\sin\theta = n\lambda$$

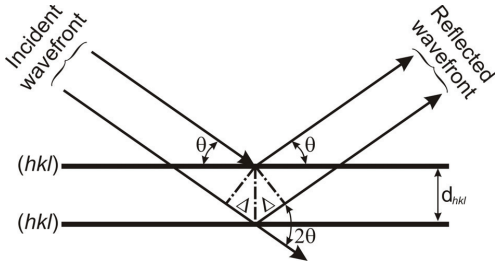

Figure 1: Illustration of Bragg's law: constructive interference of neutron waves, reflected from lattice planes, where θ, 2θ are Bragg angles, $2\Delta=2d_{hkl}\sin\theta$ is the path difference and $2\Delta=n\lambda$ is the constructive interference.

Applying Bragg's law one can derive the lattice spacings ("d-values") from the scattering angle positions of the Bragg peaks in a constant-wavelength diffraction experiment. With the help of d-values a qualitative phase analysis can be carried out.

Ewald's sphere

The Ewald's sphere provides a visualisation of diffraction with help of the reciprocal lattice. At first, we introduce the scattering vector ***Q*** and the scattering triangle (Figure 2). The incident neutron wave is described by a propagation vector $\boldsymbol{k_i}$, the scattered wave is given by $\boldsymbol{k_f}$. In the case of elastic scattering (no energy transfer) both vectors $\boldsymbol{k_i}$ and $\boldsymbol{k_f}$ have the same length which is reciprocal to the wavelength.

$$|k_i| = |k_f| = \frac{2\pi}{\lambda}$$

remark:

The length of the wave vectors are sometimes given as $|k_i| = |k_f| = \frac{1}{\lambda}$ *(This definition is found esp. in crystallographic literature, while the other one is more common for physists).*

The angle between vectors $\boldsymbol{k_i}$ and $\boldsymbol{k_f}$ is the scattering angle 2θ. The scattering vector ***Q*** is the given by the difference between $\boldsymbol{k_i}$ and $\boldsymbol{k_f}$:

$$\boldsymbol{Q} = \boldsymbol{k}_f - \boldsymbol{k}_i \quad |Q| = 4\pi \frac{\sin\theta}{\lambda}$$

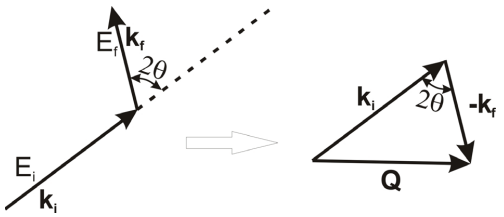

Figure 2: Illustration of scattering vector and scattering angle resulting from incident and scattered waves.

In the visualisation of the diffraction phenomena by Ewald the scattering triangle is implemented into the reciprocal lattice of the sample crystal – at first, we consider diffraction at a single crystal (Figure 3). Note that the end of the incident wave vector coincides with the origin of the reciprocal lattice. Ewald revealed the following condition for diffraction: we have diffraction in the direction of $\boldsymbol{k_f}$, if its end point (equivalently: the end point of scattering vector ***Q***) lies at a reciprocal lattice point *hkl*. All possible $\boldsymbol{k_f}$, which fulfil this condition, describe a sphere with radius 2π/λ, the so called Ewald's sphere. Thus we obtain a hkl reflection if the reciprocal lattice point hkl is on the surface of the Ewald's sphere.

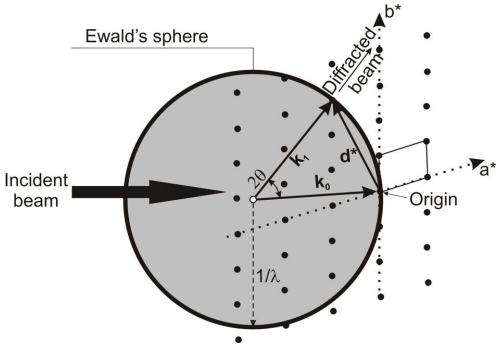

Figure 3: Illustration of diffraction using the Ewald's sphere.

Here, the radius of Ewald's sphere is given by 1/λ (For $|k_i| = \frac{2\pi}{\lambda}$ we obtain a radius of 2π/λ).

We receive the following condition for diffraction: the scattering vector ***Q*** should coincide with a reciprocal lattice vector $\boldsymbol{H_{hkl}}$ (x 2π):

$$\vec{Q} = 2\pi\vec{H}_{hkl};\ \vec{H}_{hkl} = h\vec{a}^{\,x} + k\vec{b}^{\,x} + l\vec{c}^{\,x};\ \left|\vec{H}_{hkl}\right| = d^{x}_{hkl} = \frac{1}{d_{hkl}}$$

From this diffraction condition based on the reciprocal lattice we can derive Bragg's law:

$$\left|\vec{Q}\right| = 2\pi\left|\vec{H}_{hkl}\right| \rightarrow 4\pi\frac{\sin\theta}{\lambda} = \frac{2\pi}{d_{hkl}} \rightarrow 2d_{hkl}\sin\theta = \lambda$$

The Ewald's sphere is a very important tool to visualize the method of single crystal diffraction: At a random orientation of a single crystalline sample a few reciprocal lattice points might match the surface of Ewald's sphere, thus fulfil the condition for diffraction. If we rotate the crystal, we rotate the reciprocal lattice with respect to the Ewald's sphere. Thus by a stepwise rotation of the crystal we receive corresponding reflections.

Powder Diffraction in Debye-Scherrer Geometry

In a polycrystalline sample or a powder sample we assume a random orientation of all crystallites. Correspondingly, we have a random orientation of the reciprocal lattices of the crystallites. The reciprocal lattice vectors for the same *hkl*, i.e. $\boldsymbol{H_{hkl}}$, describe a sphere around the origin of the reciprocal lattice. In the picture of Ewald's sphere we observe diffraction effect, if the surface of the Ewald's sphere intersects with the spheres of $\boldsymbol{H_{hkl}}$ vectors. For a sufficient number of crystallites in the sample and a random distribution of grain orientations, the scattered wave vectors ($\boldsymbol{k_f}$) describe a cone with opening angle 2θ with respect to the inident beam $\boldsymbol{k_i}$.
In the so called Debye-Scherrer Geometry a monochromatic beam is scattered at a cylindrical sample. The scattered neutrons (or X-rays) are collected at a cylindrical detector in the scattering plane. The intersection between cones (scattered neutrons) and a cylinder (detector area) results in segments of rings (= Debye-Scherrer rings) on the detector. By integration of the data along the Debye-Scherrer rings one derives the conventional constant-wavelength powder diffraction pattern, i.e. intensity as a function of the scattering angle 2θ.

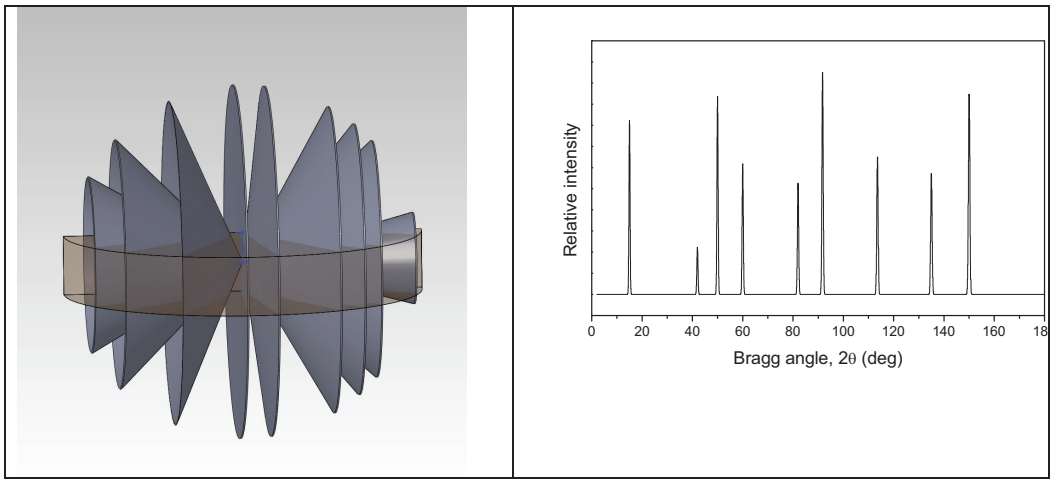

Figure 4: Illustration of powder diffraction in Debye-Scherrer Geometry. On the left: cones of neutrons scattered from a polycrystalline sample are detected in the scattering plane. On the right: resulting powder diffraction pattern.

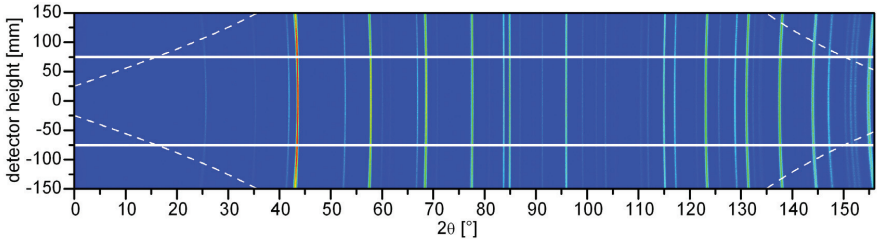

Figure 5: Two dimensional diffraction data (detector height vs. scattering angle 2θ), collected at high-resolution powder diffractometer SPODI, illustrating the Debye-Scherrer rings of a corundum sample.

Relations between Bragg positions and lattice parameters

With the help of Braggs law one can derive the lattice spacings “d-values” directly from the positions of Bragg reflections. The d-values are related with the lattice parameters of the unit cell (the cell dimensions a,b,c and the cell angles α,β,γ) and the Miller indexes (hkl) of the corresponding reflections. In the following, the relations are provided for the different crystal systems.

cubic $$\frac{1}{d_{hkl}} = \frac{h^2 + k^2 + l^2}{a^2}$$

hexagonal $$\frac{1}{d_{hkl}} = \frac{4}{3}\frac{h^2 + hk + k^2}{a^2} + \frac{l^2}{c^2}$$

tetragonal $$\frac{1}{d_{hkl}} = \frac{h^2 + k^2}{a^2} + \frac{l^2}{c^2}$$

orthorhombic $$\frac{1}{d_{hkl}} = \frac{h^2}{a^2} + \frac{k^2}{b^2} + \frac{l^2}{c^2}$$

monoclinic $$\frac{1}{d_{hkl}} = \frac{h^2}{a^2 \sin^2\beta} + \frac{k^2}{b^2} + \frac{l^2}{c^2 \sin^2\beta} + \frac{2hl\cos\beta}{ac\sin^2\beta}$$

3. Information from powder diffraction experiments

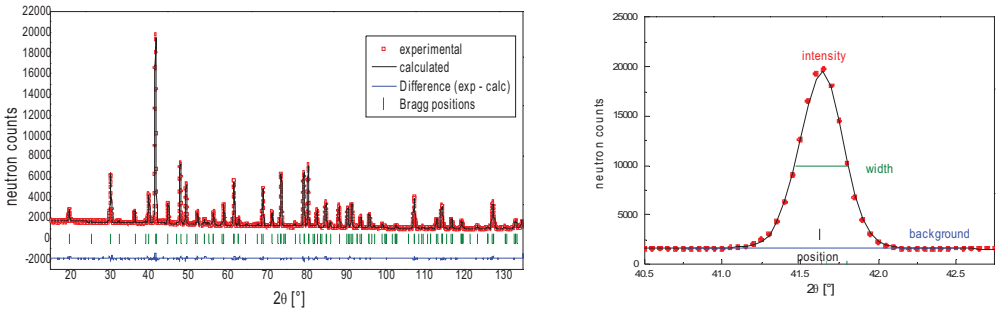

Figure 6: on the left: typical powder diffraction pattern. On the right: zoom on a single Bragg peak.

In the following, we will consider the information which can be derived from different elements of the diffraction patterns.

Positions (scattering angles) of Bragg reflections

- phase identification (from d-values)
- lattice parameters
- symmetry information (space group) by lattice parameters and selection rules (systematic extinction of reflections)

Intensity of Bragg reflections

- crystallographic structure
  - positions of atoms (fractional atomic coordinates)
  - occupancies of atoms on their sites
  - thermal displacement parameters
- magnetic structure
  - magnetic lattice (propagation vector)
  - magnetic symmetry (space group)
  - magnetic moment per atom
- quantitative phase analysis
- preferred orientation effects

Profiles of reflections

The reflection profiles result in a convolution of the instrumental resolution function with broadening effects of the sample

- microstructural information
  - microstrains
  - crystallite sizes

Modulation/Profile of Background

- short range order
- disorder
- amorphous contents

4. Evaluation of Powder Diffraction Data

The methods of data treatment can be classified in analysis of phase composition or phase transformation, structure solution and structure refinement.
Qualitative phase analysis is based on the determination of d-values and relative intensities (in particular intensities of strong reflections have to be considered). The phase identification is supported by crystallographic data bases (ICDD, ISCD), literature data and information from other methods (for instance, analysis of the chemical composition). Such kind of phase analysis is however typically carried out with X-ray diffraction.
The majority of neutron powder diffraction studies is based on experiments at various temperatures to investigate phase transformation behaviour as a function of temperature. There is an increasing demand for parametric studies, i.e. diffraction studies under various environmental conditions (temperature, electric or magnetic field, mechanical stress, gas atmosphere...) with particular attention to reaction pathways/reaction kinetics. This kind of investigations require in general high-intensity powder diffraction.
Powder diffracton data can be used either for phase identification or for the refinement of structural parameters, such as lattice parameters, fractional atomic coordinates, atomic occupancies and atomic displacement parameters by the full profile Rietveld analysis. In the Rietveld method, the full diffraction pattern is calculated by a structure model, taking into account the above mentioned structural parameters, as well as reflection profile parameters, instrumental parameters and background parameters. Using least-squares method, the experimental data can be fitted to the model in a stepwise refinement of the parameters. The complexity of the structures is directly dependent on the instrument specification, in particular, high-resolution powder diffractometers are designed for structure refinements on complex systems.
Besides structure refinement, also structure solution can be done based on powder diffraction patterns by various methods.

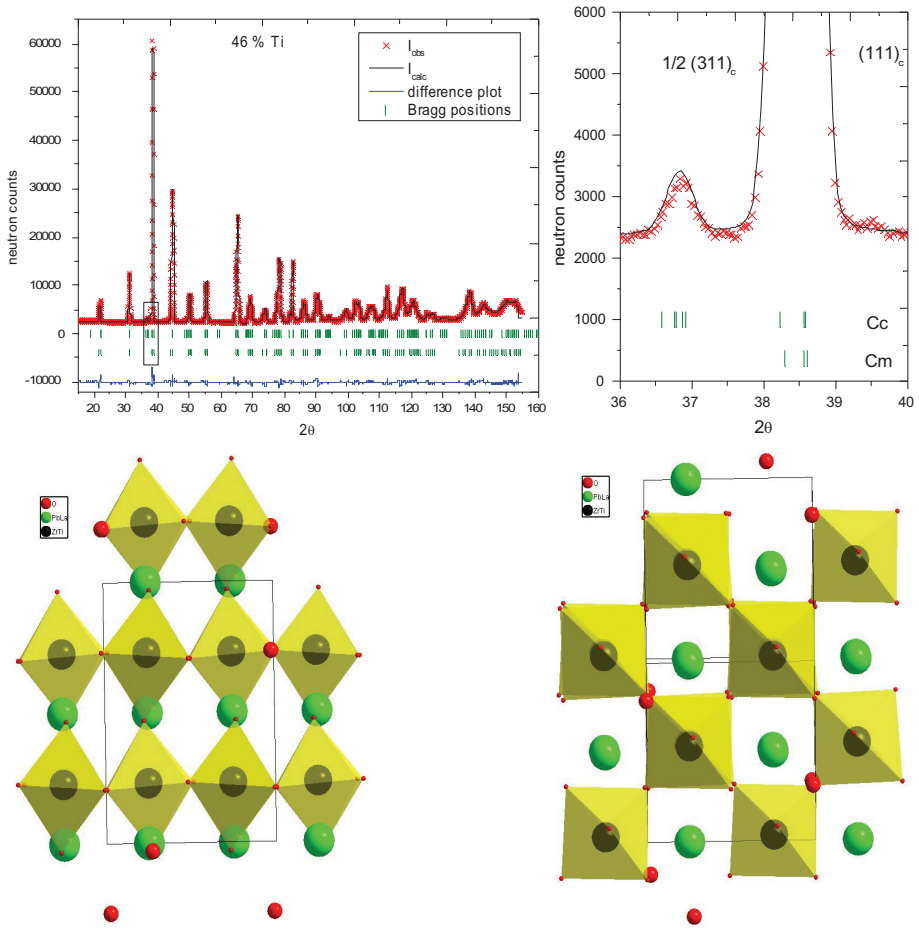

Figure 7: Data treatment of a measurement on the ferroelectric $Pb_{0.99}La_{0.01}Zr_{0.54}Ti_{0.46}O_3$, carried out at 5 K at diffractometer SPODI (FRM II): Diffraction pattern including experimental data, calculated data by Rietveld fit, Bragg reflection positions of the phases (space groups C_C *and* C_m) and difference plot (between experimental and calculated data). - zoom into the diffraction pattern, hightlighting a superlattice reflection of the C_C phase. - structure model of the C_C phase, view in the $[001]_c$ direction - structure model of the C_C phase, view in the $[010]_c$ direction. In particular, the superstructure in the tiltings of oxygen octahedra can be seen.

5. Comparison between Neutron and X-ray diffraction

I) X-rays are scattered at electrons, neutrons are scattered at nuclei

In case of X-ray scattering, the scattering power of an atom (described by the atomic form factor *f*) is proportional to the number of electrons.
Neutrons are scattered at nuclei. Thus the interaction (described by the scattering length b) varies between different isotopes of an element. Scattering length of neighbouring elements in the periodic system can be very different.

implications:

Localisation of light elements next to heavier ones

X-ray diffraction is a powerful tool to determine the positions of heavy atoms, but the localisation of light atoms in the vicinity of much heavier atoms is often difficult or related with high uncertainties. Neutron diffraction is advantageous to localise light atoms such as H, D, Li, C, N, O.

Localisation of neighbouring elements in the periodic table

Neighbouring elements in the periodic table can hardly be distinguished by means of X-ray diffraction. Neutrons are advantageous for such cases: examples: Mn – Fe - Co – Ni or O – N.

Q-dependence of intensities

Since the size of electron clouds is comparable to the wavelength, the atomic form factor depends on $\sin\theta/\lambda$ or Q. Therefore the intensities of X-ray reflections decrease significantly for increasing Q (increasing scattering angles 2θ).
As the range of the neutron–nuclei–interaction is by orders of magnitude smaller than the wavelengths of thermal neutrons, scattering lengths do not depend on Q. As a consequence, neutron diffraction patterns do not show a decrease of Bragg reflection intensities for higher scattering angles, enabling the analysis of larger Q-ranges. In particular, neutron diffraction is advantageous for the analysis of thermal displacement parameters.

II) neutrons interact weakly with matter

implications:

sample volume

The flux from neutron sources much lower compared to X-ray tubes or even synchrotrons. In addition, neutrons interact weakly with matter. Therefore, much larger sample amounts are required compared to X-ray diffraction ("grams instead of milligrams"). On the other hand this weak interaction results in much higher penetration depths of neutrons, compared to laboratory X-ray diffractometers. Thus, polycrystalline bulk samples can be investigated. Furthermore, using large sample volumes avoids possible problems due to preferred orientation effects. In principle, bulk samples can also be investigated with high-energy synchrotron radiation. Anyhow in special cases the very low scattering angles related to low wavelength (in high-energy synchrotron studies) can cause difficulties.

Sample environments

The large penetration depths of neutrons facilitate the usage of sample environments like cryostat, furnaces, magnets... In general neutron scattering experiments are more powerful applying high or low temperatures. On the other hand, the small sample volume required for synchrotron studies gives better possibilities for high-pressure experiments.

III) neutrons exhibit a magnetic moment

Though neutrons do not have an electric charge, the internal charge distribution due to its three quarks along with the spin result in a magnetic moment of the neutron.

implications:

magnetic scattering

The interaction between the magnetic moment of the neutron and a possible magnetic moment of an atom results in a magnetic scattering contribution, incidentally in the same order of magnitude as the nuclear scattering contribution. The magnetic scattering contribution can be easily detected by means of neutron diffraction. In synchrotron diffraction studies, possible magnetic scattering events are by several orders of magnitude weaker than the Thomson scattering.

6. Setup of the high-resolution neutron powder diffractometer SPODI at FRM II

The main components of a constant-wavelength neutron powder diffractometer are: source, monochromator, sample and detector. Between these components collimation systems are installed which have high impact on the instrumental resolution function and the neutron flux.

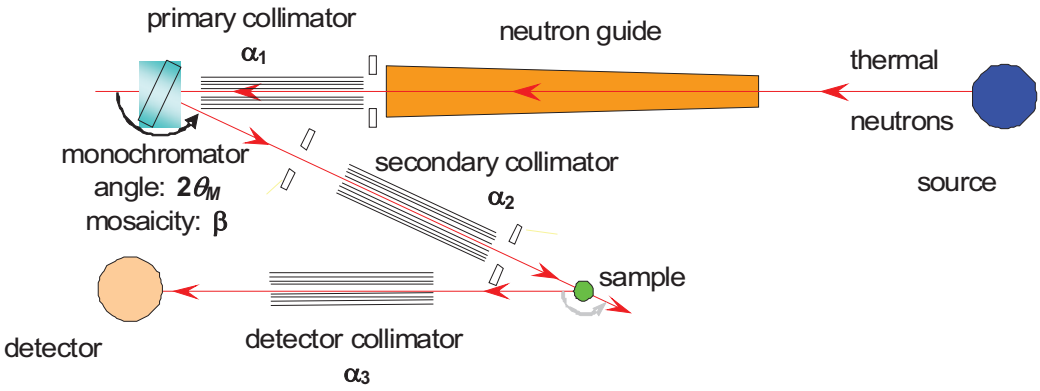

Figure 8: illustration of a typical instrumental layout, introducing the parameters used by Caglioti to describe the instrumental resolution function.

Instrumental resolution function

As shown by Calgioti, the instrumental resolution function of a constant-wavelength powder diffractometer can be approximated by:

$$FWHM = \sqrt{U \tan^2 \theta + V \tan \theta + W}$$

with the Caglioti parameters:

$$U = \frac{4\left(\alpha_1^2\alpha_2^2 + \alpha_1^2\beta^2 + \alpha_2^2\beta^2\right)}{\tan^2\theta_m\left(\alpha_1^2 + \alpha_2^2 + 4\beta^2\right)}$$

$$V = \frac{-4\alpha_2^2\left(\alpha_1^2 + 2\beta^2\right)}{\tan\theta_m\left(\alpha_1^2 + \alpha_2^2 + 4\beta^2\right)}$$

$$W = \frac{\alpha_1^2\alpha_2^2 + \alpha_1^2\alpha_3^2 + \alpha_2^2\alpha_3^2 + 4\beta^2\left(\alpha_2^2 + \alpha_3^2\right)}{\left(\alpha_1^2 + \alpha_2^2 + 4\beta^2\right)}$$

in this approach it is assumed that all components have Gaussian transmission profiles. The resolution function is determined by the horizontal beam divergences α_1, α_2, α_3, the monochromator angle $2\theta_m$ and the mosaicity of the monochromator β (Figure 8). As the impact of these parameters on the instrumental resolution function can be estimated, the Caglioti equations help to design an instrument to achieve a designated performance. However, it should be emphasised that in the approximations of Caglioti only the horizontal beam divergences are taken into account, neglecting vertical beam divergences by a vertical focusing monochromator or a vertical divergent neutron guide. Those effects are taken into account by ray-tracing methods, which allow a detailed modelling of the individual components.

The powder diffractometer SPODI has been designed to achieve both high resolution and good profile shape. In its standard configuration (highest resolution mode) SPODI uses a unique very high monochromator take-off angle of 155° along with a large monochromator-to-sample distance of 5 meters. An evacuated beam tube of about 4 m in length is located between the monochromator and the sample which also controls both vertical and horizontal neutron beam divergences at the sample position. Thus the natural neutron beam divergence in horizontal plane is 25' only. It can be reduced down to even 5' by optional Soller collimators in front of the sample.

Monochromator

At constant-wavelength diffractometers, the monochromatisation is perfomed using crystals followings Bragg's equation:

$2d_{hkl}\sin\theta = \lambda$, where the effective transmission band is determined by a derivative

$$\frac{\Delta\lambda}{\lambda} = \Delta\theta_M \cot\theta_M$$

The width of the wavelength band $\Delta\lambda/\lambda$ strongly depends on the monochromator angle $2\theta_m$ and the mosaicity of the monochromator β oρ $\Delta\theta_m$. Thus these parameters have a major impact on the instrumental resolution function and the flux on the sample.

Typically, the monochromator crystals are installed at a vertical focusing unit of 200 – 300 mm, allowing optimization of the intensity distribution at the sample position with respect to the monochromator – sample distance or the sample height. On the other hand, the vertical beam divergence results in a smearing of the Debye-Scherrer rings along the detector height (this effect depends also on the sample height). At the high-resolution powder diffractometer SPODI, 15 Germanium wafer-stack crystals with a (551)-orientation are used. Different wavelengths between 1.0 and 2.6 Å can easily be selected by rotation of the monochromator unit (without changing the monochromator take-off angle $2\theta_m$), i.e. by selecting different (*hkl)* reflection planes. In general, large wavelengths are advantageous to investigate structures exhibiting large d-values. This is the case for large unit cells, but in particular for magnetic ordering. With decreasing wavelengths, larger Q-values can be achieved. Thus, with lower wavelengths, more reflections can be observed in the same scattering angle range. Low wavelengths are in particular advantageous for the analysis of thermal displacement parameters or static disorder phenomena.

Detector array

At constant-wavelength diffractometers the data are collected in an angle-dispersive manner at equidistant 2θ points. Detector systems based on ^{3}He have been most commonly used due to their very high efficiency. Now, the world wide shortage of ^{3}He demands and promotes the development of alternatives, in particular scintillator based systems.
Classical high-resolution powder diffractometers, such as D2B (ILL), SPODI (FRM II), BT1 (NIST), ECHIDNA (ANSTO) use multidetector/multicollimator systems. The data are collected by ^{3}He tubes while the beam divergence is limited by Soller collimators. Such systems enable high Q-resolution over a broad scattering angle regime, while the resolution does not depend on the sample diameter. On the other hand, a multidetector concept requires a data collection by stepwise positioning of the detector array to collect the full diffraction pattern. Therefore, kinetic measurements are not feaible due to the fact that the sample must not change during the collection of a pattern.
The detector array of SPODI consists of 80 ^{3}He tubes, which are position sensitive in the vertical direction. Thus, two-dimensional raw data are obtained, which allow to rapid check for sample crystallinity, alignment and possible preferred orientation effects. The conventional diffraction patterns (intensity vs. scattering angle 2θ) are derived from the two-dimensional raw data by integration along the Debye-Scherrer rings.

7. Experiment: Phase- and structure analysis of lead titanate at various temperatures

samples

Lead zirconate titanates $PbZr_{1-x}Ti_xO_3$ („PZT“) exhibit piezo-, pyro- and ferroelectric properties. Piezoelectricity describes the generation of an electric polarisation as a consequence of a mechanical deformation – or the other way round the development of a macroscopic strain by an electric field. The crystallographic condition of piezoelectricity is the lack of an inversion center: as the balance points of negative and positive charge do not coincide the displacements of the ions in the electric field results in a polarization. Pyroelectrticity refers to a spontaneous polarization of a material as a function of temperature. Ferroelectrics are special pyroelectric materials, in which the polarization can be switched by an electric field, resulting in a ferroelectric hysteresis.

The electromechanical properties of $PbZr_{1-x}Ti_xO_3$ can be understood by their phase transformation behaviour. At high temperatures they exhibit the perovskite structure with simple cubic symmetry (space group Pm-3m). Because of its symmetry (inversion center) this phase is not piezoelectric but paraelectric. During cooling, titanium-rich samples undergo a phase transition to a tetragonal phase (space group P4mm). This phase transformation is accompanied by atomic displacements. In particular, the Ti^{4+}/Zr^{4+} are shifted in the opposite direction than O^{2-} ions, resulting in a dipole moment or a spontaneous polarisation. The material exhibits ferroelectric behaviour, with a polar axis in the direction of the pseudocubic c-axis, i.e. $[001]_c$. Zirconium rich samples undergo a phase transition towards a rhombohedral phase (space group R3m) during cooling. In this case, the atomic displacements result in a polar axis in direction $[111]_c$ with respect to the parent pseudocubic lattice. Materials $PbZr_{1-x}Ti_xO_3$ with compositions (Zr/Ti ratios) close to the so called morphotropic phase boundary between rhombohedral and tetragonal phase, show the highest piezoelectric response, i.e. the largest macroscopic strain as a function of the applied electric field. These compositions are therefore most interesting for technological applications. The piezoelectric properties can be modified further by adding doping elements to substitute Pb^{2+} or Ti^{4+}/Zr^{4+} ions.

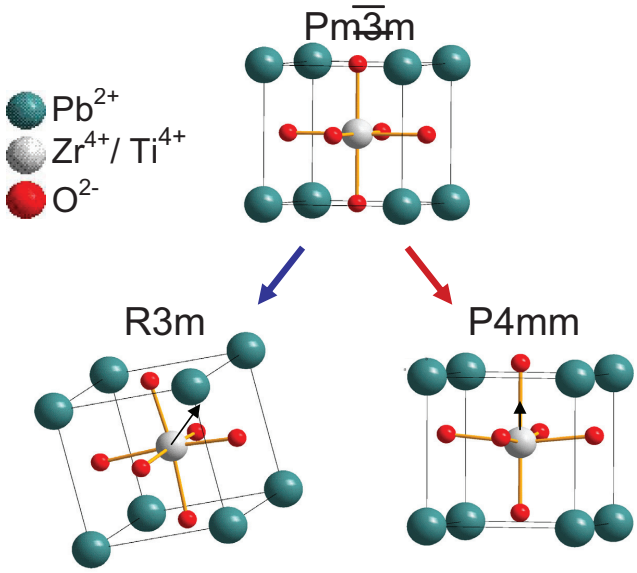

Figure 9: Structure models of the paraelectric cubic phase and the ferroelectric rhombohedral and tetragonal phases.

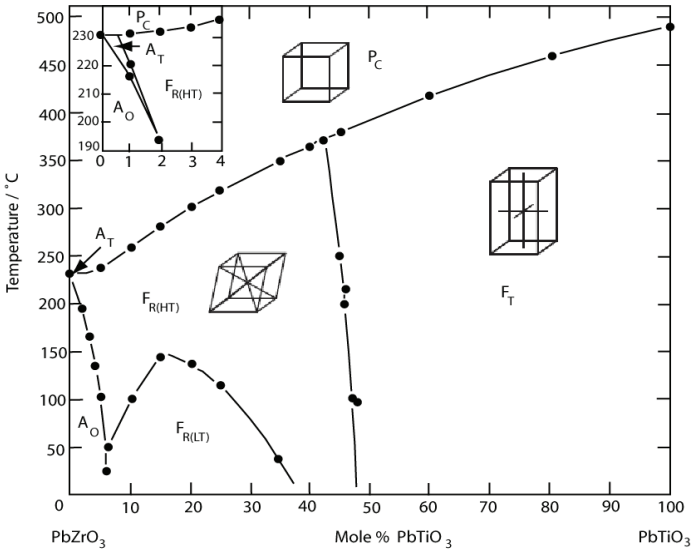

Figure 10: Phase diagram of $PbZr_{1-x}Ti_xO_3$, illustrating regions of phase stability for paraelectric cubic phase P_C, ferroelectric rhomboedral phases $F_{R(HT)}$ (= high temperature) and $F_{R(LT)}$ (= low temperature) and ferroelectric tetragonal phase F_T. From B. Jaffe, W. R. Cook, H. Jaffe, Piezoelectric Ceramics and Related Issues, Academic Press, London, 1971.

$PbZr_{1-x}Ti_xO_3$, find extensive applications

- transformation from mechanical in electric energy: ignition elements, lighters
- transformation from electric in mechanical energy (actuators): loudspeakers, sonar transducers, Active control of vibration
- transformation from mechanical force in an electric signal (sensors): strain gauges, microphones
- data storage, information technology: capacitors, F-RAM

Experiment

In the frame of the practical course, the temperature-dependent phase transformation behavior of a $PbZr_{1-x}Ti_xO_3$ with a composition on the tetragonal side should be investigated. Diffraction patterns at different temperature steps between room temperature and 600 °C will be collected with a vacuum high-temperature furnace. The structural changes at different temperatures will be investigated by an analysis of the lattice parameters. Based on the experimental data, the relations between the structural changes and the corresponding physical properties can be discussed.

Following experimental procedures will be carried out

- sample preparation, filling the sample material into a sample can, adjustment of the sample stick, installation of the sample stick into the furnace
- short test measurement to check the sample adjustment and data quality
- editing a program to run the data collection at various temperatures and starting the scans
- data reduction: Derivation of diffraction patterns from the two-dimensional raw data
- data analysis: analysis of the lattice parameter changes as a function of temperature
- discussing the results with respect to structure – properties relationships

Literature

[1] V. K. Pecharsky, P. Y. Zavalij, Fundamentals of Powder Diffraction and structural Characterisation of Materials (2003).
[2] G. L. Squires, Introduction to the Theory of Thermal Neutron Scattering, Dover Reprints (1978).
[3] C. Kittel, Einführung in die Festkörperphysik, 10. Edition, Oldenbourg (1993).
[4] H. Dachs, Neutron Diffraction, Springer Verlag (1978).
[5] H. Ibach und H. Lüth, Festkörperphysik, Einführung in die Grundlagen, 6. Edition, Springer
Verlag (2002).
[6] J.R.D. Copley, The Fundamentals of Neutron Powder Diffraction (2001), http://www.nist.gov/public_affairs/practiceguides/SP960-2.pdf.
[7] A. D. Krawitz, Introduction to Diffraction in Materials Science and Engineering.
[8] W. Kleber, Einführung in die Kristallographie, Oldenbourg (1998).

Contact

SPODI

Web: http://www.frm2.tum.de/wissenschaftliche-nutzung/diffraktion/spodi/index.html

Dr. Markus Hoelzel

Forschungsneutronenquelle Heinz Maier-Leibnitz (FRM II)
Technische Universität München
Phone: 089/289-14314
e-Mail: markus.hoelzel@frm2.tum.de

Dr. Anatoliy Senyshyn

Forschungsneutronenquelle Heinz Maier-Leibnitz (FRM II)
Technische Universität München

Phone: 089/289-14316
e-Mail: anatoliy.senyshyn@frm2.tum.de

HEiDi

Hot Single Crystal Diffractometer for Structure Analysis with Neutrons

M.Meven

Institut für Kristallographie, RWTH Aachen
and
Jülich Centre for Neutron Science
Forschungszentrum Jülich

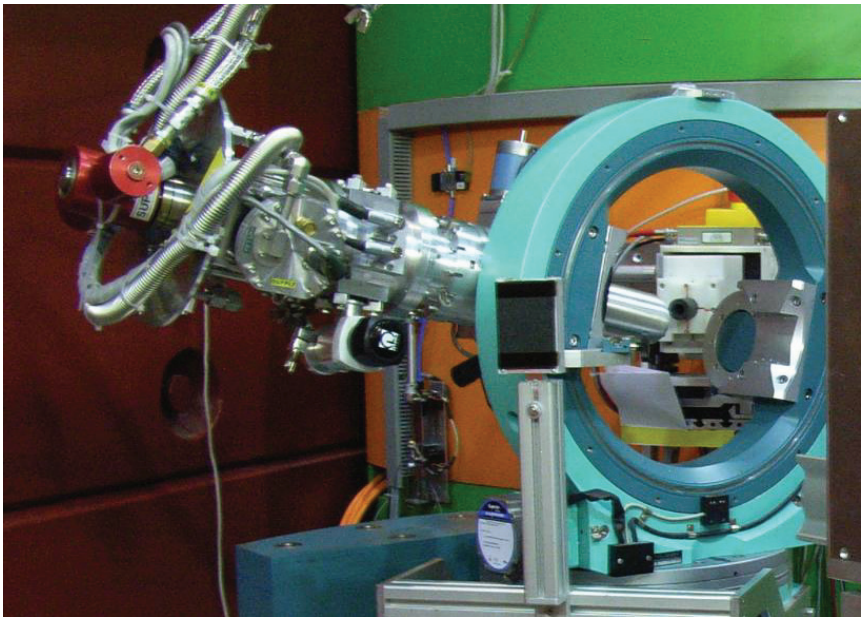

Manual of the JCNS Laboratory Course Neutron Scattering

Contents

1 Introduction

Many properties of solid matter like their mechanical, thermal, optical, electrical and magnetic properties depend strongly on their atomic structure. Therefore, a good understanding of the physical properties needs not only the knowledge about the particles inside (atoms, ions, molecules) but also about their spatial arrangement. For most cases diffraction is *the* tool to answer questions about the atomic and/or magnetic structure of a system. Beyond this, neutron diffraction allows to answer questions where other techniques fail.

2 Crystallographic Basics

In the ideal case a complete solid matter consists of small identical units (same content, same size, same orientation like sugar pieces in a box). These units are called unit cells. A solid matter made of these cells is called a single crystal. The shape of a unit cell is equivalent to a parallelepiped that is defined by its base vectors $\mathbf{a_1}$, $\mathbf{a_2}$ und $\mathbf{a_3}$ and that can be described by its lattice constants a, b, c; α, β and γ (pic. 1). Typical lengths of the edges of such cells are between a few and a few ten Ångström (1Å=10^{-10} m). The combination of various restrictions of the lattice constants between $a \neq b \neq c$; $\alpha \neq \beta \neq \gamma \neq 90°$ (triclinic) and $a = b = c$; $\alpha = \beta = \gamma = 90°$ (cubic) yields seven crystal systems. The request to choose the system with the highest symmetry to describe the crystal structure yields fourteen Bravais lattices, seven primitive and seven centered lattices.

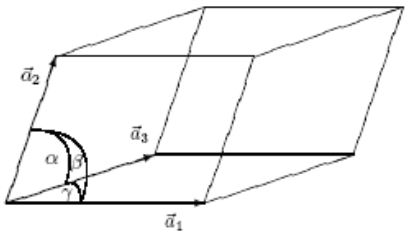

Fig. 1: Unit cell with $|\mathbf{a_1}|=a$, $|\mathbf{a_2}|=b$, $|\mathbf{a_3}|=c$, α, β, γ

Each unit cell contains one or more particles i. The referring atomic positions $\mathbf{x_i}=x_i*\mathbf{a_1} + y_i*\mathbf{a_2} + z_i*\mathbf{a_3}$ are described in relative coordinates $0 \leq x_i; y_i; z_i < 1$. The application of different symmetry operations (mirrors, rotations, glide mirrors, screw axes) on the atoms in one cell yield the 230 different space groups (see [1]).

The description of a crystal using identical unit cells allows the representation as a threedimensional lattice network. Each lattice point can be described as the lattice vector $\mathbf{t} = u*\mathbf{a_1} + v*\mathbf{a_2} + w*\mathbf{a_3}$; $u, v, w \in \mathbf{Z}$. From this picture we get the central word for diffraction in crystals; the *lattice plane* or *diffraction plane*. The orientations of these planes in the crystal are described by the so called *Miller indices* h, k and l with $h, k, l \in \mathbf{Z}$ (see pic. 2). The reciprocal base vectors $\mathbf{a^*_1}$, $\mathbf{a^*_2}$, $\mathbf{a^*_3}$ create the reciprocal space with: $\mathbf{a^*_i} * \mathbf{a_j} = \delta_{ij}$ with $\delta_{ij}=1$ for $i=j$ and $\delta_{ij}=0$ for $i \neq j$. Each point $\mathbf{Q}=h*\mathbf{a^*_1} + k*\mathbf{a^*_2} + l*\mathbf{a^*_3}$ represents the normal vector of

a (*hkl*) Plane. Each plane cuts the crystal lattice along its base vectors $\mathbf{a_1}$, $\mathbf{a_2}$ and $\mathbf{a_3}$ at $1/h^*\mathbf{a_1}$, $1/k^*\mathbf{a_2}$ and $1/l^*\mathbf{a_3}$. A Miller index of zero means that the referring axis will be cut in infinity. Thus, the lattice plane is parallel to this axis.

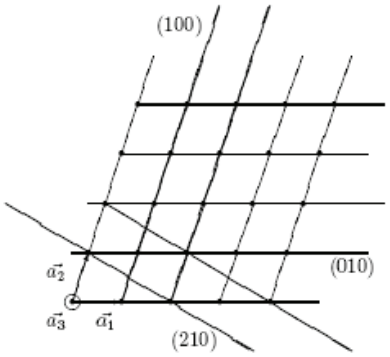

Fig. 2: Different lattice planes in a crystal lattice, $\mathbf{a_3}$ = viewing direction

The atoms in a unit cell are not rigidly fixed at their positions. They oscillate around their positions (e.g. thermal excitation). A simple description for this is the model of coupled springs. In this model atoms are connected via springs whose forces describe the binding forces between the atoms (e.g. van der Waals, Coulomb, valence). The back driving forces of the springs are proportional to the deviation x_i of the atoms from their mean positions and to the force constant D, thus. $F = -D^*\Delta x$ (harmonic approximation).
Therefore, the atoms oscillate with $x_i = A_i^*\sin(\nu^*t)$ around their mean positions with the frequency ν and the amplitude A_i. Both, ν and A_i are influenced by the force constant D_j of the springs and the atomic masses m_i of the neighbouring atoms. The resulting lattice oscillations are called phonons in reference to the photons (light particles) in optics, which as well transport energy in dependence of their frequency. A more complex and detailed description of phonons in dependence on the lattice structure and the atomic reciprocal effects is given in lattice dynamics. In the harmonic approximation the displacements of an atom can be described with an oszillation ellipsoid. This ellipsoid describes the preferred spacial volume in which the atom is placed. Its so called mean square displacements (MSD) U^i_{jk} represent the different sizes of the ellipsoid along the different main directions *j, k* in the crystal. The simplest case is a sphere with the isotrope MSD B_i. In the next paragraph MSD are discussed from the point of view of diffraction analysis.
A full description of a single crystal contains information about lattice class, lattice constants and unit cell, space group and all atomic positions and their MSD. If the occupancy of one or more positions is not exactly 100%, e.g. for a mixed crystal or a crystal with deficiencies there has to be used also an occupancy factor.

3 Structure Determination with Diffraction

3.1 Introduction

Diffraction means coherent elastic scattering of a wave on a crystal. Because of the quantum mechanical wave/particle dualism x-rays as well as neutron beams offer the requested wave properties:

Electrons: $E = h\nu$; $\lambda = c/\nu$
Neutrons: $E_{kin} = 1/2 * m_n * v^2 = h\nu = p^2/2m_n$; $\lambda = h/p$; $p \sim \sqrt{(m_n k_B T)}$

h: Planck's constant; ν: oscillation frequency; λ: wavelength; c: light speed; p: impact; m_n: neutron mass; k_B: Boltzmann constant; T: temperature

Only the cross section partners are different (x-rays: scattering on the electron shell of the atoms, neutrons: core (and magnetic) scattering) as explained in detail below. In scattering experiments informations about structural properties are hidden in the scattering intensities I.
In the following pages we will discuss only elastic scattering ($\lambda_{in}=\lambda_{out}$). The cross section of the radiation with the crystal lattice can be described as following:
Parallel waves of the incoming radiation with constant λ are diffracted by lattice planes which are ordered parallel with a constant distance of d. This is very similar to a light beam reflected by a mirror. The angle of the diffracted beam is equal to the angle of the incoming beam, thus the total angle between incoming and outgoing beam is 2Θ (see fig. 3).

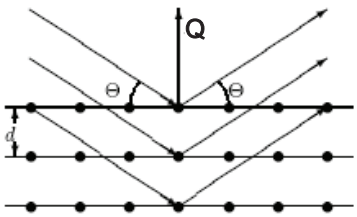

Fig. 3: Scattering on lattice planes

The overlap of all beams diffracted by a single lattice plane results in constructive interference only if the combination of the angle Θ, lattice plane distance d and wavelength λ meet Braggs law:

$$\mathbf{2}d\ \mathbf{sin}\Theta = \lambda$$

The largest distance $d_{hkl} = |\mathbf{Q}|$ of neighboured parallel lattice planes in a crystal is never larger than the largest lattice constant $d_{hkl} \leq \max(a; b; c)$. Therefore, it can only be a few Å or less. For a cubic unit cell ($a = b = c$; $\alpha = \beta = \gamma = 90°$) this means:
$d_{hkl} = a/\sqrt{(h^2+k^2+l^2)}$

With increasing scattering angle also the indices (hkl) increase while the lattice plane distances shrink with a lower limit of $d_{min} = \lambda/2$. Therefore, scattering experiments need

wavelengths λ in the same order of magnitude of the lattice constants or below. This is equal to x-ray energies of about 10 keV or neutron energies about 25 meV (thermal neutrons).

Ewald Construction: In reciprocal space each Bragg reflex is represented by a point $\mathbf{Q} = h^*\mathbf{a}^*_1 + k^*\mathbf{a}^*_2 + l^*\mathbf{a}^*_3$. A scattered beam with the wave vector $\mathbf{k}$ fulfills Braggs law if the relationship $\mathbf{k} = \mathbf{k_0} + \mathbf{Q}$, $|\mathbf{k}|=|\mathbf{k_0}|=1/\lambda$ is true, as shown in fig. 4. During an experiment the available reciprocal space can be described by an Ewald sphere with a diameter of $2/\lambda$ and the (000)-point as cross point of $\mathbf{k_0}$ direction and the centre of the diameter of the sphere. The rotation of the crystal lattice during the diffraction experiment is equal to a synchronous movement of the reciprocal lattice around the (000)-point. If Braggs law is fulfilled, one point (*h k l*) of the reciprocal lattices lies exactly on the Ewald sphere. The angle between the **k**-vektor and the $\mathbf{k_0}$-vektor is 2Θ. The limited radius of $1/\lambda$ of the Ewald sphere limits also the visibility of (*h k l*) reflections to $|\mathbf{Q}| < 2/\lambda$.

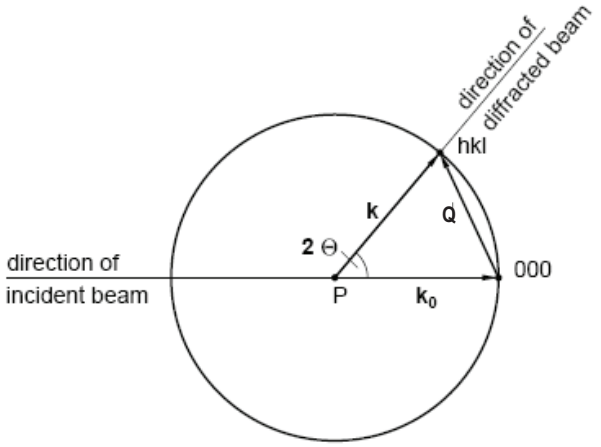

Fig. 4: Ewald construction

Determination of the Unit Cell: Following Braggs law the scattering angle 2Θ varies (for λ=const.) according to the lattice distance d_{hkl}. Thus for a given λ and known scattering angles 2Θ one can calculate the different *d* values of the different layers in the lattice of a crystal. With this knowledge is is possible to determine the lattice system and the lattice constants of the unit cell (although not always unambigously!).

Atomic Positions in the Unit Cell: The outer shape of a unit cell does not tell anything about the atomic positions $\mathbf{x_i}=(x_i\ y_i\ z_i)$ of each atom in this cell. To determine the atomic positions one has to measure also the quantities of the different reflection intensities of a crystal. This works because of the relationship between the intensities of Bragg reflections and the specific cross section of the selected radiation with each element in a unit cell. Generally one can use the following formula for the intensity of a Bragg reflection (*h k l*) with **Q** (kinetic scattering theory):

$$I_{hkl} \sim |F_{hkl}|^2 \text{ with } F_{hkl} = \sum^n_{i=1} s_i(\mathbf{Q}) \exp(2\pi\imath(hx_i+ky_i+lz_i))$$

The scattering factor F is a complex function describing the overlap of the scattering waves of each atom i (n per unit cell). $s_i(\mathbf{Q})$ describes the scattering strength of the i-th atom on its position $\mathbf{x}_i$ in dependence of the scattering vector $\mathbf{Q}$, which depends on the character of cross section as described below.
In this context one remark concerning statistics: For measurements of radiation the statistical error σ is the square root of the number of measured events, e.g. x-ray or neutron particles. Thus, 100 events yield an error of 10% while 10,000 events yield an error of only 1%!

Mean Square Displacements (MSD): Thermal movement of atoms around their average positions reduce the Bragg intensities during a diffraction experiment. The cause for this effect is the reduced probability density and therefore reduced cross section probability at the average positions. For higher temperatures (above a few Kelvin) the MSD B_i of the atoms increase linearly to the temperature T, this means $B \sim T$. Near a temperature of 0 K the MSD become constant with values larger than zero (zero point oscillation of the quantum mechanical harmonic oscillator).
Thus, the true scattering capability s_i of the i-th atom in a structure has to be corrected by an angle-dependent factor (the so called Debye-Waller factor):

$$s_i(\mathbf{Q}) \rightarrow s_i(\mathbf{Q}) * \exp(-B_i(\sin \Theta_{\mathbf{Q}}/\lambda)^2)$$

This Debye-Waller factor decreases with increasing temperatures and yields an attenuation of the Bragg reflection intensities. At the same time this factor becomes significantly smaller with larger $\sin\Theta/\lambda \sim |\mathbf{Q}|$. Therefore, especially reflections with large indices loose a lot of intensity. The formula for anisotropic oscillations around their average positions looks like this:

$$s_i(\mathbf{Q}) \rightarrow s_i(\mathbf{Q}) * \exp(-2\pi^2(U^i_{11}\, h^2a^{*2} + U^i_{22}\, k^2b^{*2} + U^i_{33}\, l^2c^{*2} + \\ + 2U^i_{13}\, hl\, a^*c^* + 2U^i_{12}\, hk\, a^*b^* + 2U^i_{23} kl\, b^*c^*))$$

The transformation between B and U_{eq} (from the U_{ij} calculated isotropic MSD for a sphere with identical volume) yields $B = 8\pi^2 U_{eq}$.
For some structures the experimentally determined MSD are significantly larger than from the harmonic calculations of the thermal movement of the atoms expected. Such deviations can have different reasons: Static local deformations like point defects, mixed compounds, anharmonic oscillations or double well potentials where two energetically equal atomic positions are very near to each other and therefore distribute the same atom over the crystal with a 50%/50% chance to one or the other position. In all those cases an additional contribution to the pure Debye-Waller factor can be found which yields an increased MSD. Therefore in the following text only the term MSD will be used to avoid misunderstandings.

3.2 Comparison of X-ray and Neutron Radiation

X-Ray Radiation interacts as electromagnetic radiation only with the electron density in a crystal. This means the shell electrons of the atoms as well as the chemical binding. The scattering capability s (atomic form factor $f(\sin\Theta/\lambda)$) of an atom depends on the number Z of its shell electrons ($f(\sin(\Theta=0)/\lambda) = Z$). To be exact, $f(\sin(\Theta)/\lambda)$ is the Fourier transform of the radial electron density distribution $n_e(r)$: $f(\sin(\Theta)/\lambda) = s \int_0^\infty 4\pi^2 n_e(r)\, \sin(\mu r)/\mu r\, dr$ with $\mu = 4\pi\sin(\Theta)/\lambda$. Heavy atoms with many electrons contribute much stronger to reflection

intensities ($I \sim Z^2$) than light atoms with less electrons. The reason for the sinΘ/λ-dependence of f is the diameter of the electron shell, which has the same order of magnitude as the wavelength λ. Because of this there is no pointlike scattering centre. Thus, for large scattering angles the atomic form factors vanish and also the reflection intensities relying on them. The atomic form factors are derived from theoretical spherical electron density functions (e. g. Hartree-Fock). The resulting f(sinΘ/λ)-curves of all elements (separated for free atoms and ions) are listed in the international tables. Their analytical approximation can be described by seven coefficients (c; a_i; b_i; $1 \leq i \leq 3$) , see [1].

Neutron Radiation radiation interacts with the cores and the magnetic moments of atoms. The analogon to the x-ray form factor (the scattering length b) is therefore not only dependent on the element but the isotope. At the same time b-values of elements neighboured in the periodic table can differ significantly. Nevertheless, the scattering lengths do not differ around several orders of magnitude like in the case of the atomic form factors f . Therefore, in a compound with light and heavy atoms the heavy atoms do not dominate necessarily the Bragg intensities. Furthermore the core potential with a diameter about 10^{-15}Å is a pointlike scattering centre and thus the scattering lengths b_n become independent of the Bragg angle and sinΘ/λ respectively. This results in large intensities even at large scattering angles. The magnetic scattering lengths b_m can generate magnetic Bragg intensities comparable in their order of magnitude to the intensities of core scattering. On the other hand side the magnetic scattering lengths are strongly dependent on the sinΘ/λ value due to the large spacial distribution of magnetic fields in a crystal. Therefore, it is easy to measure magnetic structures with neutrons and to separate them from the atomic structure.

Comparison: In summary in the same diffraction experiment the different character of x-ray and neutron radiation yield different pieces of information that can be combined. x-rays yield electron densities in a crystal while neutron scattering reveals the exact atomic positions. This fact is important because for polarised atoms the core position and the centre of gravity of electron densities are not identical any more. In compounds with light an heavy atoms structural changes driven by light elements need additional diffraction experiments with neutrons to reveal their influence and accurate atomic positions respectively. One has to take into account also that for x-rays intensitied depend twice on sinΘ/λ. Once bye the atomic form factor f, and twice by the temperature dependent Debye-Waller factor (see above). The first dependence vanishes if using neutron diffraction with b=const. and decouples the structure factors from the influence of the MSD. In general this yields much more accurate MSD U_{ij} especially for the light atoms and might be helpful to reveal double well potentials.

3.3 Special Effects

From the relation $I \sim |F|^2$ one can derive that the scattering intensities of a homogenous illuminated sample increases with its volume. But there are other effects than MSD that can attenuate intensities. These effects can be absorption, extinction, polarization and the Lorentz factor:

Absorption can be described by the Lambert-Beer law:

$I = I_0 \exp(-\mu x)$, μ/cm^{-1} = linear absorption coefficient, x/cm = mean path through sample

The linear absorption coefficient is an isotropic property of matter and depends on the wavelength and kind of radiation. For x-rays penetration depths are only a few millimetre or below (e.g. for silicon with $\mu_{MoK\alpha}$=1.546 mm^{-1}, $\mu_{CuK\alpha}$=14.84 mm^{-1} with penetration depths of 3 mm and 0.3 mm respectively). This limits transmission experiments to sample diameter of typically below 0.3 mm. To correct bias of intensities due to different scattering paths through the sample one has to measure accurately the sample size in all directions. Even for sphere liek samples the mean path lenghts depend on 2Θ! In addition the sample environment must have an extraordinary small absorption
Thermal neutrons have for most elements a penetration depth of several centimeters. Thus, sample diameters of several millimeters and large and complex sample environments (furnaces, magnets, etc.) can be used. On the other hand side one needs sufficiently large samples for neutron diffraction which is often a delicate problem.

Extinction reduces also radiation intensities. But the character is completely different form that of absorption. In principle extinction can be explained quite easily by taking into account that each diffracted beam can be seen as a new primary beam for the neighbouring lattice planes. Therefore, the diffracted beam becomes partially backscattered towards the direction of the very first primary beam (Switch from kinetic to dynamic scattering theory!). Especially for very strong reflections this effect can reduce intensities dramatically (up to 50% and more). Condition for this effect is a merely perfect crystal.
Theoretical models which include a quantitative description of the extinction effect were developed from Zachariasen (1962) and Becker and Coppens [2, 3, 4, 5, 6]. These models base on an ideal spherical mosaic crystal with a very perfect single crystal (primary Extinction) or different mosaic blocks with almost perfect alignment (secundary Extinction) to describe the strength of the extinction effect. In addition, it is possible to take into account anisotropic extinction effect if the crystal quality is also anisotropic. Nowadays extinction correction is included in most refinement programs [7]. In general extinction is a problem of sample quality and size and therefore more commonly a problem for neutron diffraction and not so often for x-ray diffraction with much smaller samples and larger absorption.

Polarisation*:* X-ray radiation is electromagnetic radiation. Therefore, the primary beam of an x-ray tube is not polarized. The radiation hits the sample under an diffraction angle of Θ where it can be separated into two waves of same intensity, firstly with an electrical field vector parallel $E_{||}$ and secondly perpendicular $E_{\perp}$ towards the Θ-axis. Whilst the radiation with $E_{||}$ will not be attenuated the radiation with $E_{\perp}$ will be attenuated with $E_{\perp} \rightarrow \cos(2\Theta)\, E_{\perp}$. The polarization factor P for the attenuation has then the following formula ($I \sim E^2$):

$$P = (1+\cos(2\Theta)^2)/2$$

Additional optical components like monochromator crystals also have an impact on the polarization and have to be taken into account accordingly.

Lorentz factor: The Lorentz factor L is a purely geometrical factor. It describes that during an ω- and Θ-scan respectively of Bragg reflections towards higher 2Θ values for the same angular speed $\Delta\omega/\Delta t$ an effectively elongated stay of the sample in the reflection position results.:

$$L = 1/\sin(2\Theta)$$

This has to be taken into account for any kind of radiation in an diffraction experiment.

3.4 Summary of Theory of Method

The different interactions of x-ray and neutron radiation with the atoms in a crystal make neutrons in general the better choice for a diffraction experiment. But on the other hand one has to take into account the available flux of x-rays and neutrons respectively. The flux of modern neutron sources like the Heinz Maier-Leibnitz neutron source (FRM II) is spread around a broad spectrum of neutron energies. In a sharp band of energies/wavelengths, e.g. $\Delta\lambda/\lambda<10^{-3}$, there is the flux of neutrons several order of magnitude smaller than the flux of x-rays of a corresponding synchtrotron source or x-ray tube in the laboratory. The reason for this is the fact that in an x-ray tube most x-rays are generated in a small energy band, the characteristic lines of the tube target (K_α, K_β, etc.). Additional metal foil used as filter allow to cut off unwanted characteristic lines which yields quasi monochromatic radiation of a single wavelength.
To use neutrons around a small energy band one has to use monochromator crystals. This reduces significantly the number of available neutrons for the diffraction experiment. Thus, the weak flux of neutrons and the weak cross section of neutrons with matter has to be compensated with large sample sizes of several millimeters. For the same reason the monochromatization of the neutrons is normally chosen to be not too sharp (resolution about $\Delta\lambda/\lambda\approx10^{-2}$ for neutrons, $\Delta\lambda/\lambda\approx10^{-5} - 10^{-6}$ for synchrotron).

3.5 From Measurement to Model

To get a structural model from the experimentally collected integral Bragg intensities one needs several steps in advance. Firstly on has to make sure that all reflections are measured properly (no shading, no $\lambda/2$-contamination, no Umweganregung (Renninger-effect)). Damaged reflections have to be excluded from further treatment.
During data refinement not only the quantities of the relative intensities but also their errors are taken into account. The total statistical error σ of an integral intensity I_{obs} of a single reflection is calculated as following:

$$\sigma^2 = I_{obs} + I_{background} + (k\, I_{total})^2$$

The part $\sigma_0^2 = I_{total}$, $I_{total} = I_{obs} + I_{background}$ refers to the error caused by counting statistics. It contains as well the effective intensity Iobs as well as the contribution of the background. But there are other effects that influence the reproducibility of a measurement (and thus the total error), e.g. specific errors of the instrumental adjustment. Those errors are collected in the so called *McCandlish-Factor k* and contribute to the total error. Therefore, the total error cannot drop below the physically correct limit of the experiment and thus the impact of strong reflections does not become exaggerated in the refinement. The determination of *k* is done by measurent the same set of reflections several times during an experiment (the so called standard reflections). The mean variation of the averaged value represents *k*. In addition, the repeated measurement of standard reflections offers the opportunity to notice unwanted changes during experiment like structural changes or release from the sample holder.

To make sure the comparisability of all reflections with each other, all intensities and errors are normalized to the same time of measurement (or monitor count rate) and undergo the Lorentz and (in the x-ray case) polarization correction.
Finally in advance of the data refinement there can be done an numerical (e.g. with DataP, [8]) or an empirical absoprtion if necessary. The quality of a measurement is checked in advance of the data refinement by comparing symmetry equivalent reflections and systematic extinctions to confirm the Laue group and space group symmetry. The result is written as internal *R*-value:

$$R_{\mathrm{int}} = (\sum_{k=1}^{m}(\sum_{j=1}^{n_k} (<I_k>- I_j)^2))/ (\sum_{k=1}\sum_{j=1}^{n_k}(I_j^2)_k)$$

R_{int} represents the mean error of a single reflection j of a group k of n_k symmetry equivalent reflections, corresponding to its group and the total number m of all symmetrically independent groups. Therefore R_{int} is also a good mark to check the absorption correction. After these preliminary steps one can start the final data refinement.
At the beginning one has to develop a structural model. The problem with that is that we measure only the absolut values $|F_{\mathrm{hkl}}|$ and not the complete structure factor $F_{\mathrm{hkl}} = |F_{hkl}|\exp(\imath\phi)$ including its phase ϕ. Therefore, generally the direct fouriertransform of the reflection information F_{hkl} from reciprocal space into the density information ρ in the direct space (electron density for x-rays, probability density of atomic cores for neutrons) with

$$\rho(\mathbf{x}) \sim \sum_h\sum_k\sum_l F_{hkl} \exp(-2\pi(hx+ky+lz))$$

not possible. This can be done only by direct methods like patterson, heavy atom method or anomal dispersion for x-rays.
In the so called refinement program a given structural model (space group, lattice constants, atomic form factors, MSD, etc.) are compared with the experimental data and fitted. In a leas squares routine those programs try to optimize (typically over several cycles) the free parameters to reduce the difference between the calculated structure factors F_{calc} and intensities $|F_{calc}|^2$ respectively and the experimentally found F_{obs} and $|F_{\mathrm{obs}}|^2$ respectively. To quantisize the quality of measurement there are several values in use:

1. *unweighted R*-value: $R_{\mathrm{u}} = \sum_{hkl} |F_{\mathrm{obs}}^2-F_{\mathrm{calc}}^2|/\sum_{hkl} F_{\mathrm{obs}}^2$
This value gives the alignment of the whole number of reflections without their specific errors.

2. weighted *R*-value: $R_{\mathrm{w}} = (\sum_{hkl} w (F_{\mathrm{obs}}^2-F_{\mathrm{calc}}^2)^2)/\sum_{hkl} w F_{\mathrm{obs}}^4$
This value represents the alignment of the whole number of reflections including their specific errors or weights ($w\sim 1/\sigma^2$). Sometimes weights are adopted in a way to suppress unwanted influence of the refinement algorithm by weak or badly defined reflections. Be aware that such corrections have to be done extremely carefully because otherwise the refinement adopts the data to the selected structural model and not the model to the experimental data!

3. *Goodness of Fit S*: $S^2 =(\sum_{hkl} w (F_{\mathrm{obs}}^2-F_{\mathrm{calc}}^2)/(n_{\mathrm{hkl\text{-}reflections}} - n_{\mathrm{free\ parameter}})$

S should have a value near one if the weighting scheme and the structure model fit to the experimental data set.

4 Sample Section

4.1 Introduction

$La_{2-x}Sr_xCuO_4$ is one of the cuprate superconductors with K_2NiF_4- structure for whose discovery the noble prize was granted in 1988 (Bednorz and Müller [9]) . Pure La_2CuO_4 is an isolator. Doping with earth alcali metals (Ca^{2+}, Sr^{2+}, Ba^{2+}) on the La^{3+} lattice positions generates in dependence of the degree of doping superconductivity. Sr doping of x=0.15 yields a maximum T_c of 38 K.

Pure La_2CuO_4 undergoes at $T_{t\text{-}o}$=530 K a structural phase transition from the tetragonal high temperature phase (HTT)

F4/mmm: a=b=5.384 Å, c=13.204 Å, α=β=γ=90° at T=540 K

to the orthorhombic low temperature phase (LTO)

Abma: a=5.409 Å, b=5.357 Å, c=13.144 Å, α=β=γ=90° at room temperature.

The phase transition temperature $T_{t\text{-}o}$ drops for $La_{2-x}Sr_xCuO_4$ with increased doping and disappears above x=0.2.

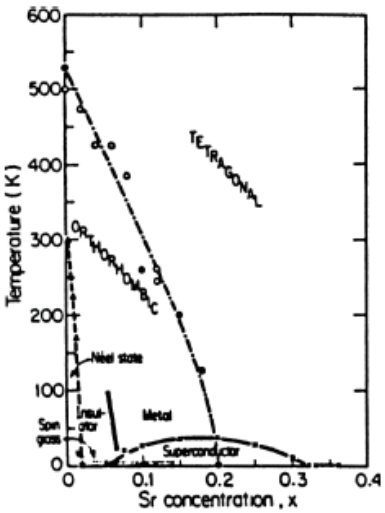

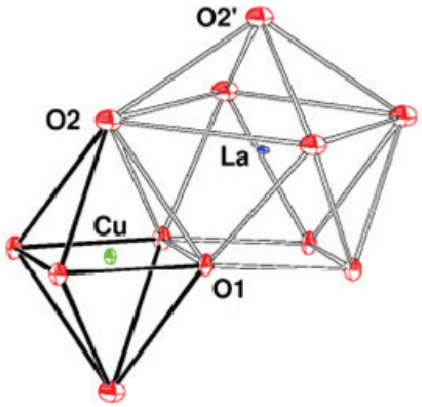

Fig.. 6 left: J. Birgenau, G. Shirane, HTC Superconductors I, World Scientific (1989)
Fig.. 6 right: Stuctural parts of La_2CuO_4 in the LTO phase

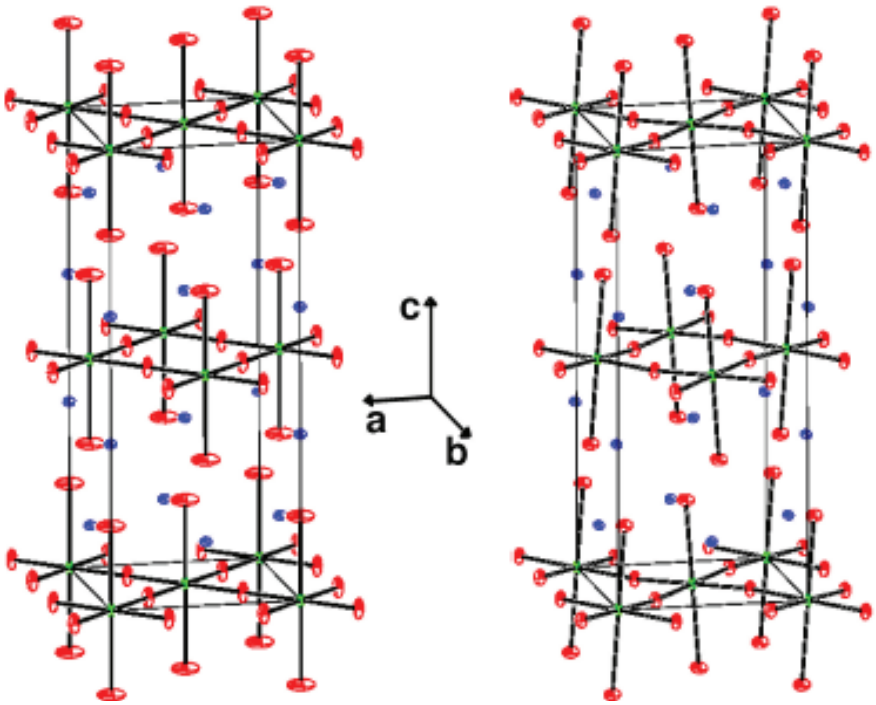

Fig. 7 left: tetragonal HTT phase Fig. 7 right: orthorhombic´LTO phase

4.2 Twinning

During the transition into the low temperature phase the CuO_6 octahedrons are tilted around their [010] axis. Thus, the two axes of identical length in the HTT phase, a_1 and a_2, are not equal in the LTO phase anymore. Instead, the longer one becomes the new *a* axis, the shorter one becomes the *b* axis. Whether a_1 or a_2 becomes the new a axis depends only on the real structure of the crystal, for instance grain boundaries or point defects. Therefore, one can find two equivalent crystallographic space groups in the LTO phase:

Abma ($a_1 \rightarrow a$, $a_2 \rightarrow b$) and B*mab* ($a_1 \rightarrow b$, $a_2 \rightarrow a$)

For the structure factors in the LTO is valid:

$F_{\mathrm{Abma}}(hkl)=F_{\mathrm{Bmab}}(khl)$

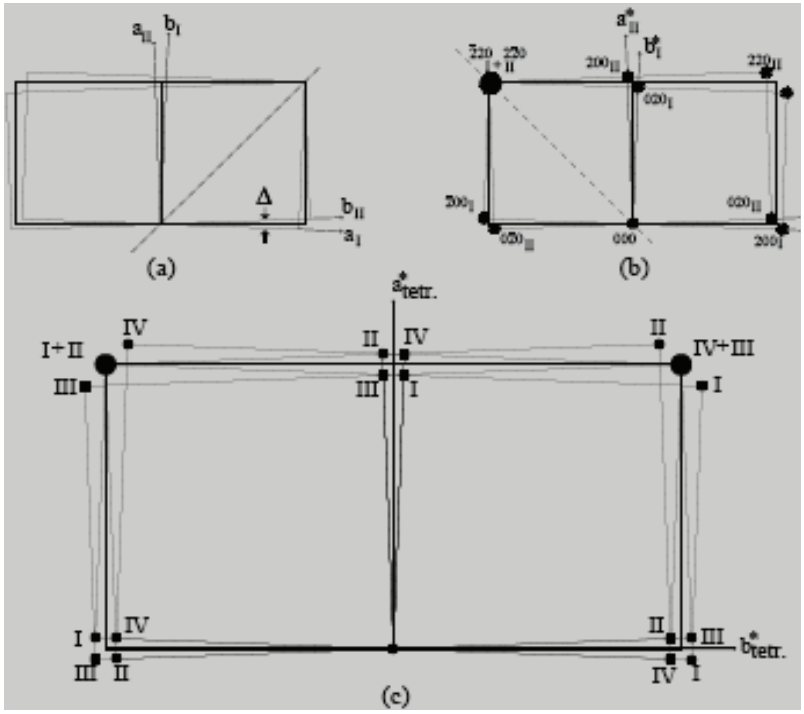

Fig. 8
(a) orthorhombic distortion with twinning correspondint to a (1-10) mirroring
(b) corresponding reciprocal lattice
(c) Overlay of (110)- and (1-10)-mirroring in reciprocal space

In the HTT phase only reflections with *h, k, l* of equal parity (*g* for even, *u* for uneven) are allowed - (*uuu*) and (*ggg*). They are called in the following main structrure reflections.
In the LTO phase additional reflections occur, called super structure reflections: In the *Abma*-Structure (*ugg*), l≠0 and (*guu*), in the *Bmab* structure (*gug*), l≠0 and(*ugu*).
Forbidden in both the HTT and the LTO phase are (*uug*), (*ggu*), (*ug*0) and (*gu*0).
These extinction rules will become important later.
In the real structure of the crystal there exist four domain types in total. They are separated into two pairs with the couple $Abma_1/Bmab_1$ (I/II) with the (1-10) mirror plane as grain boundary and the couple $Abma_2/Bmab_2$ (III/IV) with the (110) mirror plane as grain boundary (fig. 8).

The following overlaps of reflections result from this twinning:

- No splitting of the (00l) reflections,
- triple splitting of the (hh0) reflections
- fourfold splitting of the (h00) reflections.

An equal distribution of the volumetric portion of each single domain yields a ratio of intensities of 1:2:1 for the triple splitting. The distance $\Delta\omega$ between the centre and the side

peaks of a (*hkl*) reflex gives because of $(a+b)/2 = a_{1/2}$ an information about the orthorhombic *a/b* splitting. For the triple splitting of a (*hh*0) reflex is valid:

$\Delta\omega = 90°\text{-}2\arctan(b/a)$

Thus, although the real crystal is twinned, one can quantify the orthorhombic distortion.

The intensity contribution of the single domains corresponding to the whole intensity of a reflection can be described (taking into account the incoherent overlap of single intensities and the volumetric portions V_{A1} to V_{B2} of the domains) as follows:

$$I_{obs}(hkl) = I_{Abma1}(hkl) + I_{Bmab1}(hkl) + I_{Abma2}(hkl) + I_{Bmab2}(khl) \text{ or}$$

$$V_{total}|F_{obs}(hkl)|^2 = V_{A1}|F_{Abma1}(hkl)|^2 + V_{B1}|F_{Bmab1}(hkl)|^2 + V_{A2}|F_{Abma2}(hkl)|^2 + V_{B2}|F_{Bmab2}(hkl)|^2$$

$$= (V_{A1} + V_{A2})|F_{Abma1}(hkl)|^2 + (V_{B1}| + V_{B2})|F_{Bmab1}(hkl)|^2$$

$$= V_{total}\ \{\alpha|F_{Abma}(hkl)|^2 + (1\text{-}\alpha)\ |F_{Abma}(khl)|^2\ \}$$

with α being the relative portion of the volume of *Abma* domains to the crystal..

Because of the extinction rules in the LTO phase for the super structure reflections is valid: $I_{obs}(hkl) \sim \alpha|F_{Abma}(hkl)|^2$ for *Abma* and $I_{obs}(hkl) \sim (1\text{-}\alpha)|F_{Abma}(khl)|^2$ for *Bmab*. Thus, one can classify directly intensities to the volumetric portions of the domain types *Abma* and *Bmab* respectively. Therefore, by using one single additional parameter α to describe the relation between the twins in the structure one can determine the orthorhombic single crystal structure! This holds true although the Bragg reflections contain contributions of up to four different domains.

4.3 Oxygen Position

The oxygen atoms undergo the largest shift of their positions during the transition to the LTO phase. For the structure factor of a any Bragg reflection forbidden in *F4/mmm* is valid:

$$F(hkl) \sim \sum_i s_i \exp(-2\pi\imath(hx_i+ky_i+lz_i) = F(hkl)_{\text{apex oxygen}}+F(hkl)_{\text{in plane oxygen}}+F(hkl)_{\text{structure w/o O}}$$
$$\rightarrow F(hkl)_{\text{apex oxygen}}+F(hkl)_{\text{in plane oxygen}}$$

In the LTO phase the atomic position of the apex oxygens is (x 0 z), the atomic position for the in-plane oxygens is (1/4 1/4 -z). This yields the following intensities for the superstructure reflections:

$F(hkl)_{\text{apex oxygen}} = \cos(2\pi hx)\cos(2\pi lz)$ for h even or
$F(hkl)_{\text{apex oxygen}} = \sin(2\pi hx)\cos(2\pi lz)$ for h uneven

In the case of x-rays the form factor $f_i \sim Z_i$, Z_i=order number is much smaller for oxygen (Z=16) than for Cu (Z=29) and La (Z=57). Because of $I_{\text{obs}}(hkl) \sim |F(hkl)|^2$ the oxygen shift is hardly measurable. In the case of neutrons the scattering lengths b_i of all atoms are in the same order of magnitude (b_{O}=5.803 barn, b_{Cu}= barn, b_{La}= barn, 1 barn = 10^{-24} cm^{-2}). Therefore, the intensity contribution of the oxygen atoms increeases in relation to the other elements in the structure and allows a much more precise determination of the structural change of the oxygen positions

5 Preparatory Exercises

1. What is the fundamental difference between powder/single crystal diffraction and what are the advantages and disadvantages of both techniques (Compare d-values and orientations of different reflections in a cubic structure)?
2. What is wrong with fig. 2?
3. Which reflections are not allowed in a face centered structure (structure factor)?
4. There is no space group F4/mmm in the international tables. Why (Which other space group in the international tables yields the same pattern in direct space)?

6 Experiment Procedure

During this practical course not all physical and technical aspects of structure analysis with neutrons can be discussed in detail. Nevertheless this course is supposed point out the basic similarities and dissimilarities of x-rays and neutron radiation as well as their specific advantages and disadvantages in general and referring to single crystal diffraction. The sample selected for this practical course is most suitable for this purpose because of its special crystallographic peculiarities.

6.1 The Instrument

Fig. 5 shows the typical setup of a single crystal diffractometer with a single detector. Outgoing from the radiation source a primary beam defined by primary optics (in our case the beam tube) reaches the single crystal sample. If one lattice plane (*hkl*) fulfills Braggs laws, the scattered beam, called secondary beam, leaves the sample under an angle 2Θ to the primary beam. The exact direction of this beam depends only on the relative orientation of the sample to the primary beam.
For the diffractometer shown in fig. 5 the movement of the neutron detector is limited to a horizontal rotation around the 2Θ axis. Thus, only those reflections can be measured, whose scattering vector **Q** lies exactly in the plane defined by the source, the sample and detector circle. This plane is also called scattering plane.

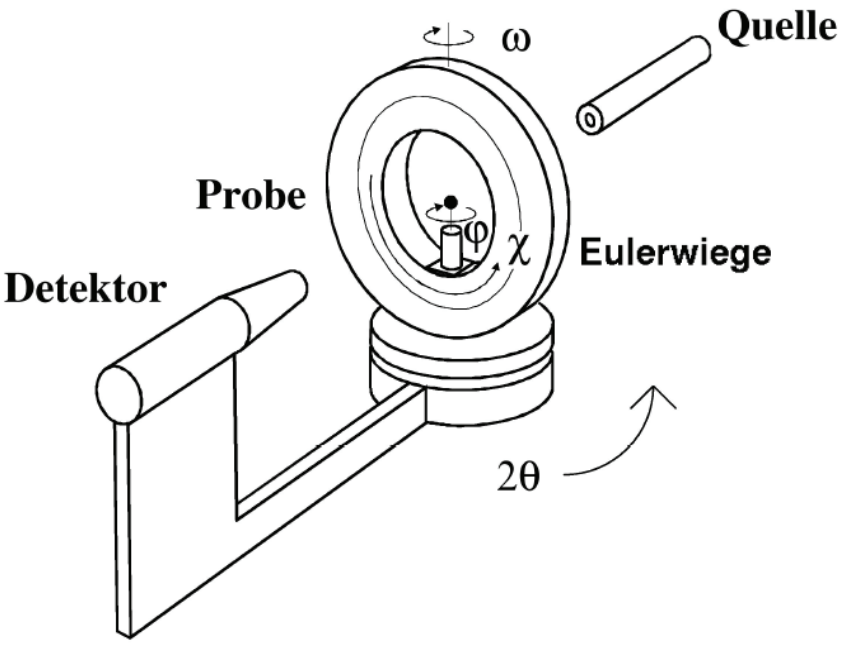

Fig. 5: Scheme of a single crystal diffractometer

To direct the secondary beam towards the detector position one has to orient the sample around the three axes ω, χ and ϕ. These three axes allow a virtually random orientation of the crystal in the primary beam. During the experiment the sample has to stay exactly in the cross point of all four axes (2Θ, ω, χ and ϕ) and the primary beam. Additionally, for 2Θ = ω = χ = ϕ = 0° the primary beam direction and the χ axis on one hand side and the 2Θ-, ω- and ϕ-axes on the other hand side are identical while the angle between the primary beam and the 2Θ-is exactly 90°. Because of the four rotational axes (2Θ, ω, χ, ϕ) this kind of single crystal diffractometer is often called four circle diffractometer. Another often used geometry - the so called κ-Geometrie - will not be discussed in detail here.

Further details of the experimental setup:

1. Beam source and primary optics: The primary beam is generated by a suitable source (x-rays: x-ray tube, synchrotron; neutrons: nuclear fission, spallation source). The primary optics defines the path of the beam to the sample in the Eulerian cradle. Furthermore, the primary optics defines the beam diameter using slits to make it fit to the sample size for homogeneous illumination. This homogeneity is very important because the quality of the data refinement relies on the comparison of the intensity ratios between the different reflections measured during an experiment. Wrong ratios caused by inhomogeneous illumination can yield wrong structural details! Other components of the primary optics are collimators defining beam divergence and filters or monochromators which define the wavelength λ of the radiation.

2. Sample and sample environment: The sample position is fixed by the centre of the Eulerian cradle which is defined by the cross point of the axes ω, χ and ϕ. As described above, the cradle itself has in combination with the ω-circle the task to orient the sample according to the observed reflection in a way that it hits the detector. The sample itself is mounted on a goniometer head. This head allows the adjustment of the sample in all three directions **x***;* **y***;* **z**, via microscope or camera. To avoid scattering from the sample environment and goniometer head the sample is usually connected to the head via a thin glass fibre (x-rays) or aluminum pin (neutrons). This reduces significantly background scattering. For experiments at high or low temperatures adjustable cooling or heating devices can be mounted into the Eulerian cradle.

3. Secondary optics and detector: The 2Θ arm of the instrument hold the detector which – in the ideal case – catches only radiation scattered from the sample and transforms it to an electrical signal. There exists a variety of detectors, single detectors and position sensitive 1D and 2D detectors. Area detectors have a large sensitive area that allows the accurate observation of spatial distribution of radiation. Other components of the secondary optics are slits and collimators or analyser (as optional units). They fulfil the task to shield the detector from unwanted radiation like scattering from sample environment, scattering in air, wrong wavelengths or flourescence

6.2 Sequence of measurement in Theory

1. Centering: In advance of the planned scientific program (profile analysis, Bragg data collection) the orientation of the sample in relation to the coordinate system of the diffractometer has to be determined. First of all the sample has to be centered optically to assure a homogeneous illumination of the sample. Afterwards, a reflection search routine has to be started to optimize the intensity of a found reflection by moving several angles after each other.
In many cases there are some structural informations like the unit cell and hkl values of strong reflections available from previous studies, e.g. from powder diffraction, thus, one can limit the reflection search to 2Θ values around these strong reflections to spare some time and to classify manually the found reflections with the correct indices.

2. Determination of orienting matrix and lattice constants: The comparison of the **Q** vectors of the found and centered reflections yields generally one or more suggestions for a suitable unit cell. This is done by a least squares routine minimizing the error bars between the calculated and measured **Q** vectors. This method allows to determine accurately the orientation matrix $\mathbf{M_o} = (\mathbf{a^*}\ \mathbf{b^*}\ \mathbf{c^*})^T$ of the sample relative to the coordinate system of the diffractometer and the lattice constants of the unit cell.

On HEiDi the axes are defined as following: **x**=primary beam, **z** || 2Θ axis, **y**=**z** x **x**.
A proposed unit cell is only acceptable if all experimentally found reflections can be indexed with integer *hkl* , this means $\mathbf{Q} = (h\ k\ l)^*\mathbf{M_o}$. In addition the found reflection intensities *I* offer a course check, e.g. whether extinction rules are followed or intensities of symmetrically identical reflections are identical.

3. Profile analyses and scan types: During profile analysis reflex profiles are analysed via so called ω scans. During this scan the sample is turned for *n* steps around a center position ω_0. This scan makes different crystallites in one large sample visible. In addition one has to take into account that even in perfectly grown crystals there are grain boundaries and slight mismatches of the crystallites. These mosaic blocks are perfect crystals whose orientations are misaligned only a few tenths of a degree or less. By the way, the axis position $2\Theta/2=\Theta=\omega$ is called the bisecting orientation of the Eulerian cradle.
As long as the vertical aperture is large enough, a rotation of the crystal around a ω_0, that is equivalent to the ideal Θ_0 Bragg angle of a reflex allows to catch the intensity portion of each crystallite in the sample in the neutron detector on the fixed 2Θ position, even those that can only be found for slightly differing ω. Therefore, a crystal with large mosaicity gives measurable intensities over a broader ω area than a perfect crystal. Thus it gives a broader reflex profile. Also the tearing and cracking of a crystal creates broad but unregular profiles.
Beside the crystal quality also the instrumental resolution limits the measurable profile widths in the following sense: The divergence of a primary beam in real experiment is limited, for instance to 0.2°.
If a reflection fulfills Bragg's Law at Θ, the total divergence is a convolution of the divergence of the primary beam *and* the mosaicity/divergence of the sample. Thus, the reflection profile will never be sharper than the divergence of the primary beam itself.
In addition one has to take into account that for larger diffraction angles a fixed detector window will not be sufficient to catch the whole reflection intensities during a rocking scan.

For a given spectrum $\Delta\lambda/\lambda$ of the primary beam, with increasing scattering angle Θ angular range $\Delta\Theta$ increases with $\sin(\Delta\Theta/2)=\tan(\Theta)*\Delta\lambda/\lambda$ for which all wavelengths in the interval $\lambda\pm\Delta\lambda/2$ fulfilling Bragg's law are distributed. Because of the limited width of the detector window this yields a cut off of intensities for larger scattering angles for ω-scans.
To compensate this cut off effect it is necessary to begin at a certain 2Θ-angle to move the detector window with the ω-angle.. This can be done by so called $\omega/2\Theta$-scans. The start position of this 2Θ range depends on the primary beam divergence and sample quality and has to be checked individually for each sample.

4. Collection of Bragg reflections: If a sample was found good after the described preliminary studies one can start with the Bragg data collection. In this data collection all (or selected) reflections in a given 2Θ intervall are collected automatically. The usual strategy follows the rule „Only as many as necessary". This means the following: On one hand side the quality of the measured reflections has to fulfil certain standards (like small standard deviations σ and a good shape of the profiles) to reach an acceptable accuracy. On the other side there is only a limited amount of time available for each reflection due to the huge number of them (up to several thousands). and the limited beam time. A rule of thumb is therefore to measure about 10 non symmetry equivalent reflections for each free parameter used in the data refinement to get the correct structure. To achieve this goal a typical algorithm is to do a prescan with t_{min} per point of measurement in combination with a given larger (e.g. I/σ=4 and 25%, respectively) and a smaller (e.g. I/σ=20 and 5%, respectively) relative error limit. t_{min} is chosen in a way that the statistics of strong reflections is fine already after the prescan. Weak reflections are also noticed in the prescan and stored as weak reflections without additional treatment. Reflections in between get an additional chance to improve their statistics by performing a second scan with a limited amount of time up to t_{max}-t_{min}. This method avoids to spend unreasonable beam time to weak reflections which will not help to improve the quality of the structure model.

6.3 and in Practice

1. **Adjust optically the sample in the neutron beam :** Alignment of the sample in the rotational centre of the instrument. This is necessary for a homogeneous illumination of the sample for all possible orientations.

2. **Search for Bragg reflections and center them, , "Reflex centering**": Sample and detector position are controlled by a special diffractometer software. The main goal is to find suitable angular positions for the detector first and afterwards for the sample to get a measurable signal. Afterwards the orientation of the sample in the Eulerian cradle have to be optimized for maximum intensity.

3. **Analyse profiles of selected reflections:** Study different reflex profiles and reveal the impact of twinning

4. **Determine the orthorhombic lattice parameters a, b and c**: Estimate the misalignment of *a* and *b* in reference to $a_{1/2}$ in the real tetragonal cell.

5. **Determine the average tetragonal unit cell**: The centering of different reflections allows the calculation of all lattice constants including the averaged tetragonal parameters.

6. **Observe super structure reflections:** Measuring pairs of (*hkl*)/(*khl*) allows the estimation of the volumetric contribution of each single domain to the whole crystal.

7. **Select measurement parameters for Bragg data collection:** In order to optimize the number and statistical quality of collected Bragg reflections suitable scan parameters (time/step, no. of steps, stepwidths, etc.) have to be determined.

8. **Collect a Bragg data set**

6.4 Data analysis

After having measured a Bragg data set one has to do the final step, the alignment of model and measurement:

1. **Data Reduction:** In this process the measured reflection profiles are analysed and reduced to a simple list of all measured reflections and their integrated intensities including error bars and some other useful information. This so-called *hkl*-list is the base for the next step:

2. **Structure refinement:** Here the measured *hkl*-list and our structure model are combined to determine structural details like atomic positions and mean square displacements.

7 Experiment-Related Exercises

1. Why is the optical adjustment of the sample so important?
2. How large is the *a/b*-splitting at room temperature (=|*a*-*b*|/(*a*+*b*))?
3. What is the benefit/enhancement of studying the room temperature structure with neutrons instead of X-rays?

References

[1] Th. Hahn (ed.), Space-group symmetry, International Tables for Crystallography Vol. A, Kluver Academic Publishers (2006).
[2] W.H. Zachariasen, Acta Cryst. 18 703 (1965).
[3] W.H. Zachariasen, Acta Cryst. 18 705 (1965).
[4] P. Coppens and W.C. Hamilton, Acta Cryst. A 26 71-83 (1970).
[5] P.J. Becker and P. Coppens, Acta Cryst. A 30 129-147 (1974).
[6] P.J. Becker and P. Coppens, Acta Cryst. A 30 148-153 (1974).
[7] U.H. Zucker, E. Perrenthaler, W.F. Kuhs, R. Bachmann and H. Schulz J. of Appl. Crystallogr., 16 358 (1983).
[8] P. Coppens, W.C. Hamilton, S. Wilkins, M.S. Lehmann and Savariault, Datap, http://www.ill.fr/data treat/diftreat.html#single (1999).
[9] J. Bednorz and K. Müller, Z. Phys. B 64 189 (1986).

Literature

N.W. Ashcroft and N.D. Mermin, Festkörperphysik, Oldenbourg 2001.

H. Ibach and H. Lüth, Festkörperphysik, Einführung in die Grundlagen, 6. Edition Springer 2002.

C. Kittel, Einführung in die Festkörperphysik, 10. Edition, Oldenbourg 1993.

W. Borchardt-Ott, Kristallographie. Eine Einführung für Naturwissenschaftler, 6. Auflage Springer 2002.

W. Kleber, Einführung in die Kristallographie, Oldenbourg 1998

H. Dachs, Neutron Diffraction, Springer (1978)

D.J. Dyson, X-Ray and Electron Diffraction Studies in Material Science, Maney Pub 2004.

C. Giacovazzo, Fundamentals of Crystallography, 2nd Ed., Oxford University Press 2002.

L.A. Aslanov, Crystallographic Instrumentation, Oxford University Press 1998.

M.T. Dove, Structure and Dynamics. An Atomic View of Materials, Oxford University Press 2003. W. Clegg, Crystal Structure Analysis. Principles and Practice, Oxford University Press 2001.

Appendix (Tables and space groups from [1])

3.1. SPACE-GROUP DETERMINATION AND DIFFRACTION SYMBOLS

Table 3.1.4.1. *Reflection conditions, diffraction symbols and possible space groups (cont.)*

ORTHORHOMBIC, Laue class *mmm* ($2/m\ 2/m\ 2/m$) (*cont.*)

Reflection conditions								Laue class *mmm* ($2/m\ 2/m\ 2/m$)		
								Point group		
hkl	0*kl*	*h*0*l*	*hk*0	*h*00	0*k*0	00*l*	Extinction symbol	222	*mm*2 *m*2*m* 2*mm*	*mmm*
	$k+l$	l	k		k	l	*Pncb*			*Pncb* (50)
	$k+l$	l	$h+k$	h	k	l	*Pncn*			*Pncn* (52)
	$k+l$	$h+l$		h	k	l	*Pnn* –		***Pnn2*** (34)	***Pnnm*** (58)
	$k+l$	$h+l$	h	h	k	l	*Pnna*			***Pnna*** (52)
	$k+l$	$h+l$	k	h	k	l	*Pnnb*			*Pnnb* (52)
	$k+l$	$h+l$	$h+k$	h	k	l	*Pnnn*			***Pnnn*** (48)
$h+k$	k	h	$h+k$	h	k		*C* – – –	***C222*** (21)	***Cmm2*** (35) *Cm2m* (38) *C2mm* (38)	***Cmmm*** (65)
$h+k$	k	h	$h+k$	h	k	l	*C*– –2_1	***C222$_1$*** (20)		
$h+k$	k	h	h, k	h	k		*C*– –(*ab*)		*Cm2e* (39) *C2me* (39)	***Cmme*** (67)
$h+k$	k	h, l	$h+k$	h	k	l	*C*–*c* –		***Cmc2$_1$*** (36) *C2cm* (40)	***Cmcm*** (63)
$h+k$	k	h, l	h, k	h	k	l	*C*–*c*(*ab*)		*C2ce* (41)	***Cmce*** (64)
$h+k$	k, l	h	$h+k$	h	k	l	*Cc* – –		*Ccm*2_1 (36) *Cc2m* (40)	*Ccmm* (63)
$h+k$	k, l	h	h, k	h	k	l	*Cc* –(*ab*)		*Cc2e* (41)	*Ccme* (64)
$h+k$	k, l	h, l	$h+k$	h	k	l	*Ccc* –		***Ccc2*** (37)	***Cccm*** (66)
$h+k$	k, l	h, l	h, k	h	k	l	*Ccc*(*ab*)			***Ccce*** (68)
$h+l$	l	$h+l$	h	h		l	*B* – – –	*B*222 (21)	*Bmm*2 (38) *Bm2m* (35) *B2mm* (38)	*Bmmm* (65)
$h+l$	l	$h+l$	h	h	k	l	*B*–2_1–	*B*22_12 (20)		
$h+l$	l	$h+l$	h, k	h	k	l	*B*– –*b*		*Bm*2_1b (36) *B2mb* (40)	*Bmmb* (63)
$h+l$	l	h, l	h	h		l	*B* –(*ac*)–		*Bme*2 (39) *B2em* (39)	*Bmem* (67)
$h+l$	l	h, l	h, k	h	k	l	*B* –(*ac*)*b*		*B2eb* (41)	*Bmeb* (64)
$h+l$	k, l	$h+l$	h	h	k	l	*Bb* – –		*Bbm*2 (40) *Bb*2_1m (36)	*Bbmm* (63)
$h+l$	k, l	$h+l$	h, k	h	k	l	*Bb*–*b*		*Bb2b* (37)	*Bbmb* (66)
$h+l$	k, l	h, l	h	h	k	l	*Bb*(*ac*)–		*Bbe*2 (41)	*Bbem* (64)
$h+l$	k, l	h, l	h, k	h	k	l	*Bb*(*ac*)*b*			*Bbeb* (68)
$k+l$	$k+l$	l	k		k	l	*A* – – –	*A*222 (21)	***Amm2*** (38) *Am2m* (38) *A2mm* (35)	*Ammm* (65)
$k+l$	$k+l$	l	k	h	k	l	*A*2_1– –	*A*2_122 (20)		
$k+l$	$k+l$	l	h, k	h	k	l	*A*– –*a*		***Am2a*** (40) *A*2_1ma (36)	*Amma* (63)
$k+l$	$k+l$	h, l	k	h	k	l	*A*–*a* –		***Ama2*** (40) *A*2_1am (36)	*Amam* (63)
$k+l$	$k+l$	h, l	h, k	h	k	l	*A*–*aa*		*A2aa* (37)	*Amaa* (66)
$k+l$	k, l	l	k		k	l	*A*(*bc*)– –		***Aem2*** (39) *Ae2m* (39)	*Aemm* (67)
$k+l$	k, l	l	h, k	h	k	l	*A*(*bc*)– *a*		*Ae2a* (41)	*Aema* (64)
$k+l$	k, l	h, l	k	h	k	l	*A*(*bc*)*a* –		***Aea2*** (41)	*Aeam* (64)
$k+l$	k, l	h, l	h, k	h	k	l	*A*(*bc*)*aa*			*Aeaa* (68)
$h+k+l$	$k+l$	$h+l$	$h+k$	h	k	l	*I* – – –	***I222*** (23) ***I2$_1$2$_1$2$_1$*** (24)	***Imm2*** (44) *Im2m* (44)	***Immm*** (71)

3. DETERMINATION OF SPACE GROUPS

Table 3.1.4.1. *Reflection conditions, diffraction symbols and possible space groups* (*cont.*)

ORTHORHOMBIC, Laue class *mmm* ($2/m\ 2/m\ 2/m$) (*cont.*)

Reflection conditions								Laue class *mmm* ($2/m\ 2/m\ 2/m$)		
								Point group		
hkl	0*kl*	*h*0*l*	*hk*0	*h*00	0*k*0	00*l*	Extinction symbol	222	*mm*2 *m*2*m* 2*mm*	*mmm*
									*I*2*mm* (44)	
$h+k+l$	$k+l$	$h+l$	h,k	h	k	l	$I--(ab)$		*Im*2*a* (46)	***Imma*** (74)
									*I*2*mb* (46)	*Immb* (74)
$h+k+l$	$k+l$	h,l	$h+k$	h	k	l	$I-(ac)-$		***Ima*2** (46)	*Imam* (74)
									*I*2*cm* (46)	*Imcm* (74)
$h+k+l$	$k+l$	h,l	h,k	h	k	l	$I-cb$		*I*2*cb* (45)	*Imcb* (72)
$h+k+l$	k,l	$h+l$	$h+k$	h	k	l	$I(bc)--$		*Iem*2 (46)	*Iemm* (74)
									*Ie*2*m* (46)	
$h+k+l$	k,l	$h+l$	h,k	h	k	l	$Ic-a$		*Ic*2*a* (45)	*Icma* (72)
$h+k+l$	k,l	h,l	$h+k$	h	k	l	$Iba-$		***Iba*2** (45)	***Ibam*** (72)
$h+k+l$	k,l	h,l	h,k	h	k	l	$Ibca$			***Ibca*** (73)
										Icab (73)
$h+k,h+l,k+l$	k,l	h,l	h,k	h	k	l	$F---$	***F*222** (22)	*Fmm*2 (42)	***Fmmm*** (69)
									*Fm*2*m* (42)	
									*F*2*mm* (42)	
$h+k,h+l,k+l$	k,l	$h+l=4n;\ h,l$	$h+k=4n;\ h,k$	$h=4n$	$k=4n$	$l=4n$	$F-dd$		*F*2*dd* (43)	
$h+k,h+l,k+l$	$k+l=4n;\ k,l$	h,l	$h+k=4n;\ h,k$	$h=4n$	$k=4n$	$l=4n$	$Fd-d$		*Fd*2*d* (43)	
$h+k,h+l,k+l$	$k+l=4n;\ k,l$	$h+l=4n;\ h,l$	h,k	$h=4n$	$k=4n$	$l=4n$	$Fdd-$		***Fdd*2** (43)	
$h+k,h+l,k+l$	$k+l=4n;\ k,l$	$h+l=4n;\ h,l$	$h+k=4n;\ h,k$	$h=4n$	$k=4n$	$l=4n$	$Fddd$			***Fddd*** (70)

* Pair of space groups with common point group and symmetry elements but differing in the relative location of these elements.

3.1. SPACE-GROUP DETERMINATION AND DIFFRACTION SYMBOLS

Table 3.1.4.1. *Reflection conditions, diffraction symbols and possible space groups* (*cont.*)

TETRAGONAL, Laue classes $4/m$ and $4/mmm$ (*cont.*)

Reflection conditions							Extinction symbol	Laue class						
								$4/m$			$4/mmm$ ($4/m\ 2/m\ 2/m$)			
								Point group						
hkl	*hk*0	0*kl*	*hhl*	00*l*	0*k*0	*hh*0		4	$\bar{4}$	$4/m$	422	4*mm*	$\bar{4}2m$ $\bar{4}m2$	$4/mmm$
	$h+k$	k			k		$Pnb-$							*P*4/*nbm* (125)
	$h+k$	k	l	l	k		*Pnbc*							*P*4$_2$/*nbc* (133)
	$h+k$	l		l	k		$Pnc-$							*P*4$_2$/*ncm* (138)
	$h+k$	l	l	l	k		*Pncc*							*P*4/*ncc* (130)
	$h+k$	$k+l$		l	k		$Pnn-$							*P*4$_2$/*nmm* (134)
	$h+k$	$k+l$	l	l	k		*Pnnc*							*P*4/*nnc* (126)
$h+k+l$	$h+k$	$k+l$	l	l	k		$I---$	*I*4 (79)	*I*$\bar{4}$ (82)	*I*4/*m* (87)	*I*422 (97)	*I*4*mm* (107)	*I*$\bar{4}$2*m* (121)	*I*4/*mmm* (139)
													I$\bar{4}$*m*2 (119)	
$h+k+l$	$h+k$	$k+l$	l	$l=4n$	k		$I4_1--$	*I*4$_1$ (80)			*I*4$_1$22 (98)			
$h+k+l$	$h+k$	$k+l$	‡	$l=4n$	k	h	$I--d$					*I*4$_1$*md* (109)	*I*$\bar{4}$2*d* (122)	
$h+k+l$	$h+k$	k,l	l	l	k		$I-c-$					*I*4*cm* (108)	*I*$\bar{4}$*c*2 (120)	*I*4/*mcm* (140)
$h+k+l$	$h+k$	k,l	‡	$l=4n$	k	h	$I-cd$					*I*4$_1$*cd* (110)		
$h+k+l$	h,k	$k+l$	l	$l=4n$	k		$I4_1/a--$			*I*4$_1$/*a* (88)				
$h+k+l$	h,k	$k+l$	‡	$l=4n$	k	h	$Ia-d$							*I*4$_1$/*amd* (141)
$h+k+l$	h,k	k,l	‡	$l=4n$	k	h	*Iacd*							*I*4$_1$/*acd* (142)

† Pair of enantiomorphic space groups, *cf.* Section 3.1.5.
‡ Condition: $2h+l=4n;\ l$.

International Tables for Crystallography (2006). Vol. A, Space group 139, pp. 478–479.

$I4/mmm$ D_{4h}^{17} $4/mmm$ Tetragonal

No. 139 $I\ 4/m\ 2/m\ 2/m$ Patterson symmetry $I4/mmm$

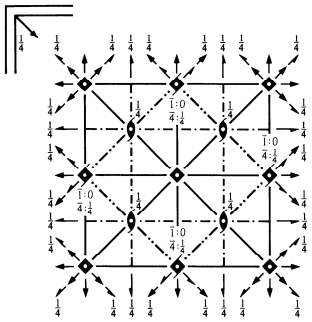

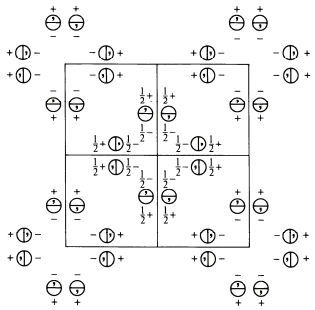

Origin at centre $(4/mmm)$

Asymmetric unit $0 \le x \le \frac{1}{2};\quad 0 \le y \le \frac{1}{2};\quad 0 \le z \le \frac{1}{4};\quad x \le y$

Symmetry operations

For $(0,0,0)+$ set

(1) 1	(2) 2 $0,0,z$	(3) 4^+ $0,0,z$	(4) 4^- $0,0,z$
(5) 2 $0,y,0$	(6) 2 $x,0,0$	(7) 2 $x,x,0$	(8) 2 $x,\bar{x},0$
(9) $\bar{1}$ $0,0,0$	(10) m $x,y,0$	(11) $\bar{4}^+$ $0,0,z;\ 0,0,0$	(12) $\bar{4}^-$ $0,0,z;\ 0,0,0$
(13) m $x,0,z$	(14) m $0,y,z$	(15) m $x,\bar{x},z$	(16) m x,x,z

For $(\frac{1}{2},\frac{1}{2},\frac{1}{2})+$ set

(1) $t(\frac{1}{2},\frac{1}{2},\frac{1}{2})$	(2) $2(0,0,\frac{1}{2})$ $\frac{1}{4},\frac{1}{4},z$	(3) $4^+(0,0,\frac{1}{2})$ $0,\frac{1}{2},z$	(4) $4^-(0,0,\frac{1}{2})$ $\frac{1}{2},0,z$
(5) $2(0,\frac{1}{2},0)$ $\frac{1}{4},y,\frac{1}{4}$	(6) $2(\frac{1}{2},0,0)$ $x,\frac{1}{4},\frac{1}{4}$	(7) $2(\frac{1}{2},\frac{1}{2},0)$ $x,x,\frac{1}{4}$	(8) 2 $x,\bar{x}+\frac{1}{2},\frac{1}{4}$
(9) $\bar{1}$ $\frac{1}{4},\frac{1}{4},\frac{1}{4}$	(10) $n(\frac{1}{2},\frac{1}{2},0)$ $x,y,\frac{1}{4}$	(11) $\bar{4}^+$ $\frac{1}{2},0,z;\ \frac{1}{2},0,\frac{1}{4}$	(12) $\bar{4}^-$ $0,\frac{1}{2},z;\ 0,\frac{1}{2},\frac{1}{4}$
(13) $n(\frac{1}{2},0,\frac{1}{2})$ $x,\frac{1}{4},z$	(14) $n(0,\frac{1}{2},\frac{1}{2})$ $\frac{1}{4},y,z$	(15) c $x,\frac{1}{2},\bar{x},z$	(16) $n(\frac{1}{2},\frac{1}{2},\frac{1}{2})$ x,x,z

Maximal non-isomorphic subgroups *(continued)*

IIa
[2] $P4_2/nmc$ (137) 1; 2; 7; 8; 11; 12; 13; 14; (3; 4; 5; 6; 9; 10; 15; 16) + $(\frac{1}{2},\frac{1}{2},\frac{1}{2})$
[2] $P4_2/mnm$ (136) 1; 2; 7; 8; 9; 10; 15; 16; (3; 4; 5; 6; 11; 12; 13; 14) + $(\frac{1}{2},\frac{1}{2},\frac{1}{2})$
[2] $P4_2/nnm$ (134) 1; 2; 5; 6; 11; 12; 15; 16; (3; 4; 7; 8; 9; 10; 13; 14) + $(\frac{1}{2},\frac{1}{2},\frac{1}{2})$
[2] $P4_2/mmc$ (131) 1; 2; 5; 6; 9; 10; 13; 14; (3; 4; 7; 8; 11; 12; 15; 16) + $(\frac{1}{2},\frac{1}{2},\frac{1}{2})$
[2] $P4/nmm$ (129) 1; 2; 3; 4; 13; 14; 15; 16; (5; 6; 7; 8; 9; 10; 11; 12) + $(\frac{1}{2},\frac{1}{2},\frac{1}{2})$
[2] $P4/mnc$ (128) 1; 2; 3; 4; 9; 10; 11; 12; (5; 6; 7; 8; 13; 14; 15; 16) + $(\frac{1}{2},\frac{1}{2},\frac{1}{2})$
[2] $P4/nnc$ (126) 1; 2; 3; 4; 5; 6; 7; 8; (9; 10; 11; 12; 13; 14; 15; 16) + $(\frac{1}{2},\frac{1}{2},\frac{1}{2})$
[2] $P4/mmm$ (123) 1; 2; 3; 4; 5; 6; 7; 8; 9; 10; 11; 12; 13; 14; 15; 16

IIb none

Maximal isomorphic subgroups of lowest index

IIc [3] $I4/mmm$ ($\mathbf{c}' = 3\mathbf{c}$) (139); [9] $I4/mmm$ ($\mathbf{a}' = 3\mathbf{a}, \mathbf{b}' = 3\mathbf{b}$) (139)

Minimal non-isomorphic supergroups

I [3] $Fm\bar{3}m$ (225); [3] $Im\bar{3}m$ (229)

II [2] $C4/mmm$ ($\mathbf{c}' = \frac{1}{2}\mathbf{c}$) ($P4/mmm$, 123)

CONTINUED **No. 139** $I4/mmm$

Generators selected (1); $t(1,0,0)$; $t(0,1,0)$; $t(0,0,1)$; $t(\frac{1}{2},\frac{1}{2},\frac{1}{2})$; (2); (3); (5); (9)

Positions

Multiplicity, Wyckoff letter, Site symmetry			Coordinates $(0,0,0)+$ $(\frac{1}{2},\frac{1}{2},\frac{1}{2})+$				Reflection conditions
							General:
32	o	1	(1) x,y,z (5) $\bar{x},y,\bar{z}$ (9) $\bar{x},\bar{y},\bar{z}$ (13) $x,\bar{y},z$	(2) $\bar{x},\bar{y},z$ (6) $x,\bar{y},\bar{z}$ (10) $x,y,\bar{z}$ (14) $\bar{x},y,z$	(3) $\bar{y},x,z$ (7) $y,x,\bar{z}$ (11) $y,\bar{x},\bar{z}$ (15) $\bar{y},\bar{x},z$	(4) $y,\bar{x},z$ (8) $\bar{y},\bar{x},\bar{z}$ (12) $\bar{y},x,\bar{z}$ (16) y,x,z	hkl : $h+k+l=2n$ $hk0$: $h+k=2n$ $0kl$: $k+l=2n$ hhl : $l=2n$ $00l$: $l=2n$ $h00$: $h=2n$
							Special: as above, plus
16	n	$.m.$	$0,y,z$ $0,y,\bar{z}$	$0,\bar{y},z$ $0,\bar{y},\bar{z}$	$\bar{y},0,z$ $y,0,\bar{z}$	$y,0,z$ $\bar{y},0,\bar{z}$	no extra conditions
16	m	$..m$	x,x,z $\bar{x},x,\bar{z}$	$\bar{x},\bar{x},z$ $x,\bar{x},\bar{z}$	$\bar{x},x,z$ $x,x,\bar{z}$	$x,\bar{x},z$ $\bar{x},\bar{x},\bar{z}$	no extra conditions
16	l	$m..$	$x,y,0$ $\bar{x},y,0$	$\bar{x},\bar{y},0$ $x,\bar{y},0$	$\bar{y},x,0$ $y,x,0$	$y,\bar{x},0$ $\bar{y},\bar{x},0$	no extra conditions
16	k	$..2$	$x,x+\frac{1}{2},\frac{1}{4}$ $\bar{x},\bar{x}+\frac{1}{2},\frac{3}{4}$	$\bar{x},\bar{x}+\frac{1}{2},\frac{1}{4}$ $x,x+\frac{1}{2},\frac{3}{4}$	$\bar{x}+\frac{1}{2},x,\frac{1}{4}$ $x+\frac{1}{2},\bar{x},\frac{3}{4}$	$x+\frac{1}{2},\bar{x},\frac{1}{4}$ $\bar{x}+\frac{1}{2},x,\frac{3}{4}$	hkl : $l=2n$
8	j	$m2m.$	$x,\frac{1}{2},0$	$\bar{x},\frac{1}{2},0$	$\frac{1}{2},x,0$	$\frac{1}{2},\bar{x},0$	no extra conditions
8	i	$m2m.$	$x,0,0$	$\bar{x},0,0$	$0,x,0$	$0,\bar{x},0$	no extra conditions
8	h	$m.2m$	$x,x,0$	$\bar{x},\bar{x},0$	$\bar{x},x,0$	$x,\bar{x},0$	no extra conditions
8	g	$2mm.$	$0,\frac{1}{2},z$	$\frac{1}{2},0,z$	$0,\frac{1}{2},\bar{z}$	$\frac{1}{2},0,\bar{z}$	hkl : $l=2n$
8	f	$..2/m$	$\frac{1}{4},\frac{1}{4},\frac{1}{4}$	$\frac{3}{4},\frac{3}{4},\frac{1}{4}$	$\frac{3}{4},\frac{1}{4},\frac{1}{4}$	$\frac{1}{4},\frac{3}{4},\frac{1}{4}$	hkl : $k,l=2n$
4	e	$4mm$	$0,0,z$	$0,0,\bar{z}$			no extra conditions
4	d	$\bar{4}m2$	$0,\frac{1}{2},\frac{1}{4}$	$\frac{1}{2},0,\frac{1}{4}$			hkl : $l=2n$
4	c	$mmm.$	$0,\frac{1}{2},0$	$\frac{1}{2},0,0$			hkl : $l=2n$
2	b	$4/mmm$	$0,0,\frac{1}{2}$				no extra conditions
2	a	$4/mmm$	$0,0,0$				no extra conditions

Symmetry of special projections

Along [001] $p4mm$
$\mathbf{a}' = \frac{1}{2}(\mathbf{a}-\mathbf{b})$ $\mathbf{b}' = \frac{1}{2}(\mathbf{a}+\mathbf{b})$
Origin at $0,0,z$

Along [100] $c2mm$
$\mathbf{a}' = \mathbf{b}$ $\mathbf{b}' = \mathbf{c}$
Origin at $x,0,0$

Along [110] $p2mm$
$\mathbf{a}' = \frac{1}{2}(-\mathbf{a}+\mathbf{b})$ $\mathbf{b}' = \frac{1}{2}\mathbf{c}$
Origin at $x,x,0$

Maximal non-isomorphic subgroups

I	[2] $I\bar{4}2m$ (121)	(1; 2; 5; 6; 11; 12; 15; 16)+
	[2] $I\bar{4}m2$ (119)	(1; 2; 7; 8; 11; 12; 13; 14)+
	[2] $I4mm$ (107)	(1; 2; 3; 4; 13; 14; 15; 16)+
	[2] $I422$ (97)	(1; 2; 3; 4; 5; 6; 7; 8)+
	[2] $I4/m11$ ($I4/m$, 87)	(1; 2; 3; 4; 9; 10; 11; 12)+
	[2] $I2/m2/m1$ ($Immm$, 71)	(1; 2; 5; 6; 9; 10; 13; 14)+
	[2] $I2/m12/m$ ($Fmmm$, 69)	(1; 2; 7; 8; 9; 10; 15; 16)+

(*Continued on preceding page*)

International Tables for Crystallography (2006). Vol. A, Space group 69, pp. 316–318.

$F\,m\,m\,m$ D_{2h}^{23} $m\,m\,m$ Orthorhombic

No. 69 $F\ 2/m\ 2/m\ 2/m$ Patterson symmetry $F\,m\,m\,m$

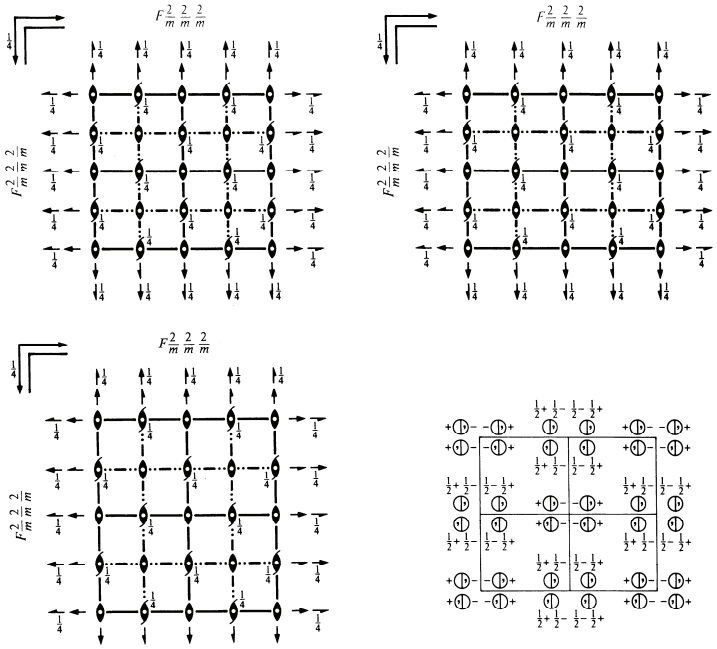

Origin at centre $(m\,m\,m)$

Asymmetric unit $0 \le x \le \frac{1}{4};\quad 0 \le y \le \frac{1}{4};\quad 0 \le z \le \frac{1}{2}$

Symmetry operations

For $(0,0,0)+$ set

(1) 1 (2) 2 $0,0,z$ (3) 2 $0,y,0$ (4) 2 $x,0,0$
(5) $\bar{1}$ $0,0,0$ (6) m $x,y,0$ (7) m $x,0,z$ (8) m $0,y,z$

For $(0,\frac{1}{2},\frac{1}{2})+$ set

(1) $t(0,\frac{1}{2},\frac{1}{2})$ (2) $2(0,0,\frac{1}{2})$ $0,\frac{1}{4},z$ (3) $2(0,\frac{1}{2},0)$ $0,y,\frac{1}{4}$ (4) 2 $x,\frac{1}{4},\frac{1}{4}$
(5) $\bar{1}$ $0,\frac{1}{4},\frac{1}{4}$ (6) b $x,y,\frac{1}{4}$ (7) c $x,\frac{1}{4},z$ (8) $n(0,\frac{1}{2},\frac{1}{2})$ $0,y,z$

For $(\frac{1}{2},0,\frac{1}{2})+$ set

(1) $t(\frac{1}{2},0,\frac{1}{2})$ (2) $2(0,0,\frac{1}{2})$ $\frac{1}{4},0,z$ (3) 2 $\frac{1}{4},y,\frac{1}{4}$ (4) $2(\frac{1}{2},0,0)$ $x,0,\frac{1}{4}$
(5) $\bar{1}$ $\frac{1}{4},0,\frac{1}{4}$ (6) a $x,y,\frac{1}{4}$ (7) $n(\frac{1}{2},0,\frac{1}{2})$ $x,0,z$ (8) c $\frac{1}{4},y,z$

For $(\frac{1}{2},\frac{1}{2},0)+$ set

(1) $t(\frac{1}{2},\frac{1}{2},0)$ (2) 2 $\frac{1}{4},\frac{1}{4},z$ (3) $2(0,\frac{1}{2},0)$ $\frac{1}{4},y,0$ (4) $2(\frac{1}{2},0,0)$ $x,\frac{1}{4},0$
(5) $\bar{1}$ $\frac{1}{4},\frac{1}{4},0$ (6) $n(\frac{1}{2},\frac{1}{2},0)$ $x,y,0$ (7) a $x,\frac{1}{4},z$ (8) b $\frac{1}{4},y,z$

CONTINUED **No. 69** ***F m m m***

Generators selected (1); $t(1,0,0)$; $t(0,1,0)$; $t(0,0,1)$; $t(0,\frac{1}{2},\frac{1}{2})$; $t(\frac{1}{2},0,\frac{1}{2})$; (2); (3); (5)

Positions

Multiplicity, Wyckoff letter, Site symmetry			Coordinates $(0,0,0)+$	$(0,\frac{1}{2},\frac{1}{2})+$	$(\frac{1}{2},0,\frac{1}{2})+$	$(\frac{1}{2},\frac{1}{2},0)+$	Reflection conditions
							General:
32	*p*	1	(1) x,y,z (5) $\bar{x},\bar{y},\bar{z}$	(2) $\bar{x},\bar{y},z$ (6) $x,y,\bar{z}$	(3) $\bar{x},y,\bar{z}$ (7) $x,\bar{y},z$	(4) $x,\bar{y},\bar{z}$ (8) $\bar{x},y,z$	hkl : $h+k,h+l,k+l=2n$ $0kl$: $k,l=2n$ $h0l$: $h,l=2n$ $hk0$: $h,k=2n$ $h00$: $h=2n$ $0k0$: $k=2n$ $00l$: $l=2n$
							Special: as above, plus
16	*o*	. . *m*	$x,y,0$	$\bar{x},y,0$	$x,\bar{y},0$	$\bar{x},\bar{y},0$	no extra conditions
16	*n*	. *m* .	$x,0,z$	$\bar{x},0,z$	$x,0,\bar{z}$	$\bar{x},0,\bar{z}$	no extra conditions
16	*m*	*m* . .	$0,y,z$	$0,\bar{y},z$	$0,y,\bar{z}$	$0,\bar{y},\bar{z}$	no extra conditions
16	*l*	2 . .	$x,\frac{1}{4},\frac{1}{4}$	$\bar{x},\frac{3}{4},\frac{1}{4}$	$\bar{x},\frac{3}{4},\frac{3}{4}$	$x,\frac{1}{4},\frac{3}{4}$	hkl : $h=2n$
16	*k*	. 2 .	$\frac{1}{4},y,\frac{1}{4}$	$\frac{3}{4},\bar{y},\frac{1}{4}$	$\frac{3}{4},\bar{y},\frac{3}{4}$	$\frac{1}{4},y,\frac{3}{4}$	hkl : $h=2n$
16	*j*	. . 2	$\frac{1}{4},\frac{1}{4},z$	$\frac{3}{4},\frac{1}{4},\bar{z}$	$\frac{3}{4},\frac{3}{4},\bar{z}$	$\frac{1}{4},\frac{3}{4},z$	hkl : $h=2n$
8	*i*	*m m* 2	$0,0,z$	$0,0,\bar{z}$			no extra conditions
8	*h*	*m* 2 *m*	$0,y,0$	$0,\bar{y},0$			no extra conditions
8	*g*	2 *m m*	$x,0,0$	$\bar{x},0,0$			no extra conditions
8	*f*	2 2 2	$\frac{1}{4},\frac{1}{4},\frac{1}{4}$	$\frac{3}{4},\frac{3}{4},\frac{3}{4}$			hkl : $h=2n$
8	*e*	. . 2/*m*	$\frac{1}{4},\frac{1}{4},0$	$\frac{3}{4},\frac{1}{4},0$			hkl : $h=2n$
8	*d*	. 2/*m* .	$\frac{1}{4},0,\frac{1}{4}$	$\frac{3}{4},0,\frac{1}{4}$			hkl : $h=2n$
8	*c*	2/*m* . .	$0,\frac{1}{4},\frac{1}{4}$	$0,\frac{3}{4},\frac{1}{4}$			hkl : $h=2n$
4	*b*	*m m m*	$0,0,\frac{1}{2}$				no extra conditions
4	*a*	*m m m*	$0,0,0$				no extra conditions

Symmetry of special projections

Along [001] $p2mm$
$\mathbf{a}' = \frac{1}{2}\mathbf{a}$ $\mathbf{b}' = \frac{1}{2}\mathbf{b}$
Origin at $0,0,z$

Along [100] $p2mm$
$\mathbf{a}' = \frac{1}{2}\mathbf{b}$ $\mathbf{b}' = \frac{1}{2}\mathbf{c}$
Origin at $x,0,0$

Along [010] $p2mm$
$\mathbf{a}' = \frac{1}{2}\mathbf{c}$ $\mathbf{b}' = \frac{1}{2}\mathbf{a}$
Origin at $0,y,0$

International Tables for Crystallography (2006). Vol. A, Space group 64, pp. 302–303.

$Cmce$ D_{2h}^{18} mmm Orthorhombic

No. 64 $C\ 2/m\ 2/c\ 2_1/e$ Patterson symmetry $Cmmm$

Former space-group symbol $Cmca$; *cf.* Chapter 1.3

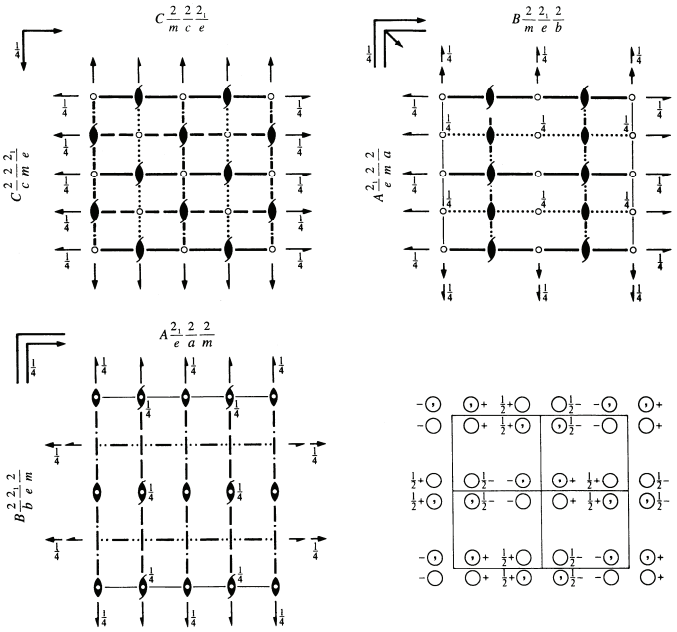

Origin at centre $(2/m)$ at $2/mn1$

Asymmetric unit $0 \le x \le \frac{1}{4}$; $0 \le y \le \frac{1}{2}$; $0 \le z \le \frac{1}{2}$

Symmetry operations

For $(0,0,0)+$ set

(1) 1	(2) $2(0,0,\frac{1}{2})$ $0,\frac{1}{4},z$	(3) $2(0,\frac{1}{2},0)$ $0,y,\frac{1}{4}$	(4) 2 $x,0,0$
(5) $\bar{1}$ $0,0,0$	(6) b $x,y,\frac{1}{4}$	(7) c $x,\frac{1}{4},z$	(8) m $0,y,z$

For $(\frac{1}{2},\frac{1}{2},0)+$ set

(1) $t(\frac{1}{2},\frac{1}{2},0)$	(2) $2(0,0,\frac{1}{2})$ $\frac{1}{4},0,z$	(3) 2 $\frac{1}{4},y,\frac{1}{4}$	(4) $2(\frac{1}{2},0,0)$ $x,\frac{1}{4},0$
(5) $\bar{1}$ $\frac{1}{4},\frac{1}{4},0$	(6) a $x,y,\frac{1}{4}$	(7) $n(\frac{1}{2},0,\frac{1}{2})$ $x,0,z$	(8) b $\frac{1}{4},y,z$

CONTINUED **No. 64** ***Cmce***

Generators selected (1); $t(1,0,0)$; $t(0,1,0)$; $t(0,0,1)$; $t(\frac{1}{2},\frac{1}{2},0)$; (2); (3); (5)

Positions

Multiplicity, Wyckoff letter, Site symmetry			Coordinates $(0,0,0)+$ $(\frac{1}{2},\frac{1}{2},0)+$				Reflection conditions
							General:
16	*g*	1	(1) x,y,z	(2) $\bar{x},\bar{y}+\frac{1}{2},z+\frac{1}{2}$	(3) $\bar{x},y+\frac{1}{2},\bar{z}+\frac{1}{2}$	(4) $x,\bar{y},\bar{z}$	hkl : $h+k=2n$
			(5) $\bar{x},\bar{y},\bar{z}$	(6) $x,y+\frac{1}{2},\bar{z}+\frac{1}{2}$	(7) $x,\bar{y}+\frac{1}{2},z+\frac{1}{2}$	(8) $\bar{x},y,z$	$0kl$: $k=2n$ $h0l$: $h,l=2n$ $hk0$: $h,k=2n$ $h00$: $h=2n$ $0k0$: $k=2n$ $00l$: $l=2n$
							Special: as above, plus
8	*f*	*m* . .	$0,y,z$	$0,\bar{y}+\frac{1}{2},z+\frac{1}{2}$	$0,y+\frac{1}{2},\bar{z}+\frac{1}{2}$	$0,\bar{y},\bar{z}$	no extra conditions
8	*e*	. 2 .	$\frac{1}{4},y,\frac{1}{4}$	$\frac{3}{4},\bar{y}+\frac{1}{2},\frac{3}{4}$	$\frac{3}{4},\bar{y},\frac{3}{4}$	$\frac{1}{4},y+\frac{1}{2},\frac{1}{4}$	hkl : $h=2n$
8	*d*	2 . .	$x,0,0$	$\bar{x},\frac{1}{2},\frac{1}{2}$	$\bar{x},0,0$	$x,\frac{1}{2},\frac{1}{2}$	hkl : $k+l=2n$
8	*c*	$\bar{1}$	$\frac{1}{4},\frac{1}{4},0$	$\frac{3}{4},\frac{1}{4},\frac{1}{2}$	$\frac{3}{4},\frac{3}{4},\frac{1}{2}$	$\frac{1}{4},\frac{3}{4},0$	hkl : $k,l=2n$
4	*b*	$2/m$ . .	$\frac{1}{2},0,0$	$\frac{1}{2},\frac{1}{2},\frac{1}{2}$			hkl : $k+l=2n$
4	*a*	$2/m$ . .	$0,0,0$	$0,\frac{1}{2},\frac{1}{2}$			hkl : $k+l=2n$

Symmetry of special projections

Along [001] $p2mm$
$\mathbf{a}' = \frac{1}{2}\mathbf{a}$ $\mathbf{b}' = \frac{1}{2}\mathbf{b}$
Origin at $0,0,z$

Along [100] $p2gm$
$\mathbf{a}' = \frac{1}{2}\mathbf{b}$ $\mathbf{b}' = \mathbf{c}$
Origin at $x,0,0$

Along [010] $p2mm$
$\mathbf{a}' = \frac{1}{2}\mathbf{c}$ $\mathbf{b}' = \frac{1}{2}\mathbf{a}$
Origin at $0,y,0$

Maximal non-isomorphic subgroups

I
[2] $C2ce$ ($Aea2$, 41) (1; 4; 6; 7)+
[2] $Cm2e$ ($Aem2$, 39) (1; 3; 6; 8)+
[2] $Cmc2_1$ (36) (1; 2; 7; 8)+
[2] $C222_1$ (20) (1; 2; 3; 4)+
[2] $C12/c1$ ($C2/c$, 15) (1; 3; 5; 7)+
[2] $C112_1/e$ ($P2_1/c$, 14) (1; 2; 5; 6)+
[2] $C2/m11$ ($C2/m$, 12) (1; 4; 5; 8)+

IIa
[2] $Pmnb$ ($Pnma$, 62) 1; 3; 6; 8; (2; 4; 5; 7) + $(\frac{1}{2},\frac{1}{2},0)$
[2] $Pbca$ (61) 1; 3; 5; 7; (2; 4; 6; 8) + $(\frac{1}{2},\frac{1}{2},0)$
[2] $Pbna$ ($Pbcn$, 60) 1; 2; 3; 4; (5; 6; 7; 8) + $(\frac{1}{2},\frac{1}{2},0)$
[2] $Pmca$ ($Pbcm$, 57) 1; 2; 7; 8; (3; 4; 5; 6) + $(\frac{1}{2},\frac{1}{2},0)$
[2] $Pbnb$ ($Pccn$, 56) 1; 2; 5; 6; (3; 4; 7; 8) + $(\frac{1}{2},\frac{1}{2},0)$
[2] $Pmcb$ ($Pbam$, 55) 1; 2; 3; 4; 5; 6; 7; 8
[2] $Pbcb$ ($Pcca$, 54) 1; 4; 6; 7; (2; 3; 5; 8) + $(\frac{1}{2},\frac{1}{2},0)$
[2] $Pmna$ (53) 1; 4; 5; 8; (2; 3; 6; 7) + $(\frac{1}{2},\frac{1}{2},0)$

IIb none

Maximal isomorphic subgroups of lowest index

IIc [3] $Cmce$ ($\mathbf{a}' = 3\mathbf{a}$) (64); [3] $Cmce$ ($\mathbf{b}' = 3\mathbf{b}$) (64); [3] $Cmce$ ($\mathbf{c}' = 3\mathbf{c}$) (64)

Minimal non-isomorphic supergroups

I none

II [2] $Fmmm$ (69); [2] $Pmcm$ ($\mathbf{a}' = \frac{1}{2}\mathbf{a}, \mathbf{b}' = \frac{1}{2}\mathbf{b}$) ($Pmma$, 51); [2] $Cmme$ ($\mathbf{c}' = \frac{1}{2}\mathbf{c}$) (67)

Contact

HEiDi

Phone: 089/289-14828
Web: http://www.frm2.tum.de/wissenschaftliche-nutzung/diffraktion/heidi/index.html

Martin Meven
Institut für Kristallographie Aachen, RWTH Aachen
JCNS Outstation at Forschungsneutronenquelle Heinz Maier-Leibnitz (FRM II)
Phone: 089/289-14727
e-Mail: Martin.Meven@frm2.tum.de

SPHERES

Backscattering spectrometer

J. Wuttke

Jülich Centre for Neutron Science
Forschungszentrum Jülich

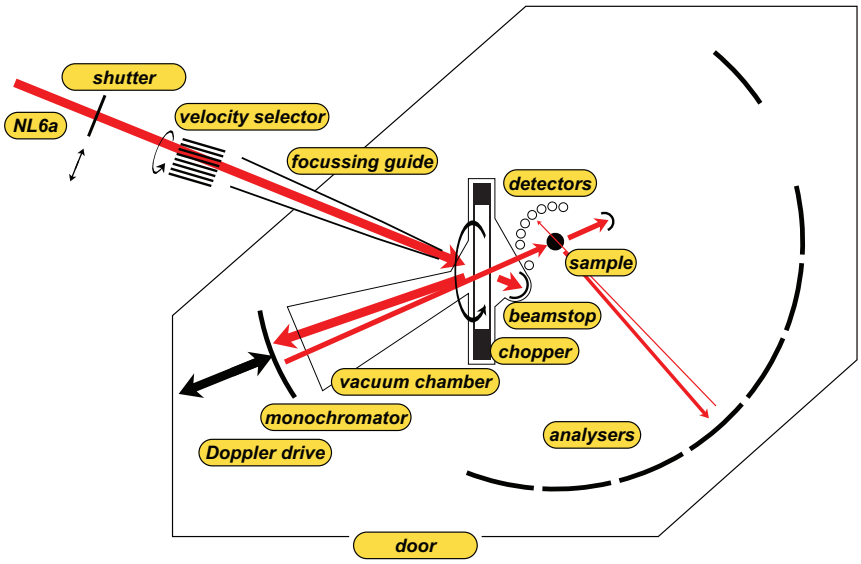

Manual of the JCNS Laboratory Course Neutron Scattering

Contents

1 Introduction

Neutron *backscattering spectrometers* are used to measure *inelastic scattering* with very high *energy resolution*. What does this mean?

In inelastic scattering, scattering intensity is measured as function of the energy exchanged between the scattered neutron and the sample. As in other areas of physics, a data set of the form intensity-versus-energy is called a *spectrum*. An instrument that resolves inelastic scattering is therefore called a *spectrometer*.

While elastic scattering experiments yield information about *structure* or *texture* of a sample, inelastic scattering is used to investigate its *dynamics*. Specifically, inelastic neutron scattering yields information about the thermal motion of atomic nuclei.

The most common instrument for inelastic neutron scattering is the triple-axis spectrometer. It is routinely used to measure phonon and magnon dispersions, with energy exchanges of the order of meV. In contrast, the *high resolution* of a backscattering spectrometer allows to resolve very *small energy shifts* of the order of μeV. By the time-energy uncertainty relation, small energy means long times. Hence, backscattering addresses relatively *slow* nuclear motion — much slower than the lattice vibrations typically seen in triple-axis spectrometry.

What processes take place on the energy or time scale made accessible by neutron backscattering? For instance the following:

- hyperfine splitting of nuclear spin orientations in a magnetic field,
- rotations or hindered reorientations of molecules or molecular side groups,
- quantum tunneling,
- hydrogen diffusion in solids,
- relaxation (molecular rearrangements) in viscous liquids,
- innermolecular rearrangements in polymers.

During your lab course day, you will use the backscattering spectrometer SPHERES (SPectrometer for High Energy RESolution) to study one example of these applications.

2 Spectrometer Physics

2.1 Energy Selection by Backscattering

In crystal spectrometers, neutron energies are selected by Bragg reflection from crystals, according to the *Bragg condition*

$$n\lambda_n = 2d_{hkl}\sin\Theta \tag{1}$$

where d_{hkl} is the distance of lattice planes $[hkl]$, and Θ is the glancing angle of reflection from these planes. The index n indicates that along with a fundamental wavelength λ_1, integer fractions $\lambda_n = \lambda_1/n$ are transmitted as well. To suppress these unwanted higher orders, experimental setups include either a mechanical neutron velocity selector (Fig. 1), or a beryllium filter.

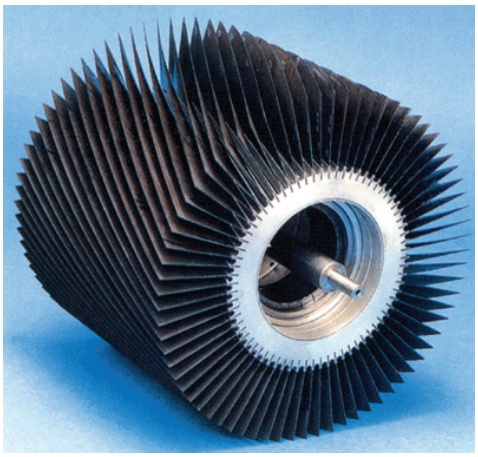

Fig. 1: *Rotor of a mechanical neutron velocity selector. The blades are coated with neutron absorbing material. In SPHERES, such a selector is used as a pre-monochromator that reduces the incoming white spectrum to about* $\pm 6\%$. *© Astrium GmbH.*

In practice, the parameters d and Θ on the right-hand side of Eq. (1) are not sharp: Imperfections of the crystal lead to a distribution of lattice constants, characterized by a width δd. And similarly, imperfections of the neutron optics (inevitable because the incoming beam, the sample, and the detector all have finite size) lead to a distribution of reflection angles, characterized by a width $\delta\Theta$. By differentiating the Bragg equation (1), one obtains the relative width of the wavelength distribution reflected by a crystal monochromator:

$$\frac{\delta\lambda}{\lambda} = \frac{\delta d}{d} + \cot\Theta\,\delta\Theta. \tag{2}$$

In usual crystal spectrometers, the second term is the dominant one. However, by choosing $\Theta = 90°$, the prefactor $\cot\Theta$ can be sent to zero. This is the fundamental idea of the backscattering spectrometer. If a monochromator crystal is used in backscattering geometry, with $\Theta \simeq 90°$, then the reflected wavelength distribution is in first order insensitive to the geometric imperfection $\delta\Theta$; it depends only on the crystal imperfection δd and on a second-order $(\delta\Theta)^2$ term.

The monochromator of SPHERES is made of silicon crystals in (111) orientation (Fig. 2). The backscattered wavelength is $\lambda = 2d_{111} = 6.27$ Å, corresponding to a neutron energy of 2.08 meV. The crystals are cut from wafers produced by the semiconductor industry. They are perfectly monocrystalline, so that their intrinsic resolution[1] of $\delta d/d \simeq 10^{-6}$ is actually too good because it does not match the spectrometer's second-order geometric imperfection $(\delta\Theta)^2 \lesssim 10^{-4}$. As a remedy, the crystals are glued to a spherical support so that the resulting strain induces a lattice constant gradient of the order $\delta d/d \simeq 10^{-4}$.

[1] In perfect crystals, the intrinsic resolution $\delta d/d$ is limited by *primary extinction*: Say, each crystalline layer has a reflectivity of about 10^{-6}. Then only about 10^6 layers contribute to the Bragg reflection. This limits $\delta\lambda/\lambda$ to about 10^{-6}.

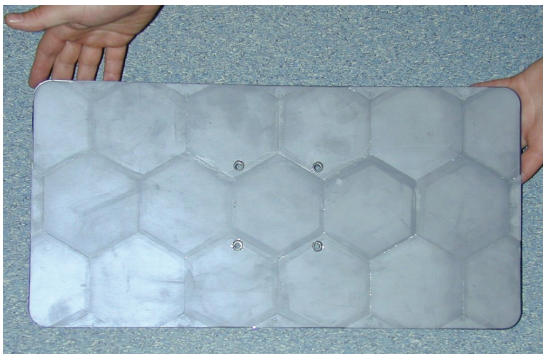

Fig. 2: *The monochromator of SPHERES consists of hexagonal Si(111) wafers of 750 µm thickness, glued onto a spherical support made of carbon fiber.*

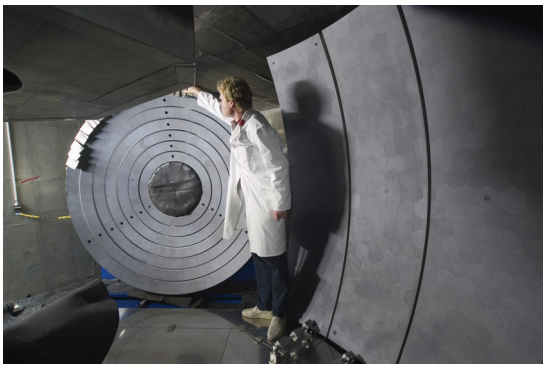

Fig. 3: *The analyzers of SPHERES are made of the same Si(111) as the monochromator. For small scattering angles, they are shaped as rings; for large scattering angles, they are approximately rectangular sections of a sphere.*

2.2 Spectrometer Layout

In a crystal spectrometer, a *monochromator* is used to send a neutron beam with a narrow energy distribution $E_\mathrm{i} \pm \delta E$ onto the sample. After the sample, a second monochromator, called *analyzer*, is used to select a narrow energy distribution $E_\mathrm{f} \pm \delta E$ out of the scattered spectrum. In SPHERES, we actually have a huge array of analyzers (Fig. 3), covering a solid angle of about 2.5, which is 20% of 4π. These analyzers send energy-selected neutrons towards 16 different detectors, depending on the scattering angle ϑ.

Fig. 4 shows the complete layout of SPHERES. The incoming beam is pre-monochromatized by a mechanical velocity selector. Then, it is transported by a focussing neutron guide into the instrument housing where it hits a rotating chopper. The chopper rotor (Fig. 5) carries mosaic crystals made of pyrolitic graphite on half of its circumference. When the incoming neutrons hit

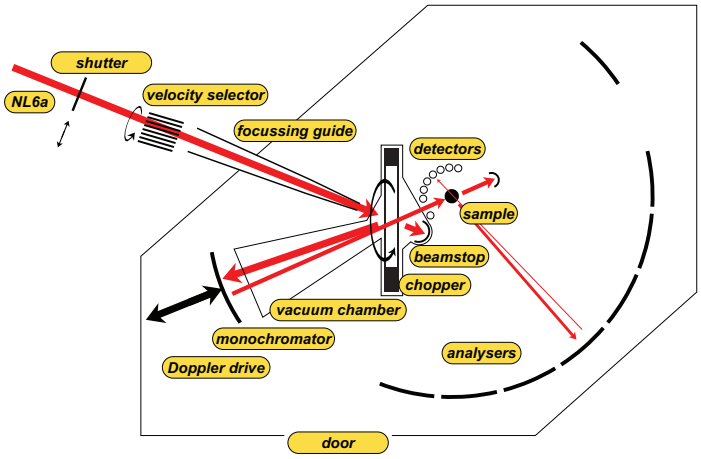

Fig. 4: *Layout of the Jülich backscattering spectrometer SPHERES at FRM II.*

Fig. 5: *Schematic front view of the chopper rotor of SPHERES. The red bands indicate the mosaic crystals that deflect the incident beam towards the monochromator.*

these crystals, they undergo a Bragg reflection towards the monochromator.[2] Otherwise, they are transmitted towards a beamstop.

The backscattering monochromator selects a neutron band $E_\mathrm{i} \pm \delta E$ as described above. Neutrons within this band are sent back towards the chopper. When they reach the chopper, the rotor has turned by $60°$: the mosic crystals have moved out of the way; the neutrons coming from the monochromator are transmitted towards the sample.

The sample scatters neutrons into 4π. About 20% of this is covered by analyzers. If a scattered neutron hits an analyzer and fullfills the backscattering Bragg condition, it is sent back towards the sample. It traverses the sample[3] and reaches a detector. To discriminate energy-selected neutrons from neutrons that are directly scattered from the sample into a detector, the time of arrival is put in relation to the chopper phase.

[2] As a side effect, the Bragg deflection by rotating mosaic crystals achieves a favorable *phase-space transform* (PST): the incoming wavevector distribution is spread in angle, but compressed in modulus. This results in a higher spectral flux in the acceptance range of the monochromator.

[3] Of course not all neutrons are transmitted: some are lost, some are scattered into a wrong detector. This inaccuracy is inevitable in neutron backscattering. We strive to keep it small by using rather thin samples with typical transmissions of 90% to 95%.

While the primary spectrometer (everything before the sample) is mainly in vacuum, the secondary spectrometer is not. To minimize neutron losses in the secondary spectrometer, the entire instrument housing can be flooded with argon. For the labcourse, we preferentially remove the argon so that participants can accede the housing. However, since refilling takes at least one full day, time constraints may prevent us from doing so. In this case, a video will be shown to present the interior of the spectrometer.

2.3 Measuring Spectra

So far we have introduced a static arrangement with fixed energies $E_\mathrm{i} = E_\mathrm{f}$. Such an arrangement is actually used to measure the fraction of elastic versus total scattering, called the *Debye-Waller factor* for coherent scattering and the *Lamb-Mössbauer factor* for incoherent scattering. More often, however, one wants to measure full spectra $S(Q, \omega)$. Therefore, one must find a way to modify the energy transfer

$$\hbar\omega = E_\mathrm{i} - E_\mathrm{f}. \tag{3}$$

This can be done using the *Doppler effect*: The monochromator is mounted on a linear drive that performs a cyclic motion. In the monochromator's rest frame, the backscattered energy is always the value $E_0 = 2.08$ meV given by the lattice constant of Si(111). Depending on the monochromator's velocity v, the value in the laboratory frame is

$$E_\mathrm{i}(v) = \frac{m_\mathrm{n}}{2}\,(v_0 + v)^2 \tag{4}$$

where $v_0 = 631$ m/s is the neutron velocity at $E_0 = m_\mathrm{n}/2\,v_0^2$. The Doppler drive of SPHERES has a linear amplitude of ± 75 mm and achieves a velocity amplitude of ± 4.7 m/s, resulting in an energy range

$$-30.7\ \mu\mathrm{eV} < \hbar\omega < 30.9\ \mu\mathrm{eV}. \tag{5}$$

This is called the *dynamic range* of the spectrometer.

When a scattered neutron is detected, its time of flight is traced back to the moment when it has been backscattered by the monochromator. From the recorded trace of the linear drive, the monochromator velocity at that moment is infered, ω is computed from (4) and (3), and the corresponding histogram channel is incremented. To determine $S(Q, \omega)$, one needs to normalize to the time spent in channel ω. This normalization is routinely done by the instrument's raw-data reduction program SLAW.

2.4 Instrument Characteristics

The performance of a spectrometer can be characterized by its *resolution function*. To obtain the resolution function, one measures the spectrum of a purely elastic scatterer. Fig. 6 shows the result of a resolution measurement from a user experiment on SPHERES. Note the logarithmic intensity scale.

Conventionally, the resolution of an instrument is characterized by the *full width at half maximum* (FWHM). For SPHERES, a typical value is 0.65 μeV. Note however that the FWHM is

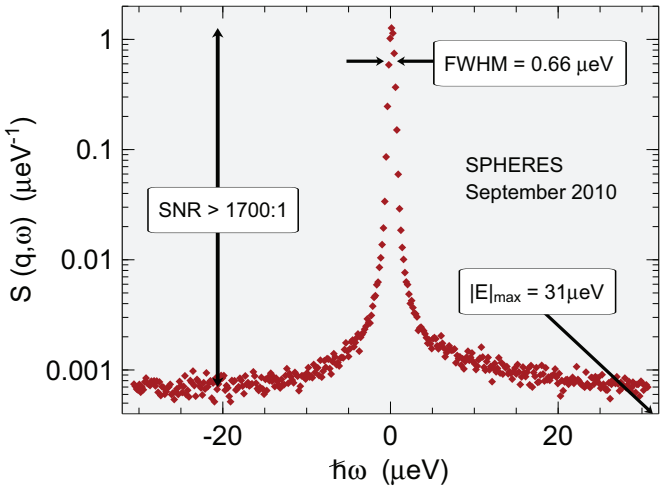

Fig. 6: *Resolution function of SPHERES, measured on a user provided sample at a low temperature where the scattering is purely elastic.*

not the full story: the quality of an instrument also depends on the *shape* of the resolution functions, especially of the deep wings. The resolution of SPHERES is slightly asymmetric. This is related to the $(\delta\Theta)^2$ term in the wavelength spread of a backscattering analyzer: all deviations from the perfect $\Theta = 90°$ geometry lead to the transmission of longer wavelengths, never of shorter ones.

Another important figure of merit is the *signal-to-noise ratio* (SNR). It depends strongly on the ratio of scattering to absorption cross sections and on the thickness and geometry of the sample. With argon filling, the best value obtained in user experiments has been 1700:1; without argon, 1200:1. On the other hand, for strongly absorbing samples it is sometimes less than 100:1.

3 Applications

In the following, two different applications of neutron backscattering are explained: hyperfine splitting in a magnetic material, and methyl group tunneling.

3.1 Hyperfine Splitting

The measurement of hyperfine splitting has been historically the first application of neutron backscattering,[4] and to this day, it is the conceptually simplest one.

Since the neutron has spin $S = 1/2$, its magnetic quantum number can take the values $S_z = \pm 1/2$. In a scattering event, this quantum number can change. In more pictorial words: when a

[4] A. Heidemann, Z. Phys. 238, 208 (1970).

neutron is scattered, it may or may not undergo a *spin flip*.

As angular momentum is conserved, a change of S_z must be accompanied by an opposite change of the magnetic quantum number I_z of the nucleus by which the neutron is scattered, $\Delta I_z = -\Delta S_z$. Therefore, spin-flip scattering is only possible if the sample contains nuclei with nonzero spin I.

Nuclei with nonzero spin quantum number I possess a magnetic moment

$$\mu = Ig\mu_{\mathrm{N}} \tag{6}$$

with the nuclear magneton

$$\mu_{\mathrm{N}} = \frac{e\hbar}{2m_{\mathrm{p}}} = 3.153 \cdot 10^{-8}\ \mathrm{eV/T}. \tag{7}$$

The g factor is different for each nucleus.[5]

A local magnetic field B leads to a splitting of energy levels,

$$E = I_z g\mu_{\mathrm{N}} B, \tag{8}$$

called *hyperfine splitting*. Consequently spin-flip scattering is accompanied by an energy exchange $\Delta E = \pm g\mu_{\mathrm{N}} B$. By measuring the neutron energy gain or loss $\pm\Delta E$, one can accurately determine the local field B in ferromagnetic or antiferromagnetic materials.

3.2 Molecular Rotation and Quantum Tunneling

Rotational motion of molecules or molecular side groups is one of the most important applications of neutron backscattering. Here, we specialize on the rotation of methyl (CH_3) groups. We consider these groups as stiff, with fixed[6] CH bond length 1.097 Å and HCH angle 106.5.°

The only degree of freedom is then a rotation around the RC bond that connects the methyl group to the remainder R of the molecule. This RC bond coincides with the symmetry axis of the CH_3 group. The rotational motion can therefore be described by a wave function ψ that depends on one single coordinate, the rotation angle ϕ.

The Schrdinger equation is

$$\left\{ B\frac{\partial^2}{\partial\phi^2} - V(\phi) + E \right\} \psi(\phi) = 0. \tag{9}$$

For free rotation ($V = 0$), solutions that possess the requested periodicity are sine and cosine functions of argument $J\phi$, with integer J. Accordingly, the energy levels are $E = BJ^2$.

Given the value $B = 670$ μeV, it is obvious that free rotor excitations occur only far outside the dynamic range of neutron backscattering. Conversely, if we observe an inelastic signal from methyl groups on a backscattering spectrometer, then we must conclude that $V \neq 0$: the

[5] Tabulation: http://ie.lbl.gov/toipdf/mometbl.pdf.

[6] Ignoring the variations of empirical values, which are of the order of ± 0.004 Å and $\pm 1.5°$.

methyl group rotation is *hindered* by a rotational potential. This potential can be caused by the remainder R of the molecule as well as by neighbouring molecules.

Due to the symmetry of the CH_3 group, the Fourier expansion of $V(\phi)$ contains only sine and cosine functions with argument $3m\phi$, with integer m. In most applications, it is sufficient to retain only one term,

$$V(\phi) \doteq V_3 \cos(3\phi). \tag{10}$$

The strength of the potential can then be expressed by the dimensionless number V_3/B. In the following we specialize to the case of a *strong potential*, $V_3/B \gg 10$, which is by far the most frequent one.

In a strong potential of form (10), the CH_3 group has three preferential orientations, separated by potential walls. The motion of the CH_3 group consists mainly of small excursions from the preferred orientations, called *librations*. Essentially, they are harmonic vibrations.

At low temperatures, almost exclusively the vibrational ground state is occupied. Yet reorientational motion beyond librations is possible by means of quantum mechanical tunneling: the wave functions of the three localised *pocket states* ψ_m ($m = 1, 2, 3$) have nonzero overlap. Therefore, the ground state is a linear combination of pocket states.[7] Periodicity and threefold symmetry allow three such combinations: a plain additive one

$$\psi_1 + \psi_2 + \psi_3, \tag{11}$$

and two superpositions with phase rotations

$$\psi_1 + \mathrm{e}^{\pm i2\pi/3}\psi_2 + \mathrm{e}^{\pm i4\pi/3}\psi_3. \tag{12}$$

In the language of group theory, state (11) has symmetry A, the degenerate states (12) are labelled E^a, E^b. It is found that A is the ground state. The *tunneling splitting* $\hbar\omega_\mathrm{t}$ between the states A and E is determined by the overlap integral $\langle\psi_m|V|\psi_n\rangle$ ($m \neq n$). It depends exponentially on the height of the potential wall. Provided it falls into the dynamic range of neutron scattering, it leads to a pair of inelastic lines at at $\pm\hbar\omega_\mathrm{t}$.

With rising temperatures, the occupancy of excited vibrational levels increase. This facilitates transitions between A and E sublevels and results in a decrease of $\hbar\omega_\mathrm{t}$ and a broadening of the inelastic lines.

Upon further temperature increase, thermal motion of neighbouring molecules causes so strong potential fluctuations that the picture of quantum tunneling is no longer applicable. Instead, the motion between different pocket states can be described as *stochastic jump diffusion*.

Let $p_m(t)$ be the probability of being in pocket state m ($m = 1, 2, 3$). Assume that jumps between the three main orientations occur with a constant rate τ^{-1}. Then, the p_m obye rate equations

$$\frac{\mathrm{d}}{\mathrm{d}t}p_m(t) = \frac{1}{\tau}\left\{-p_m + \sum_{n\neq m}\frac{1}{2}p_n\right\}. \tag{13}$$

[7] This is an extremely simplified outline of the theory. In a serious treatment, to get all symmetry requirements right, one must also take into account the nuclear spins of the H atoms. See W. Press, Single-Particle Rotations in Molecular Crystals, Springer: Berlin 1981.

The stationary equilibrium solution is just $p_m = 1/3$ for all m. When perturbed, the system relaxes into equilibrium with a time dependence of $\exp(-t/\tilde{\tau})$. Explicit solution of the linear differential equation system (13) yields $\tilde{\tau} = 2\tau/3$.

According to a fundamental theorem of statistical mechanics (the *fluctation dissipation theorem*), the relaxation by which a slightly perturbed system returns *into* equilibrium has the same time dependence as the pair correlation function *in* equilibrium. Therefore, we can employ the solution of (13) to write down the self-correlation function of the protons that constitute our methyl group. Fourier transform yields then the incoherent scattering function

$$S(q,\omega) = a(q)\delta(\omega) + b(q)\frac{\Gamma}{\omega^2 + \Gamma^2}. \tag{14}$$

The first term describes elastic scattering. The second term, the Fourier transform of the exponential $\exp(-t/\tilde{\tau})$, is a Lorentzian with linewidth $\Gamma = \tilde{\tau}^{-1}$; such *broadening* of the elastic line is often called *quasielastic*.

4 Preparatory Exercises

1. Relate the relative wavelength spread $\delta\lambda/\lambda$ to the relative energy spread $\delta E/E$.
2. In SPHERES, useable detectors are located at scattering angles 2θ ranging from 12.5° to 134°. Calculate the corresponding wavenumbers in Å^{-1}. Recommendation: use the following constants in *atomic units*: $\hbar c = 1973$ eVÅ and $m_n c^2 = 940$ MeV.
3. Convert dynamic range and resolution of SPHERES into GHz. To make contact with optical spectroscopy, you might also wish to convert into cm^{-1}.
4. Empirically, it is found that the centre of the resolution function can be fitted by a Gaussian $a\exp(-E^2/2/\sigma^2)$. Derive an expression that relates the Gaussian standard deviation σ to the FWHM.
5. Note that the above mentioned fit applies only to the very centre of the resolution function. How does a Gaussian look like on the lin-log representation of Fig. 6? And a Lorentzian?
6. In SPHERES, the distance sample-analyzer is 2 m. Calculate the time neutrons need for a round trip sample-analyzer-sample, and deduce the rotation frequency of the chopper.
7. Assume that the monochromator motion is perfectly sinusoidal. Sketch how the measuring time per energy channel varies with $\hbar\omega$.
8. Draw a sketch of the expected backscattering spectrum $S(q,\omega)$ of a ferromagnetic material with $I \neq 0$.
9. Assume a hyperfine splitting of $\Delta E = 2$ μeV. To which temperature do you have to cool the sample to observe a 10% difference between the probabilities of energy gain and energy loss scattering?
10. How do you expect ΔE to evolve when the sample is heated towards the Curie or Néel temperature?

11. Calculate the moment of inertia, $I = \sum mr_\perp^2$, of a methyl group. Verify that the *rotational constant* $B = \hbar^2/(2I)$ has a value of about 670 μeV.

12. Expand $V(\phi)$ around a potential minimum, and compare the resulting Schrödinger equation with that of a harmonic oscillator. Show that the splitting of oscillator levels is of the order of meV.

13. Draw a coordinate system energy-versus-angle. Sketch $V(\phi)$, the harmonic approximation, the ground state's $\psi(\phi)$, and the lowest oscillator energy levels. What does that imply for the validity of the oscillator approximation?

14. Sketch the expected spectra for different temperatures.

5 Experiment Procedure

5.1 The experiment itself

After an initial discussion, the group chooses which experiment to perform: hyperfine splitting, methyl group tunneling, or participation in an ongoing research project. For a given chemical composition, the group computes the sample thickness that yields 90% transmission. Depending on the group's interest, a sample is prepared, or a standard sample is used. The tutor shows how to insert the sample in the instrument's cryostat. Using the instrument's graphical user interface, starting a measurement is rather trivial. Log entries are written to the instrument log wiki.

5.2 Raw data reduction

The program SLAW is used to convert raw neutron counts into $S(Q, \omega)$. It is parametrized by a script, called `Slawfile`. The tutor provides a sample script, which is then modified to convert the results of the current experiment.

SLAW can save $S(Q, \omega)$ in a variety of output formats. Most relevant are plain tabular formats `recttab` and `spectab`, and a self-documenting format `y08` required by our standard data-analysis software FRIDA.

5.3 Data evaluation

In a first approach, labcourse participants should analyse plain tabular data using whatever all-purpose data-analysis software they are used to.

1. Plot a representative selection (choose a few Q) of measured spectra.

2. Determine the FWHM of the elastic line, and of the inelastic lines if there are any.

3. Try to fit these lines with a Gaussian, with a Lorentzian, with a squared Lorentzian.

4. Summarize the temperature dependence of the spectra.

For a more quantitative analysis, it is necessary to convolute a theoretical model with a measured resolution function. This can be done with the data-analysis package FRIDA. For a tutorial, refer to the SPHERES wiki.[8]

[8] Follow the link at `http://www.jcns.info/jcns_spheres`.

Contact

SPHERES

Phone: 089/289-14875
Web: http://www.jcns.info/jcns_spheres/

Michaela Zamponi

JCNS at FRM II, Forschungszentrum Jülich GmbH

Phone: 089/289-10793
e-Mail: m.zamponi@fz-juelich.de

Gerald J. Schneider

Phone: 089/289-10718
e-Mail: g.j.schneider@fz-juelich.de

DNS

Neutron Polarization Analysis

Y. Su

Jülich Centre for Neutron Science
Forschungszentrum Jülich

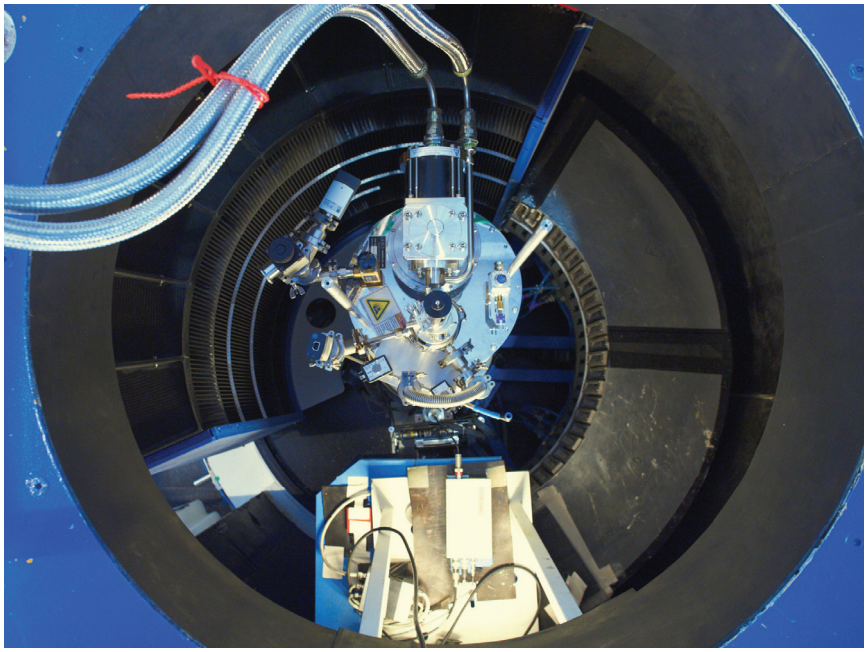

Manual of the JCNS Laboratory Course Neutron Scattering

Contents

1 Introduction

Polarized neutron scattering and polarization analysis represents a powerful technique for the studies of complex ordering phenomena and dynamics of condensed matters. The elements of this technique and its advanced applications in particular in magnetism have been comprehensively covered in a number of recent lecture notes [1-4] and several seminal papers [5-7]. The aim of this exercise on *Neutron Polarization Analysis* is to provide you with some hands-on experience on the practical aspects of polarized neutron scattering based on the multi-detector time-of-flight spectrometer DNS at FRM II. The details on the handling of polarized neutrons and the fundamentals of polarization analysis will be demonstrated from a range of carefully designed experiments and exercises.

In Section 2 of this manual, an overview of the instrument DNS as well as its unique capabilities will be given. Section 3 consists of necessary preparatory exercises and questions which can be studied before the experiment. Section 4 describes the details of the experiment procedure and provides the experiment-related exercises.

2 Overview of the DNS instrument

DNS is a versatile diffuse scattering cold neutron time-of-flight spectrometer with polarization analysis at the neutron guide NL6a, FRM II. DNS has the capability to allow unambiguous separations of nuclear coherent, spin incoherent and magnetic scattering contributions simultaneously over a large range of scattering vector **Q** and energy transfer E. A schematic layout of DNS is shown in Fig. 1.

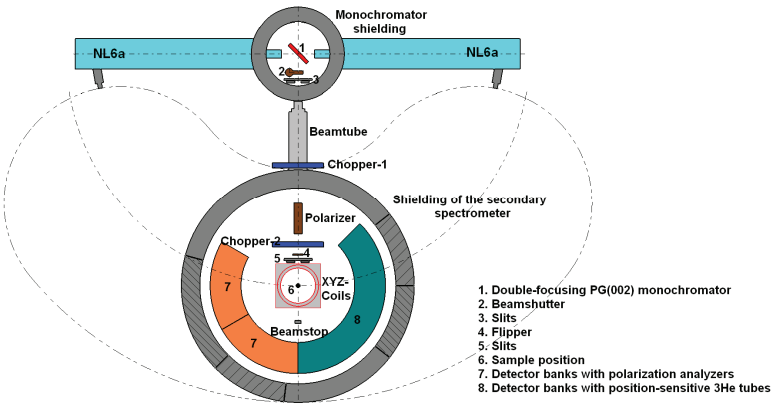

Fig. 1 The schematic layout of DNS

DNS has a number of unique features such as wide-angle polarization analysis, a large position-sensitive detector array and a high frequency double disc chopper system. With its compact design and the powerful double-focusing PG(002) monochromator, DNS is optimized as a high intensity instrument with medium resolution. The monochromatic neutron beams with the wavelength ranging from 2.4 to 6 Å are available at DNS. Newly constructed polarizer and polarization analyzers, both using m = 3 Schärpf bender-type focusing supermirrors, perform very well. A polarized neutron flux as high as 5×10^6 n/(s·cm^2) has been achieved at 4.74 Å. The polarization rate of the incident neutron beams is nearly 96%. The wide-angle polarization analysis in the horizontal scattering plane is achieved via using 24 units of polarization analyzers simultaneously. The neutron spins are manipulated using a Mezei-type π-flipper, followed by a set of orthogonal XYZ-coils situated around the sample position for providing guide fields. In addition to high polarized flux, the unique strength of DNS lies on its extreme versatility. DNS can be operated in a number of modes for a wide range of samples. There are three polarization analysis (PA) modes at DNS: uniaxial-PA for separation of coherent and spin-incoherent scattering in non-magnetic samples; longitudinal-PA for separation of magnetic scattering in paramagnetic and antiferromagnetic samples; vector-PA for the determination of complex magnetic structures.

Time-of-flight spectroscopy is another important application at DNS. The installation of 128 position-sensitive ^{3}He tubes of 1m height and half inch diameter has just been completed at DNS, and the commissioning is expected soon. This will increase the covered solid angle up to 1.9 sr. DNS will be running with a double disc chopper system with the frequency up to 300 Hz. The setup with two phase-controlled choppers would allow to eliminate high-order (e.g. λ/2) background or to select only high orders. DNS is targeted as a high count-rate cold neutron time-of-flight spectrometer with medium resolution. DNS is thus ideal for the studies of spin dynamics in many novel magnetic materials. The technical details of DNS are shown in Table 1.

Monochromator	horizontal- and vertically adjustable double-focusing	PG(002), d = 3.355 Å (at NL6a)
	crystal dimensions	2.5 × 2.5 cm^2 (5 × 7 crystals)
	wavelengths	2.4 Å ≤ λ ≤ 6 Å
Double-chopper system	chopper frequency	≤ 300 Hz
	repetition rate	≤ 900 Hz
	chopper disks	Titanium, 3 slits, ϕ = 420 mm
Expected flux at sample (n/cm^{2}s)	Non-polarized	~ 10^8
	Polarized (polarizer: m = 3 supermirror benders)	~ 5×10^6–10^7
Detector banks for non-polarized neutrons	position sensitive ^{3}He detector tubes	128 units, ϕ = 1.27 cm, height ~100 cm
	total solid angle covered	1.9 sr
	covered scattering angles in the horizontal plane	0° < 2θ ≤ 135°
Detector banks for polarized neutrons	polarization analyzers	24 units, m = 3 supermirror
	^{3}He detector tubes	24 units, ϕ = 2.54 cm, height 15 cm
	covered scattering angles in the horizontal plane	0° < 2θ ≤ 150°
Q_{max}	λ_i = 2.4 Å (E_i = 14.2 meV)	4.84 Å^{-1}
	λ_i = 6 Å (E_i = 2.28 meV)	1.93 Å^{-1}
Expected energy resolution	λ_i = 2.4 Å (E_i = 14.2 meV)	~ 1 meV
	λ_i = 6 Å (E_i = 2.28 meV)	~ 0.1 meV
Suitable samples	single crystals, powders, soft matters (e.g. polymer, liquid etc.)	
Sample environments	top-loading CCR, closed-cycle cold head, orange cryostat, cryo-furnace, ^{3}He/^{4}He dilution cryostat (~20mK), cryomagnet (self-shielding, vertical field up to 5T)	

Table 1 The technical details of the DNS instrument

Typical scientific applications at DNS are the studies of complex magnetic correlations, such as in highly frustrated magnets and strongly correlated electrons, as well as the structures of soft condensed matter systems, such as the nanoscale confined polymers and proteins, via polarization analysis. The exploration of unusual magnetic properties can also be efficiently undertaken on single-crystal samples by reciprocal space mapping. Fig. 2(a) shows an example of the measured magnetic diffuse scattering patterns in frustrated spin-ice pyrochlore compound $(Ho_{1-x}Y_x)_2Ti_2O_7$, due to in-plane magnetic correlations as determined by the spin-flip scattering of the initial P_z polarization [8]. In addition to the separation of magnetic cross section from nuclear and spin-incoherent ones, polarization analysis can also be used to explore possible anisotropy of spin correlations in complex materials. Polarized powder diffraction carried out at DNS is complementary to standard neutron powder diffraction and may be extremely useful for magnetic structure refinements, particularly in case of small magnetic moments by improving the signal to background ratio. Fig. 2(b) shows the magnetic and nuclear scattering of iron-based superconductor Sr_2CrO_3FeAs measured at DNS via polarization analysis and the corresponding Rietveld refinements [9]. Fig. 2(c) shows the magnetic diffuse scattering derived with the same approach on the $\{Mo_{72}Fe_{30}\}$ molecule magnet [10]. DNS also represents a powerful instrument for the soft condensed matter

community for the separation of nuclear coherent scattering from often dominating spin incoherent scattering background in hydrogenous materials.

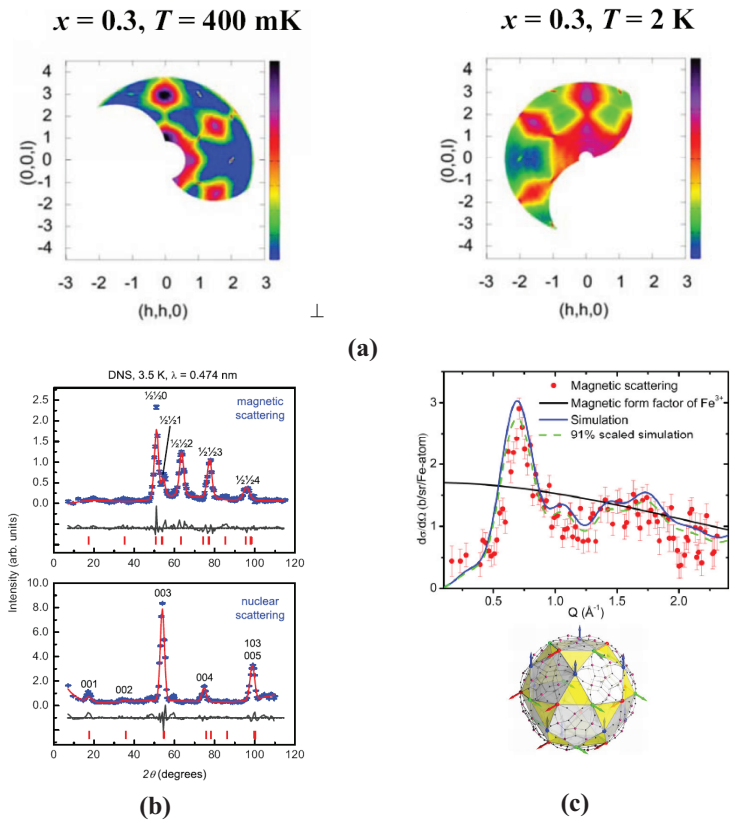

Fig. 2 Examples of the scientific applications at DNS: (a) peculiar magnetic diffuse scattering patterns observed on the frustrated spin-ice pyrochlore compound $(Ho_{1-x}Y_x)_2Ti_2O_7$ via polarization analysis [8]; (b) magnetic and nuclear scattering of iron-based superconductor Sr_2CrO_3FeAs at 3.5 K as measured (blue) at DNS via polarization analysis and the Rietveld refinements (red) [9]; (c) differential magnetic scattering cross section measured at 1.5 K and the theoretical simulation with the three-sublattice spin model of the $\{Mo_{72}Fe_{30}\}$ molecule magnet [10].

3 Preparatory Exercises

The practical aspects and the experimental setup of DNS with respect to polarization analysis have been addressed and discussed in great details in the lecture [1]. Therefore, it is strongly recommended to go through the relevant sections of the lecture notes thoroughly before the exercises. Try to answer the following general questions would greatly improve your understandings:

1. What is the Larmor precession? How to calculate the Larmor frequency (ω_L)?
2. How neutron spins would respond to changing magnetic fields? What are adiabatic and non-adiabatic behaviour?
3. How to produce polarized neutrons and how to analyze the spin state of the neutrons after the scattering process?
4. What is the spin flipper? How does it work?
5. What is the flipping ratio? What is the polarization rate of the neutron beams?
6. What are nuclear coherent, spin incoherent, isotopic incoherent and magnetic scattering processes? Whether and how the spin states of the scattered neutrons would be changed in those scattering processes?

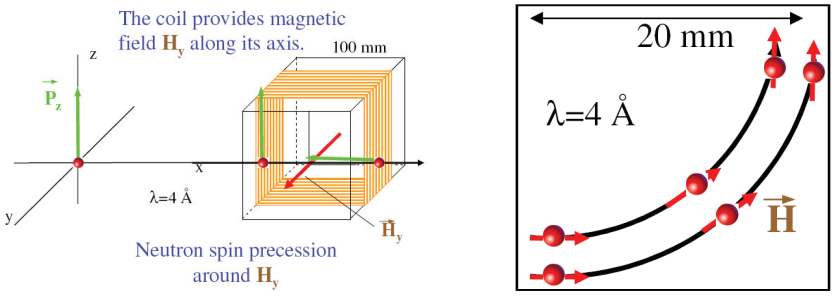

Fig. 3 Preparatory exercises

In addition to these general questions, the following exercises are provided:

1. How strong the magnetic fields $\mathbf{H}_y$ should be provided in the coil of length L = 100 mm to perform 90° turn for neutrons with λ=4 Å? (see Fig. 3(a))
2. A magnetic field **H** changes its space direction by 90° over a distance of L = 20 mm (as shown in Fig. 3(b)). How strong **H** should be to provide adiabatic evolution of the neutron spins guided by such fields? The neutrons wavelength is λ=4 Å.

4 Experiment Procedure and Experiment-related Exercises

4.1 Manipulating neutron spins

After the DNS instrument and its major instrument components are briefly introduced by the tutor, the first task for students is to learn how to manipulate neutrons spins via the Larmor precession and properly set guide fields. The following experiments are planned:

- Alignment of the π-flipper and z-compensation field coils for the incident neutrons with λ=4.74 Å
- Alignment of the magnetic guide fields at the sample position along three orthogonal directions via XYZ-coils
- Measurement of the flipping ratio and the polarization rate of the incident neutron beams at DNS

In addition, the following exercises are provided:

1. For neutrons with a wavelength λ=4.74 Å and a flight path of 10 mm through the flipper coil, how strong the flipping field would be required to achieve a π-flip?
2. The measured flipping ratio (R) is 25, what is the polarization rate (P) of the incident neutron beams?

4.2 Demonstration of the principle of neutron polarization analysis

The principle of neutron polarization analysis will be demonstrated here by the measurement of various standard samples. The following samples are planned,

- (002) Bragg reflection of pyrolytic graphite: nuclear coherent scattering
- Vanadium hollow-cylinder: nuclear spin-incoherent scattering
- Non-magnetic alloy $Ni_{0.89}Cr_{0.11}$: isotopic incoherent scattering
- A prototypical antiferromagnet: magnetic scattering

The students are expected to perform the experiment to measure the spin-flip and non-spin-flip scattering intensities of each sample via wide-angle polarization analyzers at DNS. The basic rules for the separation of different scattering cross-sections can thus be derived. The students will be encouraged to compare the results obtained at DNS to those reported in the seminal work by R.M. Moon [5].

The polarization efficiency can never achieve 100% due to polarization losses by depolarizations in the polarizer, the analyzer and the guide fields and the imperfections of the polarizer, the analyzer and the flipper. This would always lead to a finite flipping ratio even for an ideal non-spin-flip scatter. The correction for finite flipping ratio thus becomes an

important and always necessary practical issue in order to obtain a precise separation. Therefore, the following exercise related to the flipping ratio correction is provided,

1. The measured flipping ratio from an ideal isotopic incoherent scatter $Ni_{0.89}Cr_{0.11}$ is 20, the spin-flip scattering intensity is $I_{\uparrow\uparrow}$ and the non-spin-flip scattering intensity is $I_{\uparrow\downarrow}$, how to calculated the corrected intensities for $I_{\uparrow\uparrow}$ and $I_{\uparrow\downarrow}$ by taking into account the finite flipping ratio?

4.3 Case studies

In the final part, two case studies will be provided for students to maser neutron polarization analysis via the measurements on two real samples. The first one is the separation of nuclear coherent scattering from incoherent scattering in heavy water D_2O [11]. The second case study is the measurement of magnetic ordering in the novel superconducting compound via the XYZ-method [9]. The following exercises are provided,

1. How to separate nuclear coherent scattering from spin-incoherent scattering in soft condensed matter?
2. How to obtain the magnetic scattering cross section via the XYZ-method? Which necessary corrections need to be done for a precise separation?

References

[1] W. Schweika, *Polarized Neutron Scattering and Polarization Analysis,* in *Lecture Notes on Laboratory Course Neutron Scattering,* Eds. Th. Brückel, G. Heger, D. Richter, G. Roth and R. Zorn (Forschungszentrum Jülich, 2010)

[2] J. Schweiza, *Polarized Neutron and Polarization Analysis*, in *Neutron Scattering from Magnetic Materials*, Ed. T. Chatterji (Elsevier, Amsterdam, 2006)

[3] P.J. Brown, *Spherical Neutron Polarimetry*, in *Neutron Scattering from Magnetic Materials*, Ed. T. Chatterji (Elsevier, Amsterdam, 2006)

[4] L.P. Regnault, *Inelastic Neutron Polarization Analysis*, in *Neutron Scattering from Magnetic Materials*, Ed. T. Chatterji (Elsevier, Amsterdam, 2006)

[5] R.M. Moon, T. Riste, W.C. Koehler, Phys. Rev. **181**, 920 (1969)

[6] O. Schärpf, H. Capellmann, Phys. Stat. Sol. (a) **135**, 359 (1993)

[7] J.R. Stewart *et al.*, J. Appl. Cryst. **42**, 69 (2009)

[8] L.J. Chang *et al.*, Phys. Rev. B **82**, 172403 (2010)

[9] M. Tegel *et al.*, EPL **89**, 37006 (2010)

[10] Z.D. Fu *et al.*, New Journal of Physics **12**, 083044 (2010)

[11] L. Temleitner *et al.*, J. Phys.: Condens. Matter **19**, 335207 (2007)

Contact

DNS

Phone: 089/289-14339
Web: http://www.frm2.tum.de/wissenschaftliche-nutzung/spektrometrie/dns/index.html

Yixi Su

Juelich Centre for Neutron Science JCNS-FRM II
Forschungszentrum Juelich GmbH
Outstation at FRM II

Phone: 089/289-10714
e-Mail: Y.Su@fz-juelich.de
Web: http://www.fz-juelich.de/SharedDocs/Personen/JCNS/EN/Su_Y

J-NSE

Neutron spin echo spectrometer

O. Holderer, M. Zamponi and M. Monkenbusch

Jülich Centre for Neutron Science
Forschungszentrum Jülich

Manual of the JCNS Laboratory Course Neutron Scattering

Contents

1 Introduction

Aim of the experiment is to study the dynamics of a polymer chain in solution with Neutron Spin Echo spectroscopy (NSE), the technique which offers the highest energy resolution in neutron scattering. The technique is well suited for soft matter systems where the molecules or nanoscopic structures like membranes or micelles exhibit fluctuating Brownian motions, driven by the thermal energy. NSE is able to analyze these fluctuations on the nanosecond and nanometer time- and lengthscale.

In this neutron course experiment PEP (poly(ethylene propylene)) with a molecular weight of 70 kg/mol is dissolved in deuterated decane with a concentration of 3 %. The dynamics of the polymer in solution will be studied here at room temperature. The results will be interpreted in terms of the Zimm model which allows to draw conclusions about the internal motions of the polymer chains.

2 Neutron Spin Echo Spectroscopy

The neutron spin echo technique uses the neutron spin as an indicator of the individual velocity change the neutron suffered when scattered by the sample. Due to this trick the instrument accepts a broad wavelength band and at the same time is sensitive to velocity changes down to 10^{-5}. However the information carried by the spins can only be retrieved modulo an integer number of spin precessions as intensity modulation proportional to the cosine of a precession angle difference. The measured signal is the cosine transform $I(Q,t)$ of the scattering function $S(Q,\omega)$. All spin manipulations only serve to establish this special type of velocity analysis. For details see Reference [1].

Due to the intrinsic Fourier transform property of the NSE instrument it is especially suited for the investigation of relaxation-type motions that contribute at least several percent to the entire scattering intensity at the momentum transfer of interest. In those cases the Fourier transform property yields the desired relaxation function directly without numerical transformation and tedious resolution deconvolution. The resolution of the NSE may be corrected by a simple division.

For a given wavelength the Fourier time range is limited to short times (about 3 ps for the FRM II-setup) by the lower limit of the field integral and to long times by the maximum achievable field integral $J = \int Bdl$. The lower limit results from the lowest field values that are needed as "guide" field in order to prevent neutrons from depolarization effects. The upper limit results either from the maximum field that can be produced by the main solenoid, powersupply and cooling combination or by the maximum field integral inhomogeniety ($\rightarrow$ variation of precession angle between different paths within the neutron beam) that can be tolerated respectively corrected for, depending which condition applies first. The Fourier time is proportional to $J \cdot \lambda^3$. The J-NSE may achieve a $J = 0.5$ Tm corresponding to t = 48 ns at λ = 8 Å.

The instrument itself (see Figure 1) consists mainly of two large water-cooled copper solenoids that generate the precession field. The precession tracks are limited by the π/2-flippers in front of the entrance respectively exit of the first and second main solenoids and the π-flipper near the sample position. The embedding fields for the flippers are generated by Helmholtz-type coil

pairs around the flipper locations. After leaving the last flipper the neutrons enter an analyzer containing 60 (30 x 30 cm^2) magnetized CoTi supermirrors located in a solenoid set. These mirrors reflect only neutrons of one spin direction into the multidetector. By the addition of compensating loops the main coils and the analyzer coil are designed such that the mutual influence of the different spectrometer components is minimized.

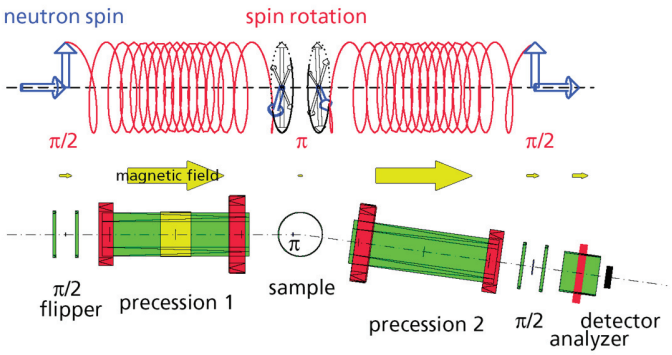

Fig. 1: *Working principle of the NSE spectrometer [2].*

Depending on its velocity, each neutron undergoes a number of precessions in the first solenoid before hitting the sample. The second solenoid after the scattering process rewinds exactly these precessions for elastically scattered neutrons, whereas inelastically scattered neutrons collect a different phase angle of rotation, $\Delta\Psi \simeq \Delta v/v^2\,\gamma\,J$, with $\gamma = 2\pi \times 2913.06598 \times 10^{-4}\,\mathrm{s}^{-1}\,\mathrm{T}^{-1}$.

The distribution of velocity changes Δv of the neutrons suffer during scattering at the sample –in terms of it's cos-Fourier transform– is measured as polarization of the neutron beam at the end of the second solenoid after the last $\pi/2$-flipper. The small velocity changes are proportional to the small energy changes $\hbar\omega$, ω being the frequency of the Fourier transform. The time parameter (Fourier time) is proportional to $\lambda^3 J$ and here in first instance is controlled by the current setting of the main coils (i.e. J). The polarization then is determined by scanning the magnetic field in one of the main coils slightly with the so called phase coil. If first and second arm are symmetric, a maximum of the polarization is measured, if the phase of the spins is shifted by 180 degree by variation of the field of one coil, one gets to a minimum of intensity. With a 360 degree variation one gets to the next maximum and so on. These oscillations are shown in Figure 2. The amplitude of this echo is normalized to the difference between maximum intensity (up-value), where all flippers are switched off, and the minimum intensity where only the π-flipper is switched on (down-value). Assuming that this normalization accounts for all imperfections of the polarization analysis in the instrument, the result yields the desired degree of polarization reduction due to inelastic/quasielastic scattering of the sample. Since the thus determined polarization reduction also contains the effects due to field integral inhomogeniety a further renormalization step is needed, which is equivalent to a resolution deconvolution in a spectroscopic instrument as e.g. the backscattering spectrometer. In order to be able to perform this resolution correction the same experimental and data treatment procedure has to be carried out with an elastic scatterer.

The scattering vector Q is determined by the angle 2θ of the second arm of the spectrometer with respect to the first one by $Q = 4\pi/\lambda \sin(\theta)$. The Fourier time t is proportional to the magnetic field of the main solenoids. At a given scattering vector Q, the magnetic field is successively increased and an echo group is recorded for each setting to obtain $I(Q, t)$ as a function of t.

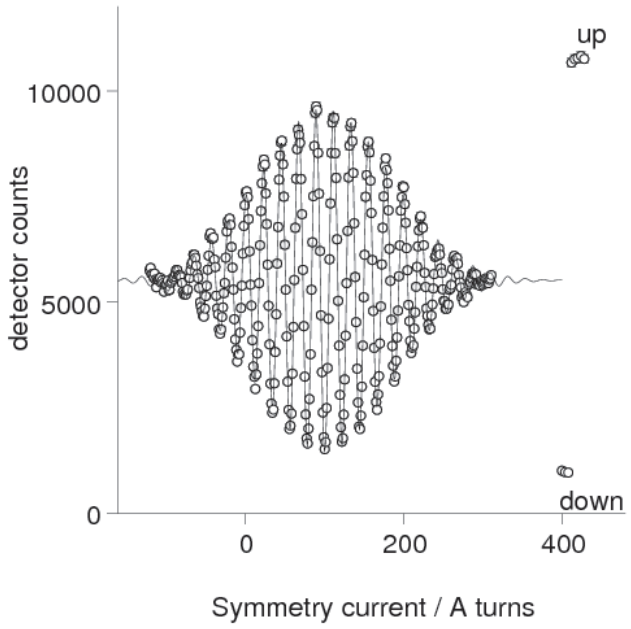

Fig. 2: *Echo group measured with the NSE instrument.*

2.1 Separation of coherent and incoherent scattering

By the use of polarized neutrons it is possible to separate the coherent and spin incoherent part of the scattering, since the incoherent scattering changes the polarisation to $-1/3$. For different scattering vectors Q the scattering intensity is measured, once in the spin-up configuration and once in the spin-down setup. In the spin-up configuration all spin flippers are switched off and the longitudinal, in forward direction (i.e. parallel to the magnetic field) polarized beam can pass through the spectrometer. The analyzer in front of the detector transmits those polarized neutrons. The measured intensity at the detector in this configuration is the maximum possible intensity. In the spin-down configuration only the π flipper at the sample position is switched on, which rotates the neutron spin orientation by $180°$. The spin direction is now against the magnetic field direction and in the ideal case the analyzer completly absorbs the neutrons, so that the minimal possible detector intensity is measured. Omitting background effects and assuming perfect flipping ratio (ratio spin-up/spin-down = ∞ in the direct beam) coherent and incoherent

scattering contributions can be separated as follow (with Up: detector intensity in the diffraction run with all flippers off, $Down$: detector intensity in the diffraction run with only π flipper at sample position on, I_{coh}: coherent scattered intensity, I_{inc}: incoherent scattered intensity)

$$Up + Down = I_{coh} + I_{inc} \tag{1}$$

$$Up - Down = I_{coh} - 1/3 * I_{inc} \tag{2}$$

which gives

$$Up = I_{coh} + 1/3 I_{inc} \tag{3}$$

$$Down = 2/3 I_{inc} \tag{4}$$

respectively

$$I_{inc} = 3/2 Down \tag{5}$$

$$I_{coh} = Up - 1/2 Down \tag{6}$$

To include nonideal flipping ratio and background count rate the calculation is more difficult.

3 Polymer dynamics

There are different models to describe the dynamics of large molecules. A nice overview is given in the book "Neutron Spin Echo in Polymer Systems", which is also available online [3].

The conformation of a linear polymer chain follows a random walk, this means a chain segment of length l can move freely around the neighboring segment (within the limitation of chemical bonds). With a set of segment vectors $\mathbf{r}_n = \mathbf{R}_n - \mathbf{R}_{n-1}$, where $\mathbf{R}_n$ is the position vector of segment n, the distance between segments which are n steps apart follows a Gaussian distribution [3]:

$$\Phi(R, n) = \left(\frac{3}{2\pi n l^2}\right)^{3/2} \exp\left(-\frac{3R^2}{2nl^2}\right) \tag{7}$$

with l the segment length.

By summing up the scattering amplitudes of the centres of the segments of a polymer chain with the correct phases, one obtains the scattering function of the polymer chain (see Lecture on Dynamics of Macromolecules for more details):

$$I(Q, t) = \langle \sum_{n,m=1}^{N} \exp[i\mathbf{Q} \cdot (\mathbf{R}_n(t) - \mathbf{R}_m(t))] \rangle \tag{8}$$

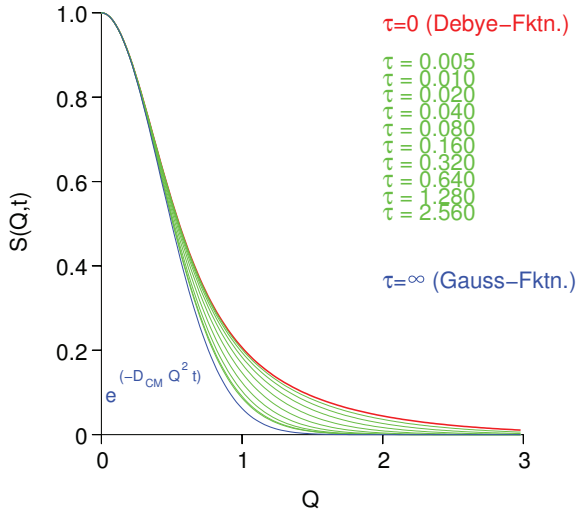

Fig. 3: *Time development of $I(Q,t)/I(Q,0)$ (here denoted $S(Q,t)$ for a Gaussian chain in the Rouse model.*

A snapshot of the chain, i.e. the static structure factor, is obtained for $t = 0$. One gets the well known Debye funktion:

$$I(Q) = N f_{Debye}(Q^2 R_g^2) \tag{9}$$

$$f_{Debye}(x) = \frac{2}{x^2}(e^{-x} - 1 + x) \tag{10}$$

with R_g the radius of gyration of the chain. In Figure 3 the Debye function and its time evolution is displayed.

3.1 Rouse dynamics

In the Rouse model the Gausssian polymer chain is described as beads connected by springs. The springs correspond to the entropic forces between the beads and the distance between the beads corresponds to the segment length of the polymer. The polymer chain is in a heat bath. The Rouse model describes the movement of the single chain segments of such a polymer chain as Brownian movement. Thermally activated fluctuations (by the stochastic force $\mathbf{f}_n(t)$ with $< \mathbf{f}_n(t) >= 0$), friction force (with friction coefficient ζ) and the entropic force determine the relaxation of polymer chains.

The movement of the chain segments is described by a Langevin equation:

$$\zeta \frac{d\mathbf{R}_n}{dt} + \frac{\partial U}{\partial \mathbf{R}_n} = \mathbf{f}_n(t) \tag{11}$$

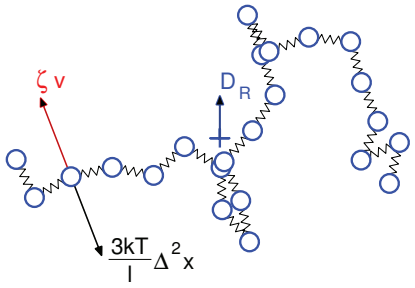

Fig. 4: *Polymer chain in the Rouse model [3] as Gaussian chain with beads connected by springs.*

The Langevin equation can be solved and one can calculate with equation 8 the intermediate scattering function, which is measured by NSE (for details, see the lecture on "Dynamics of Macromolecules"):

$$I(Q,t) = \exp(-Q^2 Dt) I_{intern}(Q,t) \tag{12}$$

with a diffusive part with a relaxation rate proportional to Q^2 and the part describing the internal relaxation, which can be written for $QR_G >> 1$:

$$I_{intern}(Q,t) = \frac{12}{Q^2 l^2} \int_0^\infty du \exp(-u - \sqrt{(\Gamma_Q t)} h(u/\sqrt{(\Gamma_Q t)})) \tag{13}$$

with the relaxation rate

$$\Gamma_Q = \frac{k_B T}{12\zeta} Q^4 l^2 \tag{14}$$

and

$$h(u) = \frac{2}{\pi} \int dx \cos(xu)(1 - e^{-x^2})/x^2 \tag{15}$$

Note that the local relaxation rate depends on Q^4. When $I(Q,t)/I(Q,0)$ is plotted against the Rouse variable $\sqrt{\Gamma_Q t}$, all curves collapse onto a master curve if the Rouse model holds.

With this model e.g. the dynamic of short polymers in the melt can be described. With increasing molecular weight other effects like the constraints imposed by mutual entanglements of the polymer chains become important, which are described in the reptation model by DeGennes (Nobel prize 1991). In this experiment polymers in solution, not in the melt, are considered. The Rouse model then needs to be extended by hydrodynamic interactions as will be described in the following section.

3.2 Zimm dynamics

Polymers in solution can be described by the Zimm model, where hydrodynamic interaction between the chain segments mediated by the solvent are dominant. Moving chain segments exert forces on other segments due to the flow of the surrounding solvent. Within some approximations the system can be described by a Langevin equation analogous to that of the Rouse model which includes the friction coefficient $\xi = 6\pi\eta a_{seg}$ with η the viscosity of the solvent. The diffusion of a chain segment depends on its hydrodynamic radius a_{seg}. More details can be found in literature [3].

In general the intermediate scattering function for polymers in solution is

$$\frac{I(Q,t)}{I(Q,0)} = F\left(\frac{k_B\,T\,Q^3\,t}{6\,\pi\,\eta}\right) \tag{16}$$

with a function $F(x)$ which depends on the polymer conformation and the quality of the solvent. The relaxation rate $\Gamma_Q = k_B\,T\,Q^3/(6\,\pi\,\eta)$ is mainly determined by the viscosity of the solvent. Internal dynamics is dominant at higher scattering vectors Q, where also the typical Q^3 dependence of the relaxation rate can be observed. At smaller scattering vectors the contribution from the center of mass diffusion is more prominent so that rather a Q^2 dependence of the relaxation rate is expected (see below). For not too small Q values and long polymer chains, where the end-to-end distance of the chain segments follow Gaussian statistics (Gaussian chain), the function $F(x)$ can be written as:

$$\begin{aligned} F(x) \;=\; & \int_0^\infty \exp\Big(-u - x^{2/3}\frac{2}{\pi}\int_0^\infty \frac{\cos(y\,u\,x^{-2/3})}{y^2} \\ & \times\Big[1-\exp\Big(-\frac{y^{2/3}}{\sqrt{2}}\Big)\Big]\mathrm{d}y\Big)\mathrm{d}u \end{aligned} \tag{17}$$

This more complex function can be approximated by a stretched exponential function over a wide Q range:

$$F(x) \simeq \exp\Big(-\Big(\frac{x}{b}\Big)^{\beta}\Big) \tag{18}$$

with the parameters $b \simeq 1.354$ and $\beta \simeq 0.85$. For the evaluation of this experiment this approximation of $F(x)$ can be used.

3.3 Center of mass diffusion

With NSE spectroscopy the movements on length scales in the order of nanometer and time scales in the order of nanoseconds can be observed. This matches e.g. the center of mass diffusion of macromolecules in solution or micelles. The mean square displacement of a particle is $< r^2(t) >= 6D_0t$ with the diffusion constant $D_0 = k_BT/(6\pi\eta R_G)$, where R_G is the hydrodynamic particle radius and η the viscosity (Stokes-Einstein-relation). The dynamic structure factor which is measured by NSE is then

$$I(Q,t)/I(Q,0) = \exp\left(-1/6 < r^2(t) > Q^2\right) = \exp\left(-D_0tQ^2\right) \tag{19}$$

A simple diffusion therefore has a quadratic dependence on the scattering vector Q.

4 Preparatory Exercises

1. How fast do neutrons with a wavelength of 8 Å fly?

2. What is the value of the earth's magnetic field?

3. What is the magnetic field at the surface of a common permanent magnet?

4. How many mm fall neutrons on their way from the entrance of the spectrometer to the detector (about 7 m) due to gravity?

5. How many precessions does a neutron of $\lambda = 8$ Å perform in the main coils if the Fourier time is set to 20 ns? (Angle $\Psi = \gamma/v \int Bdl$ with $\gamma = 2\pi \cdot 2913.06598 \times 10^4 (s \cdot T)^{-1}$.

5 Experiment Procedure

5.1 The experiment itself

First, the function of the key components of the neutron spin-echo spectrometer will be explained and demonstrated.

The generation of the "Spin Echo" will be demonstrated with an auxiliary phase coil, wound around one of the main precession coils with a simple wire. With a laboratory DC-powersupply connected to this coil, the magnetic field inside this main coil is slightly varied. A fully symmetrical setup with identical magnetic path integrals in both main coils results in a maximum count rate at the detector. Increasing the current in the auxiliary coil from this point results in an additional phase shift of the neutron spin and thus the intensity varies from the maximum to a minimum and further to the next maximum and so on. In this way, the echo group is scanned.

The experimental sample under investigation is a polymer chain (PEP, polyethylenepropylene) with a molecular weight of 70 kg/mol in solution (deuterated decane). The PEP concentration is 3 wt %. The first experiment with the sample is to measure the elastic scattering by recording the spin-up and spin-down intensity at the detector.

- The coherent and incoherent scattering of the sample shall be extracted from this reading and plotted versus the scattering vector Q.

The dynamics of the sample is measured. For some selected scattering vectors Q, a series of Fourier times is measured for the sample, for a background sample containing everything but the objects under investigation, in this case the pure deuterated solvent (d-decane), and for an elastic scatterer as reference.

5.2 Data reduction

Each Fourier time is determined by measuring 2-3 oscillations of the echo bunch and fitting the theoretical curve (a cosine oscillation with a gaussian envelope) to the points. In short, the normalized amplitude of the fitted curve is the degree of polarization wanted in this measurement. This procedure is done with a program called `echodet`, which creates the files containing the intermediate scattering function $I(Q,t)$.

5.3 Data evaluation

The $I(Q,t)$ vs. t is contained in the files b_XXXXX as ascii-data.

- Read in the data with some data treatment program (e.g. `qtiKWS9`).
- Fit the data with a model function. First use a simple exponential function $I(Q,t) = A\exp(-\Gamma t)$ and determine the relaxation rate Γ. For diffusion like behaviour with the Stokes-Einstein diffusion coefficient, $\Gamma = DQ^2$ should be valid. Plot Γ/Q^2 to check the validity of the model. It also allows for the determiation of the hydrodynamic radius of the particle assuming a viscosity of d-decane of $\eta = 0.954 \times 10^{-3}$ kg/(m s).
- Use a stretched exponential function as model function: $I(Q,t) = A\exp(-[\Gamma t]^{\beta})$ and determine the relaxation rate Γ and the stretching exponent β. The Zimm model would predict that the rate depends on the viscosity η as $\Gamma = k_B T/(6\pi\eta)Q^3$. Which is the viscosity of d-decane? Does the Q-dependence of the model describes that of the data correctly (i.e. is $\Gamma/Q^3 = const.$)?

6 Experiment-Related Exercises

Data evaluation (the bullet points in section 5):

1. Separate coherent and incoherent scattering from elastic scan (diffrun) and plot it.
2. Evaluate the data containing $I(Q,t)$ vs t with the models as described in the previous section and discuss the results.

General questions:

1. Why are no iron yoke magnets used in the construction of a NSE spectrometer?
2. What is the maximum field inside the main precession coils of the J-NSE?
3. What determines the resolution of the spin echo spectrometer?
4. How does the signal look like if the scattering is spin-incoherent? (Hint: in this case 2/3 of all neutron spins get flipped in the scattering process.)

5. What is the measured effect of the spin echo spectrometer?
6. What is measured finally?

References

[1] F. Mezei, editor. *Neutron Spin Echo, Proceedings Grenoble 1979*, volume 128 of *Lecture Notes in Physics*. Springer, 1980.

[2] D. Richter M. Monkenbusch, R. Schätzler. *Nucl. Instr. Meth. in Phys. Res. A*, 399:301–323, 1997.

[3] D. Richter, M. Monkenbusch, A. Arbe, and J. Colmenero. *Adv. Polym. Sci.*, 174:1–221, 2005.

Contact

J-NSE

Phone: 089/289-14903
Web: http://www.jcns.info/jcns_nse

Olaf Holderer

Jülich Centre for Neutron Science, Outstation at the FRM II
Forschungszentrum Jülich GmbH

Phone: 089/289-10707
e-Mail: o.holderer@fz-juelich.de
Web: http://www.jcns.info

Michaela Zamponi

Phone: 089/289-10793
e-Mail: m.zamponi@fz-juelich.de
Web: http://www.jcns.info

KWS-1 & KWS-2

Small Angle Neutron Scattering

H. Frielinghaus, M.-S. Appavou

Jülich Centre for Neutron Science
Forschungszentrum Jülich

Manual of the JCNS Laboratory Course Neutron Scattering

Contents

Fig. 1: *Representation of the protein lysozyme, which has a very compact form.*

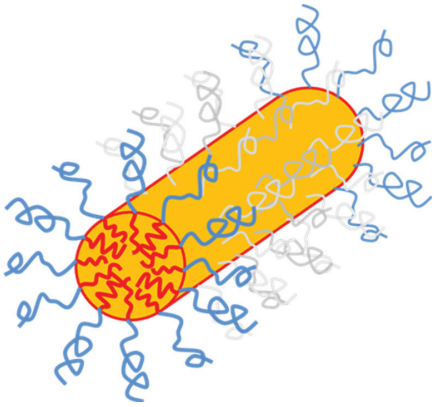

Fig. 2: *Schematic representation of a cylindrical micelle, which is composed of amphiphilic polymers.*

1 Introduction

The objective of this lab course is to clarify the essential concepts of small-angle neutron scattering. Structures are only visible by a scattering experiment if there is an appropriate contrast. For neutrons one often uses the exchange of ^{1}H by ^{2}H, i.e. deuterium. The scattering length density difference is responsible for the contrast of a small-angle neutron scattering experiment. We will investigate the protein Lysozyme in heavy water (Fig. 1) to obtain the information about the typical distance of the molecules. A second example is a micellar solution of the amphiphilic polymer POO_{10}-PEO_{10} in heavy water (Fig. 2). The chosen contrast makes only the core of the micelle visible. The core is very compact because of the hydrophobic interaction. The aim of this second part is to determine the radius of the cylindrical structure.

2 The Protein Lysozyme in Water

For this part of the experiment a Lysozyme solution of 0.02g per ml of water must be prepared. We will use deuterium oxide to prepare the solution of ca. 1ml. We will weigh exactly 0.02g of Lysozyme and put it into a new Packard glas. With an Eppendorf pipette we will add exactly 1 ml D_2O. These pipettes are extremely accurate with respect to the volume. From the solution about 0.5 to 0.6ml are transferred to Hellma quartz cuvettes, which are 1mm thick. The experimental part in the chemistry lab is finished.

3 The Diblock Copolymer POO_{10}-PEO_{10}

This polymer is an amphiphilic diblock copolymer. It consists of the monomers octyl-oxide and ethylene oxide. The monomers were consecutively polymerized and are now forming polymers.

The POO-block has a molar mass of 10kg/mol. The symmetrical polymer has about the same molecular weight in the PEO block. The PEO is deuterated in this polymer. Using heavy water especially the contrast of the POO-hydrophobic block to PEO and D_2O is highlighted. This means that in the scattering experiment the micelle core will be particularly well visible, the corona will be not. Because these polymers are very expensive, a 0.1% solution is available for the scattering experiment.

4 The Measurement at KWS-1 and/or KWS-2

These two solutions are now being measured in the small-angle neutron scattering instrument KWS-1 (or KWS-2). The wavelength of neutrons is set to 7Å. The collimation is fixed to 8m. The samples are placed as close as possible to the detector, to measure the largest Q values possible. Both samples will be measured at detector distances 2m and 8m. The offset between the sample position and the detector of about 30cm leads to effective detector distances of about 1.7m and 7.7m.

The sample holder will be filled with the two samples. In addition, the empty beam and a plexiglass plate are measured for absolute calibration. For a good statistical measurement the following times are set: 8m detector distance for 20min, and 2m detector distance 10min. The total measuring time for the 4 positions will be about 2 hours. The measurement is typically started before lunch, and can be evaluated in the afternoon. It is quite likely that an internal employee will start separate measurements during the afternoon until the next morning in order to use the valuable measuring time overnight.

5 Evaluation of the Scattering Data: Absolute Calibration

The measured data is raw data at first and describes the intensity on the detector. The data has to be corrected for the effectiveness of the different detector channels. Then the empty beam measurement is deducted to account for the zero effect of the instrument. Then the intensities are expressed as absolute units using Eq. 5.5 and are radially averaged, because for the isotropic scattering samples, the intensity does not depend on the polar angle. To perform all these steps we will be using a software available in our institute, called QtiKWS. However, since the understanding of the Eq. 5.5, as such, is more important than the exact technical understanding of the evaluation, the results are produced relatively quickly by the software, namely, $\mathrm{d}\Sigma/d\Omega$ as a function of the scattering vector Q for our samples. This data will be provided for the students to do the final evaluation. In the following, this evaluation is described.

6 Evaluation of Lysozyme Scattering Curves

The position of the maximum $Q_{\max}$ provides information on the typical distance of the proteins in solution. This can be calculated to $\ell = 2\pi/Q_{\max}$. Knowing the weight of the protein in water (0.02g/cm^3) there is an alternative way to calculate the average distance. The molar

mass of the protein is 1.43×10^4g/mol. The number density of the protein is therefore $n/V = 0.02\text{g/cm}^3/(1.43 \times 10^4\text{g/mol}) = 1.40 \times 10^{-6}\text{mol/cm}^3 = 8.42 \times 10^{-7}\text{Å}^{-3}$. For a simple cubic packing the typical distance is given by $\ell = \sqrt[3]{V/n}$. For a hexagonal packing the typical distance is $\ell = \sqrt[6]{2}\sqrt[3]{V/n}$. Both calculated distances are to be compared with the measured one.

7 Theoretical Background for Cylindrical Micelles

Now a formula for the macroscopic scattering cross section of an infinitely long cylinder with a finite radius will be discussed. This cylinder is assumed to be infinitely long, because the experimental Q-window is not sufficient to observe the entire particle as a whole.

So our scattering formula does not have a Guinier region for the entire cylinder. Moreover, the question about the orientation of the cylinder arises, because this particle is no longer isotropic. Simple sample preparations (like in the case of the lab course) do not impose a preferred orientation of the particles and they are oriented arbitrarily and therefore scatter isotropically. The presented macroscopic scattering cross section was calculated with an orientational average, which however will not be discussed in detail. One finds:

$$\frac{d\Sigma}{d\Omega}(Q) = (\Delta\rho)^2 \cdot \phi_{\text{cyl}} \cdot A_{\text{cyl}} \cdot \frac{\pi}{Q} \cdot \left(2\frac{\text{J}_1(QR)}{QR}\right)^2 \tag{1}$$

You get individual factors with the following meanings: (a) contrast, (b) the concentration of the cylinders, (c) the cross-sectional area of the cylinder, (d) a form factor part for infinitely long cylinders and (e) a form factor part of the shape of the cross-sectional area, which is simply a circle. Since the Guinier region of the entire cylinder slides out of the Q-window, the observable particle volume is reduced to a cross section A_{cyl} of the cylinder. In addition, the total form factor can be expressed as the product of two terms. This is possible if the entire structure can be expressed as a convolution of two simpler structures. In this case, this is an infinitely thin infinitely long cylinder and a flat disk perpendicular thereto. The convolution is a cylinder with a finite cross section. The infinitely long cylinder is described by the term π/Q. While having strong oscillations for finite lengths, in the limiting case this factor yields just a power law – similar to the Porod-law. The orientation-averaged disc has a rather complicated expression with a first-order Bessel function. The first zero is at $Q = 3.832/R$. This factor can also be regarded as a separate form factor with its own Guinier region. In this case, eq. 1 would be written as follows:

$$\frac{d\Sigma}{d\Omega}(Q) = (\Delta\rho)^2 \cdot \phi_{\text{cyl}} \cdot A_{\text{cyl}} \cdot \frac{\pi}{Q} \cdot \exp\left(-\frac{1}{4}Q^2R^2\right) \tag{2}$$

These two principal areas of Guinier regions derive from a scale separation. On the one hand, the cylinder is very long, and the first Guinier region disappears at very low Q. On the other hand, one finds a Guinier region of a circular disk of radius R in our Q-window. Both Guinier regions are clearly separated in reciprocal space. It is just that the observed Guinier region is covered by an additional form factor for an infinitely long, infinitely thin cylinder. The radius of

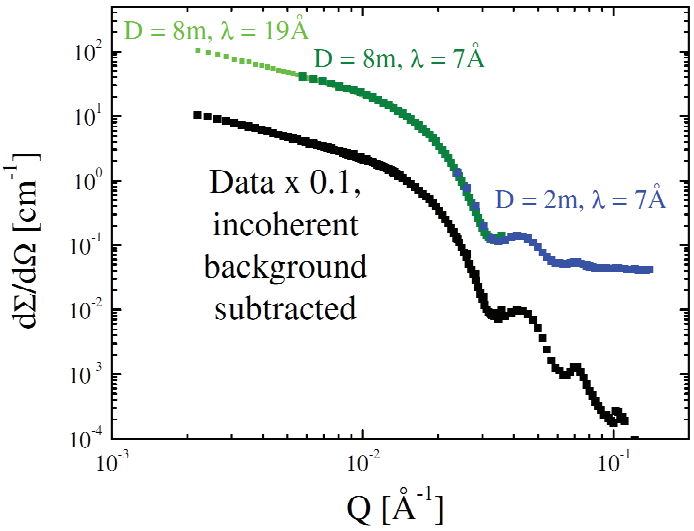

Fig. 3: *Measured scattering curve of POO_{10}-PEO_{10} micelles. The bright green data are measured at a longer wavelength, and are not intended to be repeated in the lab course. Here you can see, however, the Q^{-1} behavior, which clearly speaks for the cylindrical shape of the micelle core. The dark green and blue dots are measured in the lab course. The sharp drop of the curve at about 0.1Å^{-1} shows the Guinier region of the cylinder cross section. This is evaluated in further detail. Two minima and maxima follow at higher scattering vectors Q before the incoherent background is noticeable. Black data points, shows the curve without background (moved down to clarify the distinction).*

the cylinder can be determined from scattering data, when plotting $\ln(Q \times d\Sigma/d\Omega)$ as a function of Q^2.

8 Evaluation of the POO_{10}-PEO_{10} Scattering Curves

The entire scattering curve is first plotted in a log-log representation (Fig. 3). While in the shown diagram, the curve is measured to even smaller Q, the larger Q values suffice for the lab course ranging from about 0.006 up to 0.2Å^{-1}. We see a strong drop in intensity at about 0.01Å^{-1}. In this area the Guinier region of the cylinder cross section is found. Note that the contrast was chosen in a way, such that only the micelle core is visible. At higher Q two minima and maxima are found, which describe the sharp boundary of the micelle core. These two oscillations become clearly visible when the incoherent background is subtracted. It will be sufficient for the lab course to calculate the average of seven data points from the highest scattering vectors and subtract it. The quality of the measurement is only visible in this representation.

The basis for our further analysis is the Guinier-plot (Fig. 4). In the Gunier-plot $\ln(Q \times d\Sigma/d\Omega)$ is plotted against Q^2. On the one hand, the data points show no significant slope for the smallest Q. On the other hand the examined Q values cannot be too big, because then the Guinier

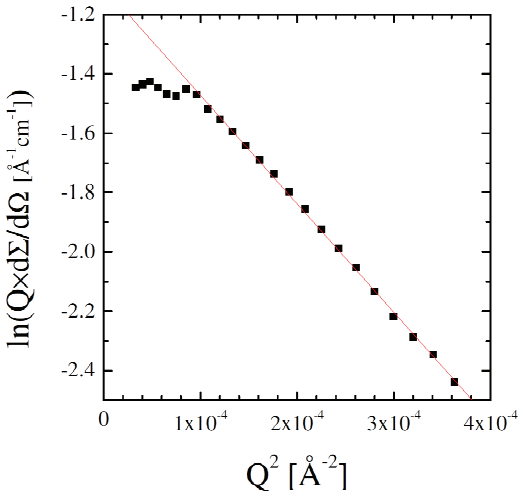

Fig. 4: *Guinier plot for cylindrical cross section. The first data points of the 8m, 7Å measurement indicate no slope. The data points for larger Q values than 0.02Å^{-1} are neglected.*

analysis is no longer valid. From the slope of the regression one can extract the diameter of the cylinder cross section (see Eq. 2). This is in the range of 120Å. For the validity of the Guinier assumption, the product of the highest Q value taken and the obtained radius can be calculated. This yields 0.02Å^{-1} $\times$ 120Å$=$ 2.4. This value is not much larger than $\sqrt{4}$. Therefore, the Guinier approximation is a good estimate for the cylinder diameter. The measurement error of the obtained radius is to be specified.

Alternatively, the first minimum $Q_{\min}$ in Fig. 4 can be used for calculating the cylinder cross section. The radius is calculated according to $R = 3.832/Q_{\min}$. The two different radii are to be compared. Is the Guinier condition $QR < 2$ well enough fulfilled? Which result is more precise?

9 Preparatory Exercises

(I) Lysozyme in D_2O

The first sample of the Neutron Lab Course at the SANS instrument KWS-1 (KWS-2) will be Lysozyme in heavy water (D_2O). This protein is rather globular (diameter ca. 5 nm). The Coulomb interactions of this charged molecule lead to liquid-like short-range-ordering. This will be observed in the SANS scattering experiment by a correlation peak. Simple estimations will be made now:

1. Give the connection between the number density ϕ and the unit cell parameter assuming a simple cubic lattice!
2. The chemical concentration c is usually given in g/L or mg/ml. The molar mass of the

molecule is 14307g/mol. What is the connection between the chemical concentration and the number density?

3. The correlation peak appears at a scattering vector $Q_{\max}$. How would it relate to the unit cell parameter of a simple cubic lattice? What is the dependence of $Q_{\max}$ as a function of the chemical concentration c?

4. If the packing of the globules was fcc (face centered cubic) or hexagonal (with arbitrary layer order) the system is more dense by a factor of $\sqrt[6]{2}$. What would be the function $Q_{\max}(c)$?

(II) Cylindrical Micelles in D_2O

The Q-dependence of the scattering curve will be evaluated in two different ways to obtain the diameter of the cylinders.

1. The Taylor expansion for small scattering vectors Q yields the following functional form $I(Q) \propto Q^{-1} \cdot \exp(-\frac{1}{4}R^2Q^2)$. What would you plot in a simple graph to obtain a linear dependence? Which role does the radius R play in this graph?

2. Knowing that the formula occurs from a Taylor expansion with the parameter $x = QR$ around the point $x = 0$, what would be criterion for a good approximation? (Don't argue too mathematically!)

3. As for many compact (and monodisperse) bodies the scattering curve shows oscillations. The first minimum of such a curve also indicates the radius of the cylindrical micelle. Mathematical calculations yield $Q_{\min} = 3.832/R$. This is another example for connections in real space to reciprocal space. Where does the name reciprocal space come from?

4. The mathematical form of an ideal, infinitely long cylinder with a radius R would predict a zero intensity for the $Q_{\min}$-value. Why would we observe a finite intensity nonetheless?

Contact

KWS-1 & KWS-2

Phone: +49-89-289-14324 & +49-89-289-14326
Web: http://www.jcns.info/jcns_instruments

Henrich Frielinghaus

Jülich Centre for Neutron Science
Forschungszentrum Jülich GmbH
c/o TUM, FRM 2
Lichtenbergstrasse 1
85747 Garching

Phone: +49-89-829-10706
e-Mail: H.Frielinghaus@fz-juelich.de

Aurel Radulescu

Jülich Centre for Neutron Science
Forschungszentrum Jülich GmbH
c/o TUM, FRM 2
Lichtenbergstrasse 1
85747 Garching

Phone: +49-89-829-10712
e-Mail: A.Radulescu@fz-juelich.de

Zhenyu Di

Phone: +49-89-289-10758
e-Mail: Z.Di@fz-juelich.de

Artem Feoktystov

Phone: +49-89-289-10746
e-Mail: A.Feoktystov@fz-juelich.de

Marie-Sousai Appavou

Phone: +49-89-289-10747
e-Mail: M.S.Appavou@fz-juelich.de

Noemi Szekely

Phone: +49-89-289-10739
e-Mail: N.Szekely@fz-juelich.de

KWS-3

Very Small Angle Neutron Scattering Diffractometer with Focusing Mirror

Vitaliy Pipich

Jülich Centre for Neutron Science
Forschungszentrum Jülich

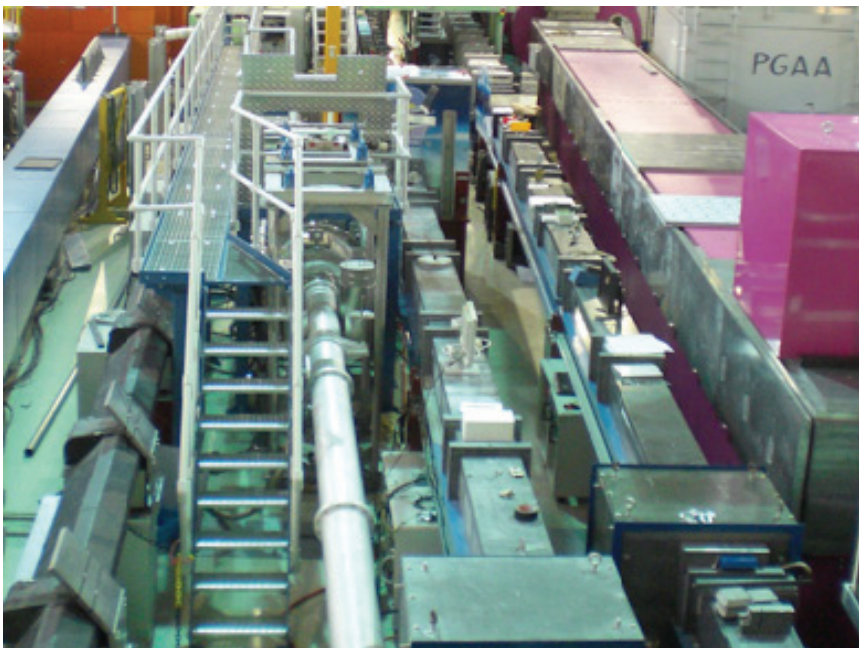

Manual of the JCNS Laboratory Course Neutron Scattering

Contents

1 Introduction

Ultra small angle (USANS) and small angle neutron scattering (SANS) experiments are performed by two different types of instruments to cover a combined Q-range from 10^{-5}Å^{-1} up to 1Å^{-1}. Double crystal diffractometers are used for USANS experiments, whereas the "standard" SANS experiment is performed using a pinhole camera. In principle, the Q-range of both instrument classes overlaps. Typical USANS instruments like S18 (ILL) or PCD (NIST) may reach maximum Q-vectors of $5{\cdot}10^{-3}$Å^{-1}. The disadvantage of these instruments is that they do not allow taking a full area image on a 2D position sensitive detector. On the other hand, the well-known pinhole instrument D11 at Institut Laue-Langevin (France) reaches a minimum Q-vector of $3{\cdot}10^{-4}$Å^{-1} by use of largest possible wavelength 22Å and sample-to-detector distances (>40 m). But the required instrumental settings push both types of instruments to their limits, mainly due to signal-to-noise level and the reduced flux at sample position. The use of neutron lenses as additional elements of a pinhole SANS instrument has been tested to overcome this intensity problem [1].

An alternative design is realized by the KWS-3 instrument [2]. The principle of this instrument is a one-to-one image of an entrance aperture onto a 2D position-sensitive detector by neutron reflection from a double-focusing elliptical mirror. It permits to perform SANS studies with a scattering wave vector resolution between 10^{-4} and 10^{-3}Å^{-1} with considerable intensity advantages over conventional pinhole-SANS instruments and double crystal diffractometers. Therefore it perfectly bridges the "Q-gap" between USANS and SANS: Very Small Angle Scattering (VSANS). The increasing need for these intermediate Q-vectors arises from the growing interest in biological and colloidal samples, which partially deal with length scales in the µm range. An investigation of the multilevel structures in partially crystalline polymer solutions performed using a combination of those three above depicted types of SANS instruments can be found in [3].

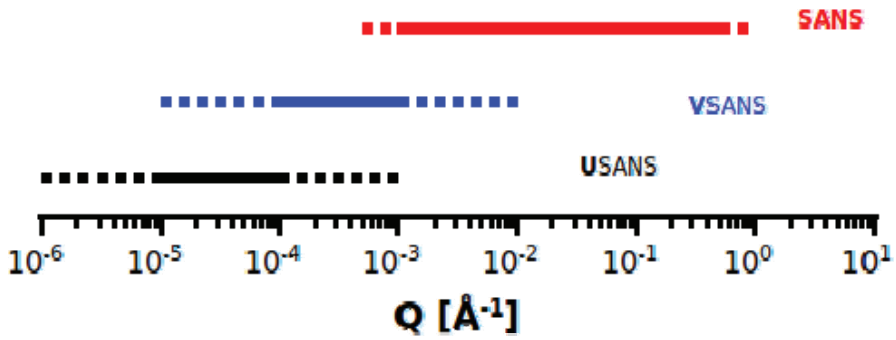

Figure 1: Focused VSANS fills space between USANS (double crystal diffractometer) and classical SANS instruments.

The main innovation and challenge of KWS-3 was to build a large mirror having a shape as close as possible to an ellipsoid and with a surface roughness less than 5 Å. The mirror is a

1.2 m long, 0.12 m wide and 0.05m thick toroidal double focusing mirror of 11 m focal length. At such a short mirror length with respect to the focal length, the toroidal shape is a good enough approximation to an elliptical shape. The reflection plane has been chosen to be horizontal, reducing the deterioration of the image due to gravity. A photo of the mirror is given in Figure 1.

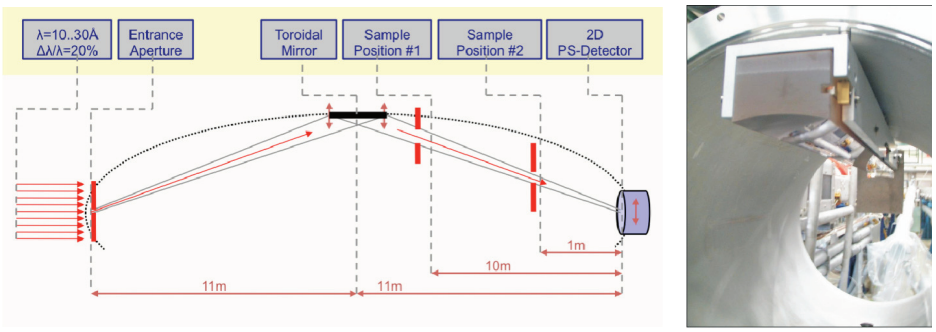

Figure 2:(left) layout of KWS-3;(right) toroidal mirror installed in vacuum its chamber.

KWS-3 is optimized for very small angle scattering range from 10^{-4} to $3\cdot10^{-3}$Å^{-1}. For last cold source filling and instrument configuration the flux at the sample position (and detector) is near **11500** counts per full sample area by use 12.5Å wavelength with 20% wavelength spread, 2x2 mm^2 entrance aperture and 20x100 mm^2 beam size sample-to-detector distance at 9.5 meters.

2 VSANS applications

All applications of the classical SANS could be investigated by VSANS by taking into account Q-resolution of VSANS. The conventional fields of application of very small angle scattering studies are:

- particles in solution [protein aggregates, polymers, micelles, ceramics];
- porous materials [cement, paste, rocks, coal etc.];
- inhomogeneous metallic alloys;
- bulk samples with artificial regular structure [phase gratings];

and other inhomogeneities on a size range from 50 nm to 5 μm, often in addition to SANS spectra, but also diffraction, reflection and refraction studies on surfaces.

3 Preparatory Exercises

1. The contrast variation (CV) is a very important feature of the neutron scattering. What is the scattering length density (SLD) ρ? How to calculate the SLD? What is the definition of the scattering contrast Δρ? How to carry out the contrast variation experiment in case of an aqueous solution of particles?

2. The standard Q-range of KWS-3 is from 10^{-4} to $3\cdot10^{-3}$Å^{-1}. What the size of particles could be investigated in this Q-range? What are the form factor P(Q) and structure factor S(Q)? In which case the scattering intensity $d\Sigma/d\Omega(Q)$ could be represented as a product of the structure factor and form factor $d\Sigma/d\Omega(Q)= d\Sigma/d\Omega(0)\cdot P(Q)\cdot S(Q)$? What is the physical "content" of the forward scattering $d\Sigma/d\Omega(0)$ [I(0)]?
3. The standard wavelength at KWS-3 is 12.5Å. What are disadvantages of this wavelength? What should we correctly select before sample preparation?
4. What is the difference between pine-hole SANS and focused SANS? Why the beam size at KWS-3 is 20cm^2?

4 Experiment Procedure

Within the frame of this practicum we will explore aquaeous solution of monodisperse polystyrene (PS) microspheres with diameter 8000Å and the initial concentration 1% of particles in H_2O. In future, this sample will be used at KWS-3 as "a standard sample" to check the performance of instrument, absolute calibration, instrument resolution.

In Table 1 there is collected information about PS microspheres obtained from the producer; additionally all necessary information about H_2O and D_2O is listed there.

Table 1. Parameters of used components

	Polystyrene Spheres	H_2O	D_2O
Scattering Length Density [Å^{-2}]	$1.41\cdot10^{-6}$	$-0.56\cdot10^{-6}$	$6.50\cdot10^{-6}$
Density, 20°C [g/cm^3]	1.05	1.0	1.05
Radius [Å]	4000±45		

The contrast variation is proposed to proceed simply by step-by-step adding of D_2O to the initial H_2O solution of spheres. To estimate how much of D_2O we should add, the simulation of the forward scattering should be done as function of D_2O concentration:

$$\frac{d\Sigma}{d\Omega}(0) = \Phi_{Spheres} V_{Spheres} \left(\rho_{Spheres} - \rho_{Water}\right)^2,$$

where $V_{Spheres}$ is volume of PS spheres, $\rho_{Spheres}$ SLD of PS spheres, ρ_{Water} SLD of D_2O/H_2O mixture, $\Phi_{Spheres}$ volume fraction of PS spheres in D_2O/H_2O mixture. We could rewrite the above-mentioned equation in terms of Φ_0 and Φ_{D2O}, the volume fraction of PS spheres in the initial H_2O solution and volume fraction of D_2O in D_2O/H_2O mixture respectively:

$$\frac{d\Sigma}{d\Omega}(0) = \frac{\Phi_0(1-\Phi_{D2O})}{1-\Phi_0\Phi_{D2O}} V_{Spheres}\left[\rho_{Spheres} - \rho_{H2O} - \Phi_{D2O}(\rho_{D2O} - \rho_{H2O})\right]^2.$$

In Figure 3 the forward scattering $d\Sigma/d\Omega(0)$ as a function of Φ_{D2O} and Φ is plotted. At the starting point of the experiment (Φ_{D2O}=0) we have PS spheres in pure H2O and maximal volume fraction of spheres $\Phi_{Spheres} = \Phi_0 = 1\%$. Minimum of the plotted curve corresponds to the matching point of PS spheres in water. In Table 2 seven points around matching concentration are labeled with "CV" mark. In case of CV, from the scattering curves of above-mentioned samples we need to extract only "integral" parameter forward scattering to

extract information about minimum of the forward scattering, and plot it as function of D_2O content.

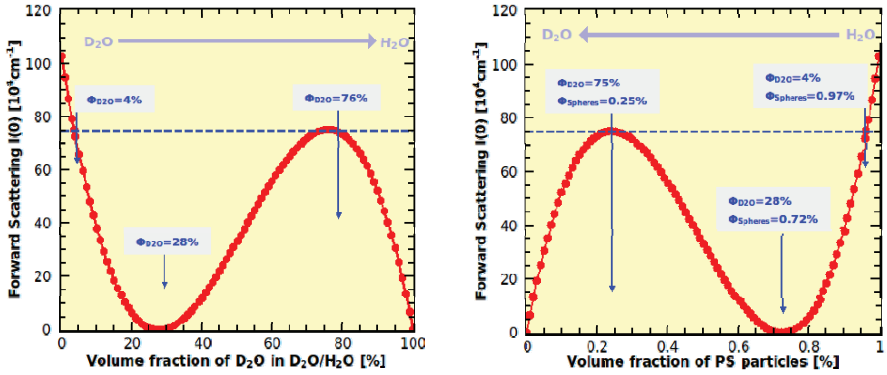

Figure 3. Forward scattering as a function of Φ_{D2O} and Φ.

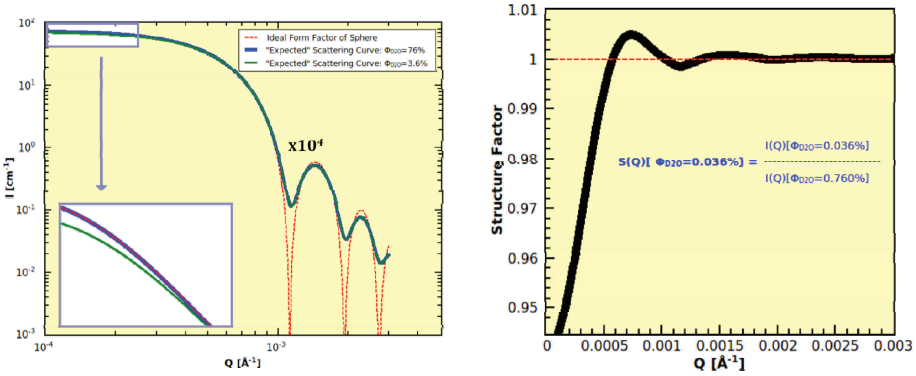

Figure 4: Expected results. (Left) the scattering signal in case of Φ_{D2O}=0.04 and 0.76. In the amplified inset is the small angle part of the calculated scattering curves. In case of Φ_{D2O}=0.04 there is clear suppression of the forward scattering due to the hard sphere interactions. Calculated scattering curve in case of the sample with Φ_{D2O}= 0.76 shows no interaction term. Red curve is pure form factor of PS spheres without taking into account instrumental resolution function. (Right) Ration between Φ_{D2O}=0.04 and Φ_{D2O}=0.76 is plotted here. So the forward scattering and form factor of both sample are the same, and in case of Φ_{D2O}=0.76 sample S(Q) =1, therefore this ratio is the structure factor of Φ_{D2O}=0.04 sample.

Next step is the investigation PS spheres in case of sample with D_2O content 76% [PS content 0.25%]. This point is located at the local maximum (see Figure 3). At this level of the dilution the structure factor is definitely undetectable. Please read carefully caption of Figure 4 to understand the logic of planned experiment.

Table 2. Samples for practicum; CV: samples for the contrast variation; FF, SF: sample for form and structure factor determination.

Φ_{D2O}	0 ^{CV}	3.6$^{FF, SF}$	10 ^{CV}	20^{CV}	30^{CV}	40^{CV}	50^{CV}	60^{CV}	76 ^{FF}
$\Phi_{Spheres}$	1.00	0.96	0.9	0.8	0.7	0.6	0.5	0.4	0.24
I(0)[10^4cm^{-1}]	103	75.2	38	6.5	0.47	12.01	33.2	55.9	75.2

5 The experiment and data reduction

All samples listed in Table 2 we will measure with (Sample) and without (Sample-DB) beamstop. The first one should be measured much longer than the second one. Additionally the empty cell [with (EC) and without (EC-DB) beamstop] and the black current (BC) run will be measured and used for data reduction of all datasets.

What to measure?

I_{Sample}, $I_{Sample\text{-}DB}$, I_{EC}, $I_{EC\text{-}DB}$, I_{BC} [counts per current pixel, normalized by monitor]

Sample transmission:

$$T = I_{Sample-DB} / I_{EC-DB}$$

Empty cell and black current subtraction:

$$I = (I_{Sample} - I_{BC}) - T \cdot (I_{EC} - I_{BC})$$

Absolute calibration:

$$\frac{d\Sigma}{d\Omega}(Q) = \frac{I(Q)}{d \cdot T \cdot \varepsilon_D \cdot \langle I_{EC-DB} \rangle \Delta\Omega(Q)}$$

where d sample thickness, T sample transmission, ε_D detector efficiency, $\Delta\Omega$ solid angle per current pixel, $<I_{EC\text{-}DB}>$ counts on sample.

6 Experiment-Related Exercises

Within our "one-day-experiment" at KWS-3 it would be nice to get as much as possible information about above mentioned sample, like:

a) the form factor P(Q) of PS spheres from sample with Φ_{D2O}=0.76; "real" radius R and polydispersity of the PS microspheres;
b) the structure factor S(Q) in case of Φ_{D2O}=0.04 and decide about the interactions between spheres: could we neglect the structure factor S(Q) during data analysis?

c) the scattering length density of PS spheres by H_2O/D_2O contrast variation. At matching point, the SLD of microspheres and water are equal. Polystyrene in microspheres is amorphous or crystalline?

References

[1] Eskilden, M. R. et al., Nature 391, 563 (2000);
Frielinghaus, H. et al., J. Appl. Cryst. 42, 681 (2009);
[2] Alefeld, B. et al., Physica B 283, 330 (2000);
Kentzinger, E. et al., Physica B 350, e779 (2004);
Goerigk, G. et al., J. Appl. Cryst. 44, 337 (2011);
[3] Radulescu A. et al., Macromolecules 39, 6142 (2006)

Contact

KWS-3

Phone: 089/289-14325
Web: http://www.jcns.info/jcns_kws3
http://iffwww.iff.kfa-juelich.de/~pipich/dokuwiki/doku.php/kws3

Vitaliy Pipich

Jülich Centre for Neutron Science JCNS
Forschungszentrum Jülich GmbH
Outstation at FRM II
Phone: 089/289-10710
e-Mail: v.pipich@fz-juelich.de
Web: http:// iffwww.iff.kfa-juelich.de/~pipich

Zendong Fu

Jülich Centre for Neutron Science JCNS
Forschungszentrum Jülich GmbH
Outstation at FRM II
Phone: 089/289-10716
e-Mail: z.fu@fz-juelich.de

RESEDA

Resonance Spin Echo Spectrometer

W. Häußler

Forschungsneutronenquelle Heinz Maier-Leibnitz (FRM II)
Technische Universität München

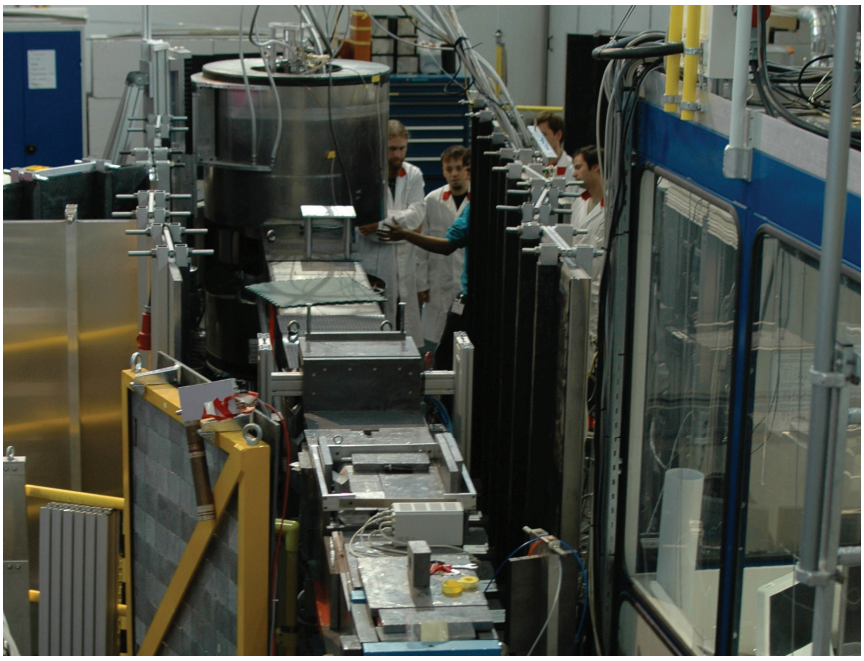

Manual of the JCNS Laboratory Course Neutron Scattering

Contents

1 Introduction

Neutrons are well suited as probes for investigating matter non-destructively, due to their large penetration depth caused by their vanishing electric charge. The energy E of a neutron with mass m corresponds to a temperature T and a velocity v:

$$E = \frac{3}{2} k_B T = \frac{1}{2} m v^2 , \quad (1)$$

where k_B is the Boltzmann constant. Then the wavelength of the neutron is given by:

$$\lambda = \frac{h}{mv}$$

with Planck`s constant h.

In neutron scattering mainly cold (E ~ 0.1 − 10meV, T ~ 1 − 120K , λ ~ 30 − 3Å), thermal (E ~ 5−100meV, T ~ 60−1000K, λ ~ 4−1Å) and hot (E ~ 100−500meV, T ~ 1000−6000K, λ ~ 1 − 0.4 Å) neutrons are used. The energy range as well as the wavelength of neutrons allows investigations of dynamics and structures of a broad range of samples. The so-called elastic neutron scattering (no energy transfer) provides the possibility to observe the structures of the studied samples. Inelastic neutron scattering (with energy transfer) and quasi-elastic scattering (with a small energy transfer) experiments provide information on the dynamics in the sample.
The fact that a neutron is a spin 1/2 particle bears another great advantage of neutron scattering: The corresponding magnetic moment of $\mu = -0.966 \cdot 10^{-26}$ J/T makes them sensitive to electro-magnetic interactions and allows to polarize neutrons by using magnetic fields in polarization devices.
In neutron spin echo (NSE), the spin of the neutron is used, in order to analyze the energy transfer in quasi-elastic scattering experiments. NSE provides high energy resolution being typically in the μeV to neV range when using cold neutrons. The NSE energy resolution does not depend on the wavelength spread of the incident beam, as opposed to other types of spectrometers.

2 Neutron Spin Echo

2.1 Elastic scattering

The NSE technique is based on the Larmor precession of polarized neutrons. To understand the basic principle, we first assume two uniform DC magnetic fields B_1 and B_2 located before and after the sample position, respectively (figure 1). We also assume elastic scattering at the sample (no energy change). An initially polarized neutron beam passes through the magnetic fields before and after being scattered at the sample. The spin of the neutrons must be aligned perpendicular to the magnetic fields (in

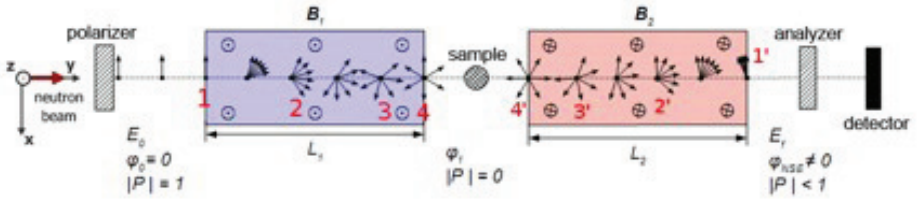

Figure 1: Basic principle of a NSE instrument (P: polariser, $B_{1,2}$: static, homogeneous magnetic fields, A: analyzer). The arrows indicate the neutron spins, which precess with the Larmor frequency. The region around the sample is located in a zero magnetic field region.

figure 1 the magnetic field points in z-direction, whereas the neutron spin points in x-direction). Then, the neutron spin precesses inside the magnetic field with the Larmor frequency $\omega_{Lar} = \gamma B$, where γ = 2.916 kHz/Gauss is the neutron's gyromagnetic ratio. The total precession phase of the neutron after passing through B_1 is proportional to the time t the neutron spends in the magnetic field. t only depends on the neutron's velocity v and the length of the magnetic field L_1. The phase of the neutron spin $\varphi_1(v)$ after the first magnetic field can be written as:

$$\varphi_1(v) = \omega_{Lar} t = \gamma \frac{L_1 B_1}{v}. \qquad (2)$$

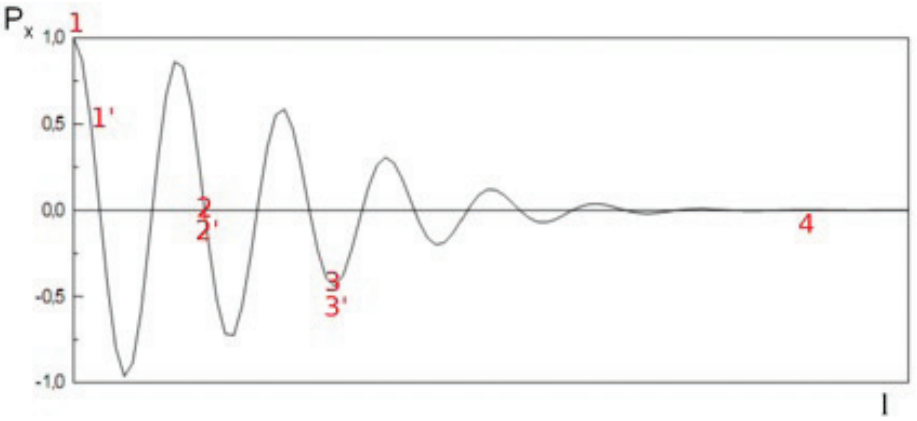

Figure 2: Polarization P_x after the first magnetic field as a function of the length of the magnetic field L_1. The positions 1 to 4 (1' to 4') correspond to the positions 1 to 4 (1' to 4') in figure 1.

The polarization is analyzed in x-direction. It is calculated from the average over all neutrons as follows:

$$P_x = \langle \cos\varphi \rangle = \int dv f(v) \cos\left(\gamma \frac{L_1 B_1}{v} \right) \qquad (3)$$

with a distribution of neutron velocities $f(v)$. Due to different neutron velocities, the envelope of the polarization decreases, if φ increases (figure 2). The shape of the measured polarization P_x is called „spin rotation group". As equation (10) shows, φ can be varied either by scanning through B_1 or by varying L_1. In figure 2, P_x is shown at

various length values l according to the positions shown in figure (1). In practice, B_1 is scanned and L_1 is kept constant, because it is easy to be technically realized.
After passing the second magnetic field B_2 behind the sample, which is antiparallel to B_1, the spin phase can be written as:

$$\varphi(v) = \varphi_1(v) + \varphi_2(v) = \gamma\left(\frac{L_1 B_1}{v} - \frac{L_2 B_2}{v}\right) \tag{4}$$

As shown in figure 1 the antiparallel field B_2 leads to a back precession of the neutron spin, denoted by the negative sign in equation (4).

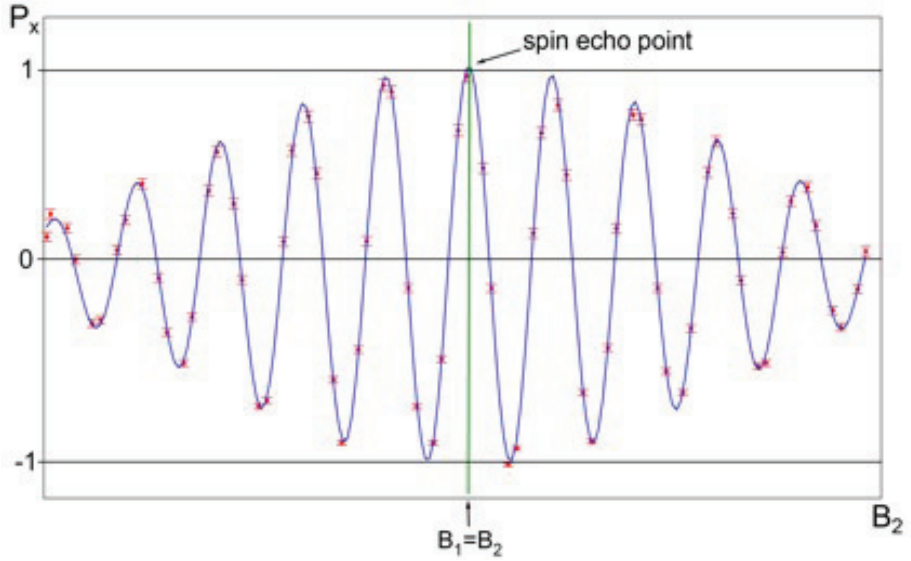

Figure 3: Spin echo group measured at RESEDA. The spin echo point represents the point where the magnitude of the magnetic field integrals and, consequently, the number of precessions in both magnetic field regions are equal. In the ideal case, the polarization reaches the value 1 in the spin echo point.

In the case of $L_1B_1 = L_2B_2$ the total spin phase of the neutron vanishes ($\varphi = 0$). According to equation (3) this leads to a polarization of $P_x = 1$. Varying one of the magnetic field integrals L_1B_1 or L_2B_2 and measuring for each set of field integrals the polarization renders the so-called *spin echo group*. Figure 3 shows a spin echo group measured at RESEDA. Here, the magnitude of the magnetic field B_1 is varied, whereas B_2, L_1 and L_2 are fixed. The center point, where $L_1B_1 = L_2B_2$ and the polarization P_x reaches its maximum, is called the *spin echo point*. At both sides of the spin echo group, the polarization decreases, as the envelope of the spin echo group equals the envelope of the spin rotation.

2.2 Inelastic and quasi-elastic scattering

In the case of inelastic scattering the kinetic energy and, consequently, the velocity of the neutrons changes. Equation (4) then reads:

$$\varphi(v) = \varphi_1(v) + \varphi_2(v) = \gamma\left(\frac{L_1 B_1}{v_1} - \frac{L_2 B_2}{v_2}\right) \tag{5}$$

where v_1 and v_2 are the neutron velocities before and after scattering, respectively. The scattering of neutrons by the sample is described by the scattering function $S(q,\omega)$ quantifying the probability that a neutron is scattered by the sample with a momentum transfer q and an energy transfer ω (both are usually given in units of $\hbar$). For quasi-elastic scattering processes the energy transfer ω is small compared to the energy of the incident neutrons. We assume an energy transfer distribution, which is symmetrically distributed around $\omega = 0$. Then, the averaged neutron velocity after scattering v_2 equals the averaged neutron velocity before scattering v_1. Regarding equation (5) with respect to $v_1 = v_2$ the spin echo point can still be found for $L_1B_1 = L_2B_2 = BL$.
The energy transfer on the sample given by the energy difference between incoming and outgoing neutrons is:

$$\hbar\omega = E_{out} - E_{in} = \frac{1}{2}mv_1^2 - \frac{1}{2}mv_2^2 \tag{6}$$

For small velocity changes $dv = (v_1 - v_2) << v_1$ equation (5) can be written as:

$$\varphi(v) = \gamma BL\left(\frac{1}{v_1} - \frac{1}{v_2}\right) = \gamma BL\left(\frac{1}{v_1} - \frac{1}{v_1 + dv}\right) \approx \gamma BL\frac{dv}{v_1^2}. \tag{7}$$

Equation (6) then gives:

$$\hbar\omega = \frac{1}{2}m(v_1 + dv)^2 - \frac{1}{2}mv_1^2 \approx mv_1 dv. \tag{8}$$

Note that we assume identical field integrals in both spectrometer arms, that means: all formula assume that measurements are performed at the spin echo point. Combining equations (7 and 8) leads to:

$$\varphi = \frac{\gamma\hbar}{m}\frac{BL}{v_1^3}\omega \equiv \tau\omega \tag{9}$$

where the *spin echo time* τ is the proportionality constant between energy transfer and spin phase.

Equation (10) describes the basic principle of NSE data evaluation. The energy transfer due to scattering is measured directly by the spin phase φ of the neutron. The energy transfer may be quite small, but is still detectable at large spin echo times. Thus, the energy resolution increases with increasing spin echo time according to equation (9).
The final NSE signal P_{NSE} measured in an NSE experiment, using equations (3 and 5), is given by

$$P_{NSE} = \frac{\int d\omega S(q,\omega)\cos(\tau\omega)}{\int d\omega S(q,\omega)} = \frac{S(q,\tau)}{S(q,\tau = 0)} \tag{10}$$

In this expression, a normalization is applied to account for possible changes of the neutron polarization by the scattering process itself. Equation (10) shows that the NSE signal P_{NSE} is proportional to the cosine fourier transformation of the scattering function $S(q,\omega)$. In order to obtain full information about $S(q,\omega)$, P_{NSE} has to be measured at several values of τ. In general, quasi-elastic processes lead to a decrease of polarization.
We note here that, in practice, the determination of the polarization in the spin echo point is accomplished by slight variation of the field integrals B_1 and B_2 and fitting of an appropriate theoretical expression to the measured values.

2.3 Example

Imagine moving particles inside a liquid sample. Each scattered neutron loses or gains energy through the interaction with such a particle. This will result in different velocities for the incoming and outgoing neutrons. The strength of the NSE technique is to detect small energy changes of individual neutrons. To illustrate this fact, imagine a velocity distribution symmetric around the mean velocity v_1, with only two kinds of neutrons namely one sort with speed $v_1 - \Delta v$ and a second sort with speed $v_1 + \Delta v$ with $\Delta v < v_1$ representing an arbitrary momentum transfer. If we now have a sample inside of which the first sort is scattered with the probability of 100 % into the other sort and vice versa, the measured polarization at the end of the spectrometer will differ from 1, since only the wrong number of precessions for each neutron takes place. The first sort is too fast and the second one too slow to precess back to the initial position.
Our assumption will be that $S(q,\omega)$ corresponds to a Lorentzian line

$$S(q,\omega) = \frac{\Gamma}{\Gamma^2 + \omega^2} \tag{11}$$

which then, using equation (10), gives for the measured polarization signal an exponential decay :

$$P_{NSE} = \langle \cos\varphi \rangle = e^{-\Gamma\tau} \equiv e^{-\tau/\tau_0} \tag{12}$$

From the τ dependence of $P_{NSE}(\tau)$ it is possible to determine the linewidth parameter Γ of the scattering process and its lifetime $\tau_0 = \Gamma^{-1}$.

3 Neutron Resonance Spin Echo

3.1 NRSE coils

In the Neutron Resonance Spin Echo (NRSE) method each precession coil of NSE is replaced by a setup of two so-called *neutron resonance spin flipper coils* (NRSE coils) and the field free space in between. Each of the two NRSE coils is actually housing two different coils. The outer coil ("B_0 coil") creates a static magnetic field B_z in z-direction. The second coil inserted in the B_0 coil creates a rotating magnetic field B_{rf} and is called

rf coil. B_{rf} points perpendicular to B_z and rotates in the x-y-plane (around B_z) with the frequency ω_{rf}.
The neutrons entering the B_0 coil start to precess with the Larmor frequency $\omega_{Lar} = \gamma B_z$. The frequency of the rf coil is adjusted to be in resonance with ω_{Lar} (being the origin of the name NRSE):

$$\omega_{rf} \equiv \omega_{Lar}. \tag{14}$$

In addition to its precession around B_z, the neutrons precess around B_{rf} as soon as they enter the rf coil. This additional motion with frequency ω_R is called *Rabi oscillation* (figure 4). After a flight time of t and a precession of $\pi = \omega_R \cdot t$, the neutrons leave the magnetic field of the coil. By this, the spin of the neutrons is flipped with respect to the field direction of B_{rf}. This is the so-called *resonant π-flip*.
After the field free flight path the neutron enters the second NRSE coil (directions of both magnetic B_z fields are identical) and the neutrons´ spin performs a second resonant π-flip.

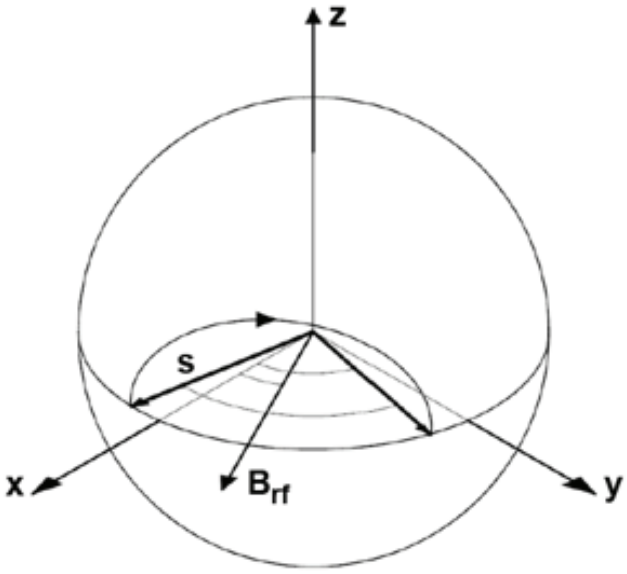

Figure 4: The spin *s* is initially in the x-y plane. As we consider the situation in the Larmor rotating coordinate system, the spin rests without the presence of a rf field. If we add the rotating field B_{rf}, with rotating frequency being in resonance with the Larmor frequency, this field in the rotating coordinate system and the spin precesses with the Rabi frequency around B_{rf}. After a half-twist, it is back in the x y plane, mirrored at B_{rf}.

The naming π-flip becomes clear when the case is considered, where the initial spin direction is parallel to B_z. In this case, the opening angle of the Larmor precession around B_z is zero. However, the precession with respect to B_{rf} takes place as discussed above. The angle between spin and B_{rf} is now exactly $\pi/2 = 90°$, and the spin performs a rotation by $\pi = 180°$ around the axis given by the B_{rf} field. This corresponds just to a

spin flip from up to down or vice versa (with respect to B_z) clarifying the origin of the naming „π-flip“.

3.2 NRSE signal and setup

A combination of two resonant spin flips as used in NRSE, results in the same final neutron spin phase as one single NSE precession region (figure 5), assuming double magnitude of the NSE field compared to B_z: $B = 2 \cdot B_z$. Hereby, the NSE coil length L is assumed to equal the distance of the NRSE coils.
The phase angle accumulated by the rotating field B_{rf} during the time $t=L/v$ the neutron spends between the two coils is $\varphi = \omega_{rf} t$. The total spin phase gained after the neutron passes through two NRSE coils, separated by the distance L, is $\varphi_{neutron} = 2\varphi$ as shown in figure 5.

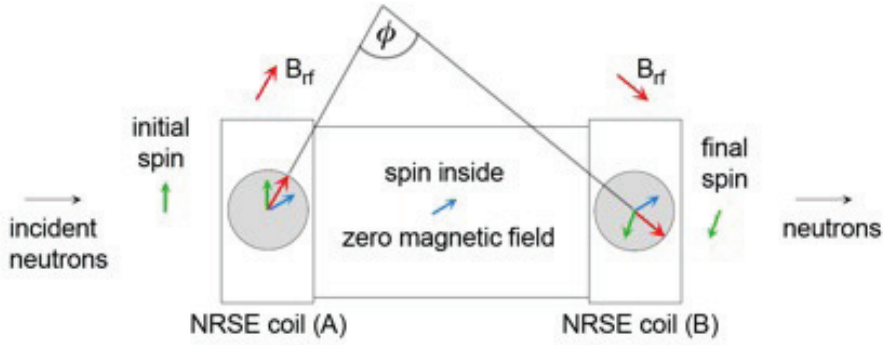

Figure 5: Schematic of two NRSE coils at distance L, which replace one NSE precession coil. The rotating field B_{rf} is in resonance to the static field B_z (B_z is not visible in the figure, as it points out of the plane of drawing). $\phi = \omega_{rf} t$ is the phase angle accumulated by the rotating field B_{rf} during the time $t=L/v$ the neutron spends between the two coils. The total spin phase gained after the neutron passes through both coils is $\phi_{neutron} = 2\phi$. Note the analogy to classical spin echo: $\phi_{neutron}$ is equivalent to the spin phase accumulated in a coil with length L and the static magnetic field $B = 2 \cdot B_z$.

A complete NRSE setup consists, consequently, of four NRSE coils, two in each spectrometer arm, with the flight paths in-between (figure 6).

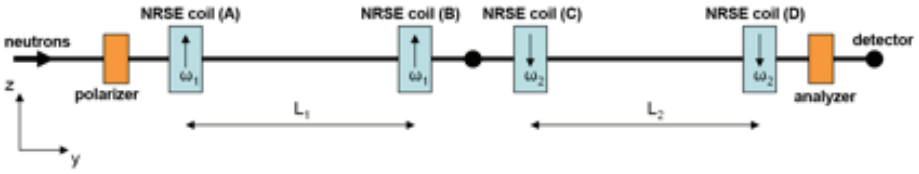

Figure 6: Schematic setup of a complete NRSE setup consisting of four NRSE coils, two in each spectrometer arm in front of and behind the sample. The static magnetic fields B_z are directed in the same direction in the same spectrometer arm, but in opposite direction with respect to the two arms. As in NSE, a NRSE setup is completed by a polariser in front of the precession regions, and a spin analyser placed behind the second precession region.

4 RESEDA

4.1 The instrumental setup

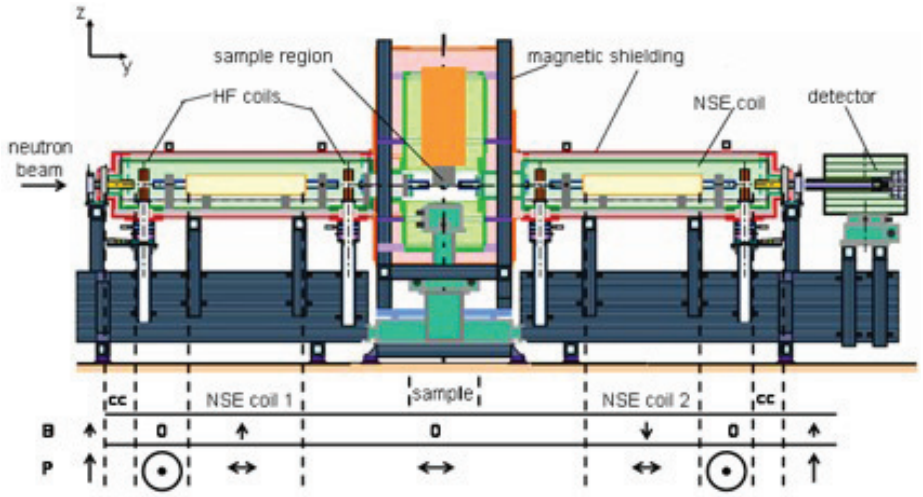

Figure 7: Schematic figure of the NSE spectrometer RESEDA with directions of polarization and magnetic fields without sample.

RESEDA (figure 7) accesses a high flux of cold neutrons (the cold source operates at 25 K) as it is installed at the neutron guide NL 5a in the neutron guide hall of the high flux reactor FRM II. RESEDA is a neutron spin echo spectrometer with two secondary spectrometer arms, in order to double the solid angle of detectable neutrons. The arms are enumerated as 0 (one incoming beam) and 1 and 2 (two scattered beams). In front of the magnetic coils, the beam preparation is accomplished, i.e. the neutron wavelength is selected. The velocity selector makes it possible to vary the wavelength used for experiments. The beam is spin polarized by a V-cavity polariser (selector and polariser not shown in figure 7).

RESEDA operates in the NSE mode for small spin echo times $\tau < 200$ ps and in the NRSE mode for large spin echo times $\tau > 200$ ps. In the following, we focus on the components of RESEDA being different to standard instruments: the magnetic fields and precession devices. The polarization of the neutron beam changes as follows from left to right through the different NSE coils (in figure 7, the resulting spin directions are illustrated below the instrument setup):

- Before coils: beam is polarized in z-direction
- 1st coupling coil (arm 0): changes the polarization to the x-direction
- 1st precession coil (arm 0): distributes the spins in the x-y-plane
- sample scattering: no change (except sample effects)
- 2nd precession coil (arm 1 or 2): back precession of the distribution in the x-y-plane
- 2nd coupling coil (arm 1 or 2): changes the polarization from x-direction to z-direction
- Analyzer and detector: determination of the polarization with respect to the z-direction

The neutrons are counted in ^{3}He detectors. RESEDA uses four points of an echo group to analyze the polarization. These four points are separated by a $\pi/2$-rotation of the spin phase. The measured signals do not necessarily correspond to the exact maximum or minimum of the amplitude. Nevertheless this method allows to obtain the polarization in a short measurement time with good statistics and without knowing the exact phase of the neutron spin.
The measurements of the phase of the neutron spin may be disturbed by external magnetic stray fields. Therefore, the spectrometer arms and sample region of RESEDA is surrounded by a double Mu-metal shielding (very high permeability of $\mu_r \gg 10000$) which compensates small stray fields.

4.2 The samples under study

At RESEDA, quasi-elastic dynamics in the spin echo time range 1.5 ps to 2 ns is routinely studied. In the laboratory course, two samples will be used. A standard elastically scattering sample is used to verify the operation of the instrument, and, in particular, to check the polarization of the spin rotation signal and the spin echo signal. The quasi-elastic measurements are performed on a magnetically scattering sample which exhibits helical magnetic ordering (figure 8) below the temperature of 28.5 K. The quasi-elastic dynamics are studied slightly above this temperature.

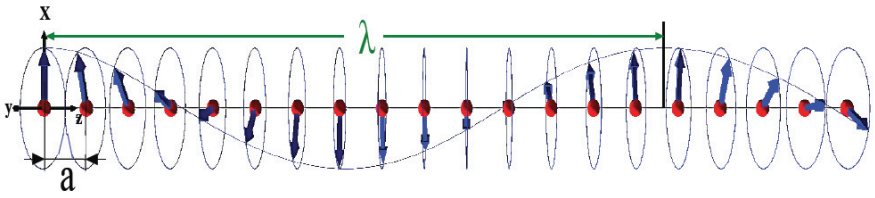

Figure 8: Schematic magnetic ordering structure of MnSi below 28.5 K. The spins form a helix with wavelength λ (therefore the name „helical phase“). a is the lattice spacing of the MnSi crystal.

5 Preparatory Exercises

1. Read this instruction carefully.
2. Calculate the energy and velocity of the neutrons accessible at RESEDA (cold source!). Calculate the time the neutrons need to pass the spectrometer arms (total length 8 m).
3. Look up the typical value of the earth‘s magnetic field. Calculate the precession frequency of the neutron spin in this field (gyromagnetic ratio!). Conclude with 2. on the spin phase accumulated at RESEDA, if there was no mu-metal shielding.

4. Understand the function of the instrumental set up and the NSE- and NRSE-method. What is the so-called „rotating wave approximation“?
5. Calculate the envelope of a spin rotation and spin echo group. Assume a Gaussian wavelength distribution of 13% width (FWHM) provided by the selector. Are the envelopes equal? If yes, why?
6. Calculate the spin phase $\varphi_1(v)$ assuming BL = 100 Gm (neutron wavelength 5 Å). Calculate the final spin phase $\varphi(v)$, if the neutron is scattered inelastically with an energy transfer of 0.01 meV. Discuss the sign of the energy transfer given in equation (6).
7. Calculate the polarization in the case of quasielastic scattering with $S(q,\omega)$ given by a Lorentzian function with line width Γ = 0.01 meV (neutron wavelength 5 Å).
8. Look up the nuclear and magnetic structure of MnSi. Which q-value corresponds to the largest magnetic structure? At which scattering angle are neutrons detected, when being scattered with this q-value (neutron wavelength 5 Å).
9. Which dynamics are detected in the experiment with MnSi temperature fixed to T=29 K? Plot the expected $S(q,\omega)$ curve.

6 Experiment Procedure

6.1 The experiment itself

You will have a guided tour on the instrument. You watch all components with the tutor, especially the precession devices.

You follow the tutor fixing the sample container at the sample stick and putting it to the sample position.

The experiment involves the following preparations:

•Sample assembly and alignment
•Cooling down the cryostat and verification of the temperature control.
•Check of the instrument set up (slits, cryostat, measurement angles, wavelength etc.)
•At low temperature, search for the magnetic peak of MnSi
•Resolution measurement at the lowest temperature
•Analysis and interpretation of data

The quasi-elastic data are acquired by means of a scan over night. The length and number of measurements will have to be adjusted to the available time, it may be necessary to use some measurements of the preceding groups.

Questions are welcome...!

Contact

RESEDA

Phone: 089/289-14874
Web: http://www.frm2.tum.de/wissenschaftliche-nutzung/spektrometrie/reseda/index.html

Wolfgang Häußler

Forschungsneutronenquelle Heinz Maier-Leibnitz (FRM II)
und Physik Department E21
Technische Universität München
Phone: 089/289-14921
e-Mail: Wolfgang.Haeussler@frm2.tum.de

TREFF

Reflectometer

S. Mattauch and U. Rücker

Jülich Centre for Neutron Science
Forschungszentrum Jülich

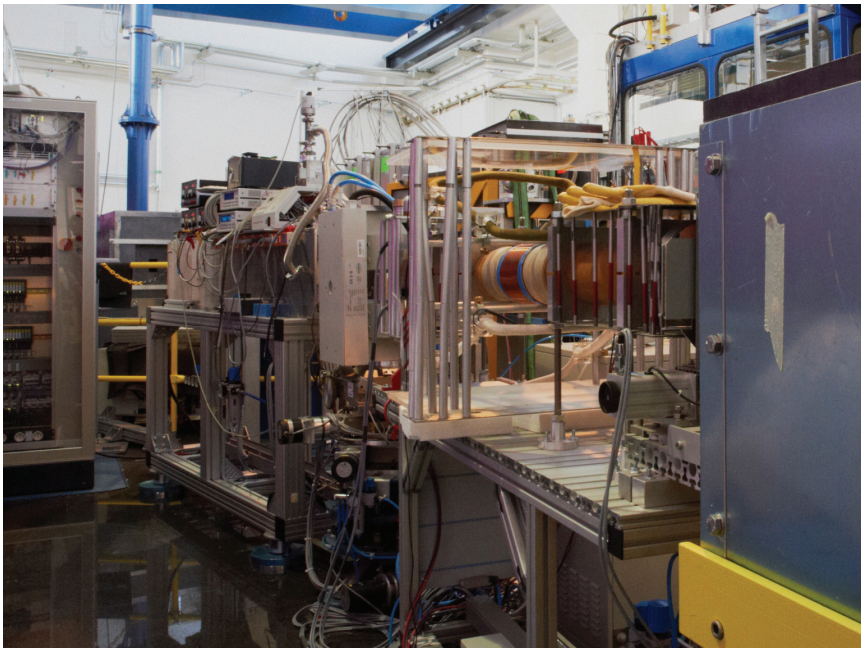

Manual of the JCNS Laboratory Course Neutron Scattering

Contents

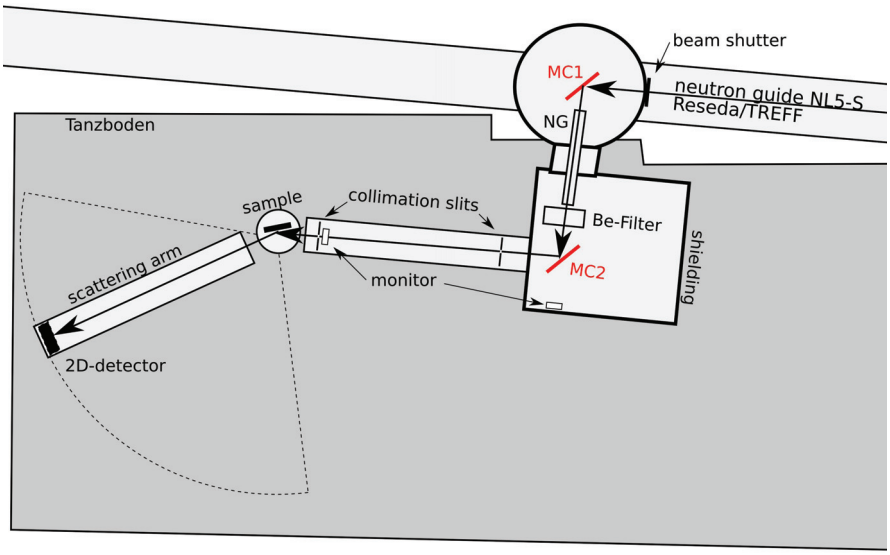

Fig. 1: *Sketch of the reflectometer TREFF@NOSPEC in top view.*

1 Introduction

The neutron reflectometry TREFF@NOSPEC at the neutron guide NL5-S is part of the neutron guide laboratory at the research reactor FRM II in Garching. TREFF is a joint facility of JCNS and the neutron optics group of FRM II. It is used for the investigation of magnetic layered structures as well as neutron optical components for the installation and improvement of neutron scattering instruments.

Figure 1 depicts the neutron reflectometer TREFF in the neutron guide hall of the FRM II research reactor. Essentially, it consists out of a double monochromator, the collimation path, the sample table with several stages of translation and rotation and, finally, the scattering arm with a position sensitive detector. The distance between the collimation slits is 1820mm and 450mm between the second slit and the centre of rotation of the sample table. For this experiment the wavelength is set to λ=4.73 Å.

2 Preparatory Exercises

The following questions will be asked during the practical course at TREFF:

1. In the sketch (Figure 1 of the instrument you will find a Be-filter and a NG (neutron guide) between the MC1 and MC2. What are they used for?

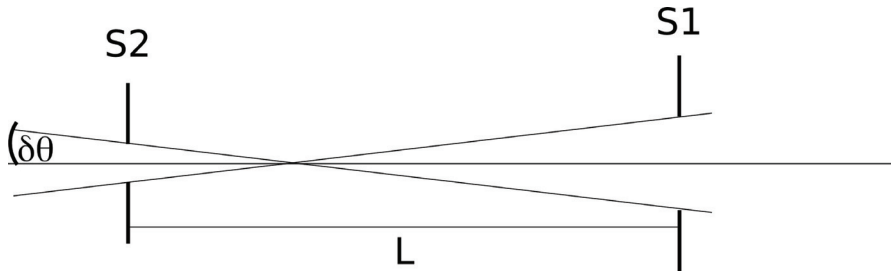

Fig. 2: *This drawing should help you to solve question 5.*

2. In the introduction the used wavelength was given with λ=4.73 Å. Which other wavelength are possible and how do you achieve these?
3. Depict a reflectivity curve of a substrate only
4. Depict a reflectivity curve of a substrate plus a layer
5. Calculate the divergence of a beam passing two slits S1 and S2 in a distance of L (see Figure 2)
6. Calculate the angle of collimation of the neutron beam to sufficiently resolve reflectivity oscillations of a 80nm thick monolayer on a substrate. What slit sizes follow for this reflectometer

3 Experiment Procedure

The aim of this experiment is the investigation of a nickel monolayer deposited on a glass substrate with unknown composition. Using neutron reflectometry the thickness of the nickel layer should be determined.

1. Perform a reflectivity experiment on the sample's back side and analyse the critical angle. To get sufficient collimation of the neutron beam, 0.6mm slit size for S1 and S2 should be taken.
2. Take the reflectivity curve of the Ni-monolayer system with the suitable collimation angles, so speaking the slit size for S1 and S2 calculated in the section before
3. Do like 3) but with a slit size of 3mm for S1 and S2.

3.1 The experiment itself

We (in the end it will be you) will mount the sample on the sample table and pre-align it with an appropriate tool (what could it be) parallel to the neutron beam. After some alignment scans

with the neutron beam we will measure the reflectivity curve step by step of the sample (see chapter Experiment Procedure).

3.2 Data reduction

The instrument saves the number of counts as a function of scattering angle.

3.3 Data evaluation

For systems such as multilayers the scattered intensity is determined by the difference in the potential of each layer (contrast). The potential is given by the **scattering length density** $\rho_{sld} = \sum_j b_j \rho_j$ with the scattering lengths b_j and the particle number densities ρ_j. The index j runs over all kind of atoms of the layer. The scattering length density is comparable to the optical density in light optics.
The **refraction index** of each layer is given by

$$n \gg 1 - \frac{\lambda^2}{2\pi}\rho_{sld} = 1 - \delta$$

.
With the **angle of total external reflection** $\Theta_c \sim \sqrt{2\delta}$, which is usually small, it follows

$$k_{c,z} = k\sin(q_c) \gg kq_c = \frac{2\pi}{\lambda}\sqrt{2\frac{\lambda^2}{2\pi}\rho_{sld}} = \sqrt{4\pi\rho_{sld}}$$

for the **critical wave vector**. For a monolayer system the **reflected amplitude** of each interface $r_{f,1}$ and $r_{f,2}$ can be calculated by the Fresnel formulae (Equation 16 in chapter 12 of the lectures book).
Neglecting roughness at the sample surface and at the interface between layer and substrate, for the amplitude at the surface one gets

$$r_{f,1} = \frac{k_{z,vac} - k_{z,lay}}{k_{z,vac} + k_{z,lay}} \quad \text{and at the interface} \quad r_{f,2} = \frac{k_{z,lay} - k_{z,sub}}{k_{z,lay} + k_{z,sub}}$$

with

$$k_{z,vac} = k\sin(q) \quad , \quad k_{z,lay} = \sqrt{k_{z,vac}^2 - 4\pi\rho_{sld,lay}} \quad \text{and} \quad k_{z,sub} = \sqrt{k_{z,vac}^2 - 4\pi\rho_{sld,sub}}$$

.
The superposition of both amplitudes yields the reflected amplitude of a monolayer sample

$$R = [r_{f,1} + r_{f,2}\exp(2ik_{z,lay}d)]\,\frac{\exp(-2ik_{z,vac}d)}{[1 + r_{f,1}r_{f,2}\exp(2ik_{z,lay}d)]}$$

with the film thickness d. The **reflected intensity** is given by re mean square of R. For $k_{z,vac} > 3k_{c,z}$ the intensity can be calculated in **Born approximation** by

$$|R|^2 \gg \frac{\pi^2}{k_{z,vac}^4}\left[\rho_{sld,lay}^2 + (\rho_{sld,lay} - \rho_{sld,sub})^2 + 2\rho_{sld,lay}(\rho_{sld,lay} - \rho_{sld,sub})\cos(2k_{z,vac}d)\right]$$

4 Experiment-Related Exercises

1. calculate from the reflectivity curve of the glass substrate the scattering length density $\rho_{sld,sub}$
2. Describe the differences and explain them between the measurement of the Ni monolayer with the 3mm slit and the slit size you have calculated.
3. Calculate the scattering length density $\rho_{sld,sub}$ of the Ni monolayer using:

molar volume	V_{Ni}=6.59 cm^3 mol^{-1}
Avogadro number	N_L=6.02 10^{23} mol^{-1}
coherent scattering length	b_{Ni}=10.3 fm

4. Determination of the thickness d of the Ni monolayer using the reflectivity formula in Born approximation. At first, estimate d based on the distance of the fringes of the reflectivity (see Data evaluation chapter).

References

Your lecture book of the year

Contact

TREFF
Phone: 089/289-10768
Web:

Stefan Mattauch

JCNS
Forschungszentrum Jülich GmbH

Phone: 089/289-10709
e-Mail: s.mattauch@fz-juelich.de

Denis Korolkov

Phone: 089/289-10722
e-Mail: d.korolkov@fz-juelich.de

Andreas Ofner

Neutronenoptik Gruppe
Forschungsneutronenquelle Heinz Maier-Leibnitz (FRM II)

Phone: 089/289-14677
e-Mail: andreas.ofner@tum.de

TOFTOF

Time-of-flight spectrometer

S. Busch, H. Morhenn, G. G. Simeoni, W. Lohstroh,
and T. Unruh

Forschungsneutronenquelle Heinz Maier-Leibnitz (FRM II)
Technische Universität München

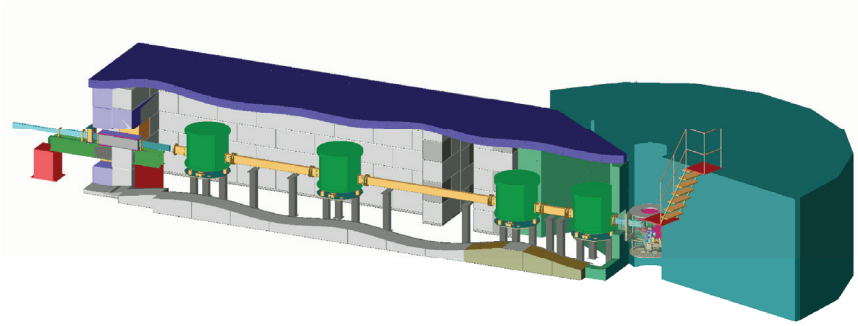

Manual of the JCNS Laboratory Course Neutron Scattering

Contents

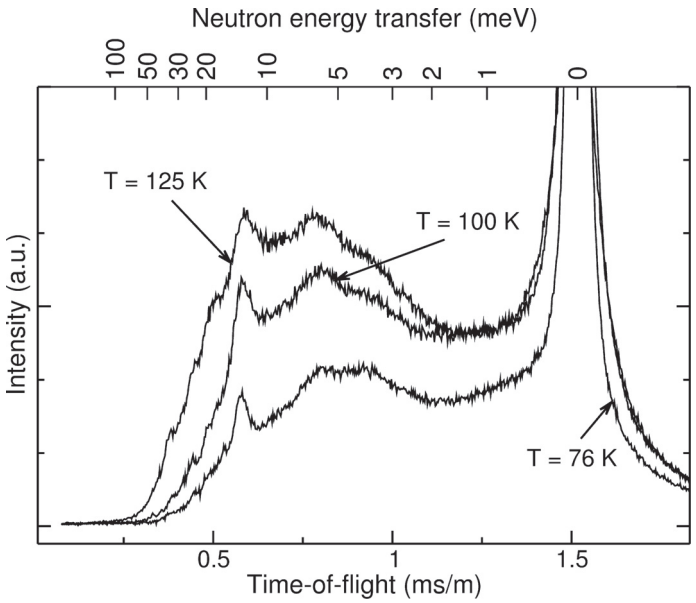

Fig. 1: *Neutron time-of-flight spectrum of pentafluorotoluene, taken from [4]. Elastic scattering happens at energy transfer zero, quasielastic scattering in a region of approximately* 0 ± 1 *meV, inelastic scattering at larger energy transfers.*

1 Introduction

Scattering experiments are carried out in order to obtain information about the structure and dynamics of the studied systems (e. g. crystals, liquids, nanoparticles). Optical microscopes are simpler to understand and operate but their resolution is limited by the wavelength of light. There are only few techniques which give access to the length scale of molecules and atoms. Of those, one of the most important is scattering.

There are several kinds of scattering experiments, depending on the subject matter. In this experiment we want to introduce you to *quasielastic neutron scattering* (QENS). Quasielastic scattering is referring to a broadening of the elastic line in a spectrum. The extend of this broadening is approximately 1 meV. Whereas in inelastic scattering (which will not be further discussed in this experiment), discrete maxima or bands appear clearly separated from the elastic line. While one can gain information about the structure or periodic motions (i. e. phonons) of the sample using *diffraction* or *inelastic scattering*, respectively, it is possible to analyse non-periodic motions (e. g. diffusion) with quasielastic scattering.

Prior to the experiment, you should read and understand these instructions, since you won't have much time to do so during the experiment. Along with this you should also work out the question section. In the following, we will first follow the path of the neutrons from the source over the sample to the detector. Afterwards, the theory of scattering will be roughly introduced, so that one can understand which information can be obtained from the scattered neutrons. Thereon the specific experiment will be explained.

To carry out the experiment, you should bring this introduction, your answers to the questions, paper and a pen. After having started the measurement of the reference sample, we will show you the spectrometer TOFTOF. Afterwards we will prepare a sample, which we then will measure. Finally, we will evaluate the data together.

2 Basics

2.1 The neutron source FRM II

In general there are two techniques in order to "produce" neutrons – spallation and nuclear fission. During spallation, huge nuclei (e. g. lead) are bombarded with protons, subsequently split and, among others, emit neutrons. The FRM II is a nuclear reactor used as a neutron source. Here ^{235}U captures a thermal neutron and thereby becomes unstable. The nucleus fissures and, among others, emits three fast neutrons.

These fast neutrons must be slowed down (moderated) to thermal energies, that is room temperature, in order to initiate a new fission. The moderated neutrons are further needed for the neutron scattering experiments. The moderation occurs in D_2O of about 300 K which encloses the core.

In order to further slow down the neutrons, and thereby match their energies to the ones of atomic motions, a tank containing liquid D_2 at 25 K is located close to the fuel element. From this *cold source* several neutron guides lead the neutrons to the instuments. Inside these guides, the neutrons are transported by total reflection at the outer walls. The time of flight spectrometer TOFTOF is located at the end of neutron guide 2a in the neutron guide hall.

2.2 The time-of-flight spectrometer TOFTOF

The *cold neutrons* move with a velocity of several hundred m/s. Hence one can determine the kinetic energy of the neutrons comfortably by a time of flight (TOF) measurement along a certain distance. If one sets the initial energy of the neutrons before the scattering event to a well-known value and measures the final energy (or velocity) after the scattering process, the energy transfer can be determined. Since the position of the detectors is fixed, the scattering angle is also known.

During time of flight spectroscopy the energy transfer is measured by a time of flight measurement of the neutrons. The advantage of the time of flight technique is that a huge range of momentum and energy transfer can be captured simultaneously.

TOFTOF is a multi chopper time of flight spectrometer with direct geometry [5]. This means that all neutrons have (more or less) the same energy before interacting with the sample. After being scattered by the sample, the energy transfer can be determined. Both, the tuning of the energy of the incident neutrons (their wavelength) and the determination of the energy of the scattered neutrons is done by time of flight.

The neutrons are directed to the spectrometer through a neutron guide, which has a supermirror coating. The end of the guide is double focusing.

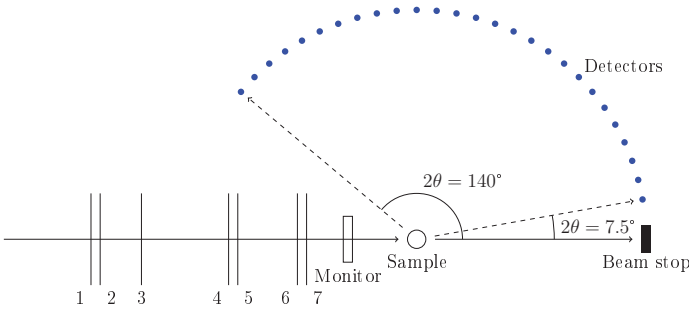

Fig. 2: *Schematic drawing of TOFTOF. Following the neutron guide, first are choppers 1 & 2 which work together with 6 & 7 as velocity selector. Choppers 3 & 4 remove higher orders, 5 is the frame overlap chopper. The time needed for the neutrons to get from the sample to the detectors encodes their energy.*

The primary spectrometer consists of seven rotating chopper discs which are placed in evacuated vessels (colored green on the cover page). The discs are made of carbon fibre composites and are coated with neutron-absorbing boron. On opposing sides, slits have been manufactured into the discs through which neutrons can pass. The first and last pair of choppers rotate in opposite direction each.

The incoming white neutron beam is pulsed by the first pair of choppers (pulsing choppers). The short neutron pulse consists of fast and slow neutrons. Thus the pulse spreads along the way to the last chopper pair. These last two choppers (monochromating choppers) select a narrow range of wavelengths out of the pulse. The third and fourth chopper filter out higher orders (higher order removal choppers).

The fifth chopper is the frame overlap chopper. After the scattering process some neutrons fly towards the detectors. It is essential that all scattered neutrons of one pulse are detected before the neutrons from the next pulse arrive. The overlap of slow neutrons from a pulse with fast neutrons of the following pulse inside the secondary spectrometer is called frame overlap. The frame-overlap-chopper blocks out several pulses, in order to avoid such an overlap.

A good energy resolution can be achieved with a high rotational speed of the chopper discs (up to 16000 revolutions/minute). The energy resolution of the spectrometer can be changed continuously in the range from roughly 5 μeV to 5 meV (Fig. 3). By defining the energy uncertainty one can modify the time of observation in the range from roughly 1 ps to 1 ns.

The intensity of the incident neutron beam is recorded with a monitor, which is located between the primary spectrometer and the sample. A ionization chamber is used as a monitor, filled with fissile matter (^{235}U). The incoming neutrons trigger a fission and the high-energy nuclear fission products generate a clear voltage pulse, due to their high ionization density.

After passing the monitor, the neutrons hit the sample. Most of the neutrons are transmitted and reach the beamstop, but about 10 % of the neutrons are scattered in all possible directions. Some neutrons move towards the detectors and enter the flight chamber, which occupies the space between the sample and detectors. The chamber is filled with argon in order to avoid unwanted scattering with air molecules.

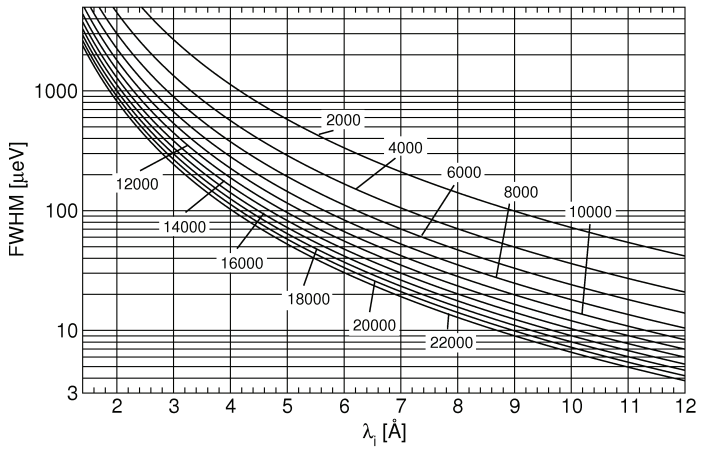

Fig. 3: *Calculated energy resolution of the TOFTOF spectrometer shown for several chopper rotation speeds as function of the initial neutron wavelength. The chopper rotation speeds are given in rounds per minute (rpm) [5].*

Altogether 1000 ^{3}He-detectors (40 cm long and 3 cm in diameter) are placed tangential to the Debye-Scherrer-circles and also tangential to an imaginary spherical surface with a radius of 4 m around the position of the sample. Thus the flightpath from the sample to the detectors is 4 m long. The scattering angle 2θ covers a region from 7.5° to 140°. The detection of the scattered neutrons inside the ^{3}He-detectors occurs via a (n,p)-reaction. Hereby the neutrons are registered and tagged with a time stamp. The amount of detected neutrons is saved in time of flight bins for each detector in raw data files.

3 Theory

3.1 Cross sections

The probability that a neutron is scattered by a nucleus is denoted by the scattering cross section σ. It depends on:

1. the element
2. the isotope
3. the relative spin orientation of neutron and nucleus

Imagine a single crystal. The scattering cross section of every nucleus i can be decomposed into $\overline{\sigma} \pm \Delta\sigma_i$ where $\overline{\sigma}$ is the average over the whole crystal. This averaged part of the scattering cross section is called the *coherent scattering cross section*: scattered neutrons which can be described by this part of the scattering cross section "see" a regular lattice and interfere to a regular scattering pattern.

nuclide / element	σ_{coh} (barn)	σ_{inc} (barn)	σ_{abs} (barn)
^{1}H	1.758	80.27	0.3326
^{2}H	5.592	2.05	0.0005
H	1.760	80.26	0.3326
C	5.551	0.001	0.0035
N	11.01	0.5	11.51
O	4.232	0.001	0.0002
F	4.017	0.001	0.0096
Al	1.495	0.01	0.231
P	3.307	0.005	0.172
V	0.02	5.08	5.08

Table 1: *Coherent and incoherent scattering cross sections as well as absorption cross sections of some selected nuclei or elements in their natural isotope composition, 1 barn = 100 fm^2. Source: [2].*

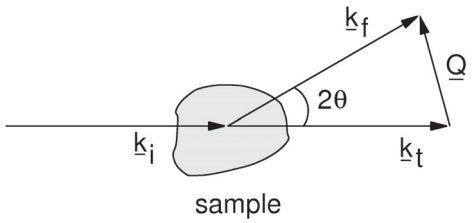

Fig. 4: *Schematic representation of a scattering experiment.* $\mathbf{k}_{i,f,t}$ *are the wave vectors of the initial (incoming), final (scattered) and transmitted neutrons, respectively.* $\mathbf{Q}$ *is the scattering vector.*

In contrast, the $\Delta\sigma$ are distributed randomly throughout the crystal and the scattering of the neutrons which can be described by the $\Delta\sigma$ does not interfere to a special pattern. This effect is attributed to an artificial quantity, the *incoherent scattering cross section*.

The proton (^{1}H) has the biggest incoherent cross section of all nuclei we study normally (about 80 barn, cf. Tab. 1). For practical purposes, the big difference between the incoherent scattering cross section of the proton and the deuteron (^{2}H) is of enormous importance. Using isotope exchange, i. e. (partial) deuteration of molecules, specific parts of the sample can be masked.

Vanadium scatters at the employed wavelengths also mainly incoherently although not as strong as the proton.

3.2 Principle of a scattering experiment

At a scattering experiment, two important values are recorded (cf. Fig. 4):

- The scattering vector $\mathbf{Q}$ is defined as the difference between the wave vector $\mathbf{k}_f$ of the

scattered wave (f as "final") and the wave vektor $\mathbf{k}_i$ of the incident wave (i as "initial"). The momentum gained or lost during the scattering process can be calculated by

$$\Delta\mathbf{p} = \hbar\mathbf{Q} = \hbar(\mathbf{k}_f - \mathbf{k}_i) \; . \tag{1}$$

However, the momentum transfer is commonly not noted. Instead, the scattering vector is commonly stated in units of inverse Ångstrom.

- The energy transfer ΔE is defined as the energy of the neutron after E_f and before E_i the scattering process:

$$\Delta E = \hbar\omega = \hbar(\omega_f - \omega_i) = \frac{\hbar^2(|\mathbf{k}_f|^2 - |\mathbf{k}_i|^2)}{2m_n} \; . \tag{2}$$

The energy transfer is measured in meV. Often, ω is written incorrectly instead of $\hbar\omega$.

The absolute value of the wave vectors $\mathbf{k}$ is defined as $|\mathbf{k}| = 2\pi/\lambda$, with an refractive index $n \approx 1$ (which is a very good approximation for neutrons). However, the scattering vector cannot be measured directly, only the wave vector of the incident and scattered neutrons. Using the law of cosine one obtains a general equation for converting k_i and k_f to Q:

$$|\mathbf{Q}|^2 = |\mathbf{k}_i|^2 + |\mathbf{k}_f|^2 - 2|\mathbf{k}_i||\mathbf{k}_f|\cos(2\theta) \; . \tag{3}$$

In the case of elastic scattering, the energy transfer is zero. Hence $|\mathbf{k}_i| = |\mathbf{k}_f|$ simplifies the equation to

$$Q = \frac{4\pi}{\lambda}\sin\left(\frac{2\theta}{2}\right) \tag{4}$$

where $Q = |\mathbf{Q}|$. Roughly speaking a distance d in direct space corresponds to a Q value

$$Q = \frac{2\pi}{d} \; . \tag{5}$$

Therefore one can extract information about the physical configuration of the nuclei in the sample by analysing the intensity of the elastic scattering as a function of Q (the diffractogram), cf. Fig. 6. Furthermore the intensity at a certain value of Q as a function of energy (a spectrum) provides information about the motion of the nuclei (see Fig. 6).

3.3 Correlation & scattering functions

The motions of the nuclei – and hence of the molecules – can be described using correlation functions. It can be shown that these correlation functions are what is measured with scattering methods.

The *pair correlation function* $G_{\text{pair}}(\mathbf{r}, t)$ gives the probability to find a particle j at time t at the place $\mathbf{r}$ if this or another particle i was at time $t = 0$ at the origin $\mathbf{r} = \mathbf{0}$, as shown in Fig. 5. The pair correlation function is

$$G_{\text{pair}}(\mathbf{r}, t) = \frac{1}{N}\sum_{i=1}^{N}\sum_{j=1}^{N}\int \langle\delta\{\tilde{\mathbf{r}} - \mathbf{R}_i(0)\}\cdot\delta\{\tilde{\mathbf{r}} + \mathbf{r} - \mathbf{R}_j(t)\}\rangle \, \mathrm{d}\tilde{\mathbf{r}} \; , \tag{6}$$

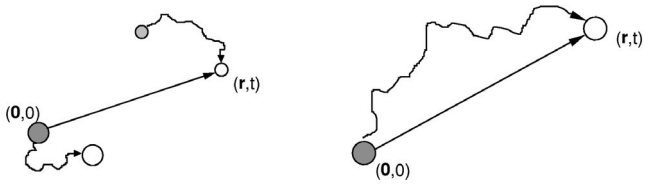

Fig. 5: *Left: Pair correlation, right: self correlation. In the case of pair correlation, the second particle may be a different one than the first one but it doesn't have to.*

with the number of particles N, an integration variable $\tilde{\mathbf{r}}$ and the place $\mathbf{R}_j(t)$ of particle j at time t. The angle brackets $\langle\rangle$ denote an ensemble average.

The *self correlation function* or *auto correlation function* $G_{\text{self}}(\mathbf{r}, t)$ gives the probability to find one particle at time t at place $\mathbf{r}$ if this very particle was at time $t = 0$ at the place $\mathbf{r} = \mathbf{0}$, see again Fig. 5. It is defined as

$$G_{\text{self}}(\mathbf{r}, t) = \frac{1}{N} \sum_{i=1}^{N} \int \langle \delta\{\tilde{\mathbf{r}} - \mathbf{R}_i(0)\} \cdot \delta\{\tilde{\mathbf{r}} + \mathbf{r} - \mathbf{R}_i(t)\} \rangle \, \mathrm{d}\tilde{\mathbf{r}} \, . \tag{7}$$

In the following, we will assume that the samples are powder samples (i. e. not single crystals, so for example liquids) and will therefore use the absolute value of $\mathbf{r}$, r, instead of the vector.

It is possible to calculate the pair and self correlation function from the scattered intensities. Roughly, the calculation is as follows:

Looking at the momentum and energy change of the neutrons during the scattering process, one obtains the *double differential scattering cross section* which can be seen as the sum of a coherent and an incoherent part:

$$\frac{\mathrm{d}^2\sigma}{\mathrm{d}\Omega \mathrm{d}E'} = \frac{k_f}{k_i} \frac{N}{4\pi} \big(\sigma_{\text{coh}} S_{\text{coh}}(Q, \omega) + \sigma_{\text{inc}} S_{\text{inc}}(Q, \omega) \big) \, . \tag{8}$$

It denotes the probability that a neutron is scattered into the solid angle $\mathrm{d}\Omega$ with an energy change $\mathrm{d}E'$. N is the number of scattering nuclei and $S(Q, \omega)$ is called the *scattering function*.

The Fourier transform in time and space of the coherent scattering function $S_{\text{coh}}(Q, \omega)$ is nothing but the pair correlation function $G_{\text{pair}}(r, t)$ and the Fourier transform in time and space of $S_{\text{inc}}(Q, \omega)$ is the self correlation function $G_{\text{self}}(r, t)$.

Three functions are important:

1. the *correlation function* $G(r, t)$
2. the *intermediate scattering function* $I(Q, t)$ which is the Fourier transform (from r to Q) of $G(r, t)$
3. the *scattering function* $S(Q, \omega)$ which is the Fourier transform (from t to ω) of $I(Q, t)$

All of them exist in two versions, considering pairs of particles (pair correlation function) or only one particle (self correlation function).

For the intermediate scattering function $I(Q,t)$ one can obtain further expressions – for a pair correlation

$$I_{\text{coh}}(Q,t) = \frac{1}{N}\sum_{i=1}^{N}\sum_{j=1}^{N}\left\langle \mathrm{e}^{-\mathrm{i}Qr_i(0)}\mathrm{e}^{\mathrm{i}Qr_j(t)}\right\rangle \tag{9}$$

and for the self correlation function

$$I_{\text{inc}}(Q,t) = \frac{1}{N}\sum_{i=1}^{N}\left\langle \mathrm{e}^{-\mathrm{i}Qr_i(0)}\mathrm{e}^{\mathrm{i}Qr_i(t)}\right\rangle \ . \tag{10}$$

At neutron spin echo spectrometers, the intermediate scattering function is measured – all other neutron scattering spectrometers, including TOFTOF, measure the scattering function.

If a scatterer performs several motions simultaneously (but independently from each other), the resulting incoherent scattering function is a convolution in energy space of the single scattering functions, for example

$$S_{\text{total}}(Q,\omega) = S_{\text{diffusion}}(Q,\omega) \otimes S_{\text{internal motion}}(Q,\omega) \ . \tag{11}$$

As a convolution corresponds to a multiplication after Fourier transform, one can also write

$$I_{\text{total}}(Q,t) = I_{\text{diffusion}}(Q,t) \cdot I_{\text{internal motion}}(Q,t) \ . \tag{12}$$

If two scatterers perform two motions independently from each other and both cause incoherent scattering, the recorded total incoherent scattering function is simply the sum of the two scattering functions, for example

$$S_{\text{total}}(Q,\omega) = S_{\text{solute}}(Q,\omega) + S_{\text{solvent}}(Q,\omega) \ , \tag{13}$$

which is also a sum after Fourier transform to the intermediate scattering function.

This decomposition of the scattering functions into parts is *very* important.

Due to the limited number of supporting points it is not possible to obtain the correlation function by numerical Fourier transform of the measured scattering function. Therefore, one proceeds the other way round: After inventing a plausible correlation function, one performs a Fourier transform of this theoretical function to a scattering function and checks if this can describe the data.

The hereby obtained theoretical scattering function $S_{\text{theor}}(Q,\omega)$ is fitted to the measured scattering function $S_{\text{meas}}(Q,\omega)$ after convolving the theoretical scattering function with the measured instrumental resolution. The instrumental resolution is often determined using a vanadium sample which is a static, incoherent scatterer.

4 Experiment

4.1 The system

In this experiment we will study the diffusive motions of molecules, mainly of *n*-alkanes.

Alkanes are rather simple chemical compounds, consisting only of carbon and hydrogen, which are linked together by single bonds. By analyzing this system we want to learn more about the mechanism of molecular self-diffusion.

As already mentioned, the observation time of the instrument can be modified in the pico- to nanosecond time scale. In this experiment, we want to probe the dynamics in this regime, therefore we will perform resolution resolved experiments at temperatures above the melting point. The main questions that we want to answer are: Can we observe long-time diffusion? How can we describe the dynamics that are faster than long-range diffusion?

4.2 Modelling the motions

Molecules in general are by far too complex to come up with a scattering function which describes all the motions correctly. Therefore, very simplified models are used. Assuming that the molecule itself is rigid and moves as a whole, one obtains the scattering function

$$S_{\text{diffusion}}(Q,\omega) = \frac{1}{\pi}\frac{|\Gamma_d(Q)|}{\omega^2 + \Gamma_d(Q)^2}\ , \tag{14}$$

a Lorentzian with a Q-dependent width $|\Gamma_d(Q)|$. If the diffusion follows exactly Fick's law, one obtains

$$|\Gamma_d(Q)| = \hbar D \cdot Q^2 \tag{15}$$

with the diffusion coefficient D which is normally given in m^2/s.

Is the line width too big at small Q, this can be a sign of *confinement*: the molecule cannot escape from a cage formed by the neighboring molecules. Is the line width too small at high Q, this can be a sign of *jump diffusion* which should rather be named *stop-and-go diffusion*: the molecule sits for some time at a certain place, then diffuses for a while, gets trapped again, ...

Try to fit the data with one Lorentzian. If this model does not describe the data satisfactorily, the assumption of a rigid molecule was probably not justified. In this case, also an internal motion has to be regarded – one localized motion corresponds to the scattering function

$$S_{\text{intern}}(Q,\omega) = A_0(Q)\cdot\delta(\omega) + (1 - A_0(Q))\cdot\frac{1}{\pi}\frac{|\Gamma_i|}{\omega^2 + \Gamma_i^2}\ , \tag{16}$$

that is the sum of a delta-function and a Lorentzian (confer also figure 6). While the Q-*in*dependent $|\Gamma_i|$ gives the frequency of the motion, the *elastic incoherent structure factor* EISF $A_0(Q)$ describes the geometry of the motion – in first approximation the size.

As we assume that the molecule performs a local motion and long-range diffusion simultaneously but independently from each other, we have to convolve the two functions with each other. The result is the sum of two Lorentzians:

$$S(Q,\omega) = F(Q)\cdot\left\{\frac{A_0(Q)}{\pi}\frac{|\Gamma_d(Q)|}{\omega^2 + \Gamma_d(Q)^2} + \frac{1 - A_0(Q)}{\pi}\frac{|\Gamma_d(Q)| + |\Gamma_i|}{\omega^2 + (|\Gamma_d(Q)| + |\Gamma_i|)^2}\right\}\ . \tag{17}$$

4.3 The experiment itself

We might either produce a sample together or fill an existing sample into the aluminium hollow cylindrical container or a flat aluminium container. This sample is then measured at TOFTOF with a vanadium standard and the empty aluminum container. The length and number of measurements will have to be adjusted to the available time, it will be necessary to use some measurements of the preceding groups.

You will do all sample changes in the presence of a tutor who explains the procedure in detail.

4.4 Data reduction

The instrument saves the number of counts as a function of scattering angle and time-of-flight, $N(2\theta, \mathrm{tof})$. The next step is the data reduction which applies several corrections and transforms to get rid of many instrument-specific properties of the data and convert them to a scattering function $S(Q, \omega)$.

Data reduction (and later on also data evaluation) is done with the program FRIDA [6]. Inside an X Terminal window, start FRIDA by entering `ida`. The question "Load file ?" has to be answered by simply pressing "Enter". You can get an overview of the available commands in FRIDA by entering `hc` or looking into the online manual [3].

As you can see there, the routine to load TOFTOF data is started with `rtof`. The values in square brackets are default values proposed by the program, they can be accepted by pressing "Enter". You can find all the commands you have to enter in the online manual – they make the program do the following:

While reading the raw data $N(2\theta, \mathrm{tof})$, all the given runs will be added up (which means that you will have to do this procedure for one sample temperature at a time) and normalized to the monitor counts. This is followed by the calculation of the energy transfer from the time-of-flight so that one obtains $S(2\theta, \omega)$. The time-of-flight when the neutrons arrive which were scattered elastically by the vanadium is set as energy transfer zero for each detector independently.

Now that the x-axis is energy transfer, FRIDA can correct for the neutron energy dependent efficiency of the detectors which was given by the manufacturer. Also the differences in sensitivity between the detectors will be corrected. To do that, all scattered intensities are normalized to the elastically scattered intensity of the vanadium standard. As vanadium is an incoherent scatterer, it should scatter the same intensity in all directions. The only effect which causes deviations from an isotropic scattering is the Debye-Waller-factor (DWF) which is well-known and can be corrected by the program as well.

4.5 Data evaluation

To get an impression how much coherent and incoherent scattering the sample produces and to check the existence of Bragg peaks, diffraction patterns have to be produced. To make diffraction patterns, stop here and extract the intensity at $\omega = 0$. Should you find Bragg peaks, delete all spectra which contain intensity from these peaks before continuing.

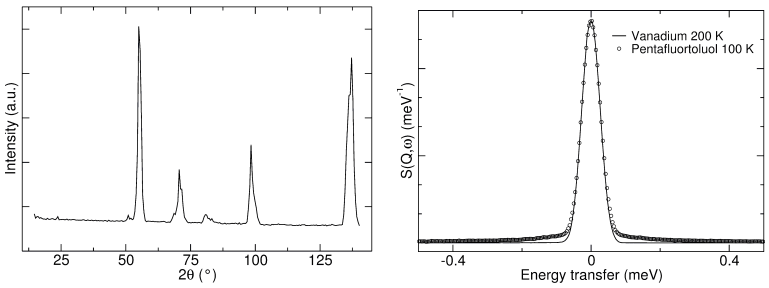

Fig. 6: *Left: Neutron diffraction patterns of solid pentafluortoluene at 100 K ($\lambda_i = 6\,\text{Å}$), taken from [4]. If the scattering vector is a reciprocal lattice vector, the positive interference of neutron waves yields a maximum in the scattered intensity. The sharp features in the diffraction pattern indicate an ordered lattice. Right: The spectra $S(Q,\omega)$ of pentafluortoluene (∘) and vanadium (–) at a momentum transfer of $Q = 1.1\,\text{Å}^{-1}$, cf. also [4]. The solid sample shows only an internal motion, can therefore be described by equation 16.*

To look at the dynamics, the next step is to calculate the momentum transfer Q from the scattering angle 2θ and the energy transfer ω using equation (3). During this step, we obtain about 1000 spectra with relatively low statistics each and a varying value of Q as the energy transfer varies. To get a better statistics and to have spectra which have the same Q for all values of energy transfer, the 1000 spectra are grouped into about 20 spectra of constant Q in the same routine.

These spectra $S(Q,\omega)$ contain information about sample and sample container. Therefore, the spectra of the empty sample container are subtracted. To do so, the same data reduction procedure has to be repeated with the empty container as "sample".

We want to use the spectra of vanadium as a measure of the instrumental resolution. This means that the whole procedure has to be done one more time with vanadium as "sample" (and as "vanadium").

Fit the spectra with the functions given in section 4.2, a single Lorentzian and a sum of Lorentzians. As the theoretical functions have to be convolved with the experimental resolution, the program will ask for the converted and grouped spectra of vanadium.

The numbers shown in brackets are the reduced χ^2 which is a measure for the quality of the fit, the other numbers are the fitted values of the parameters. Judge the fit quality by the reduced χ^2 and by visually inspecting the fits together with the data. Plot the parameters as a function of Q or Q^2 and determine the diffusion coefficient.

If you measured the sample at different temperatures, repeat the procedure for all of them.

5 Questions to be answered *before* the experiment

1. Do you expect the vanadium sample to be activated by the neutron beam? What about the aluminum container with the real sample? (2 min)

2. The vanadium standard sample at TOFTOF is a hollow cylinder with an outer diameter of 22.5 mm and a height of 65 mm. The wall thickness is 0.6 mm. Which fraction of the neutrons that hit the vanadium will be scattered? How big is the transmission?

3. Why do the samples measured at TOFTOF mostly have a transmission of about 90 %? How can the transmission be adjusted? (3 min)

4. The substance to be measured is filled in a gap between the inner and the outer cylinder of the sample container. The inner diameter of the outer cylinder is always 22.5 mm, the inner cylinder can be chosen to have either 22.1 mm or 22.3 mm outer diameter. The height of the cylinders is 65 mm. How large is the sample volume for the two different inner cylinders? Which inner cylinder would you use? (5 min)

5. Take a look into the FRIDA online manual [3]. Find the pages where it is explained how to read TOFTOF data and how to fit a model. (10 min)

6. Please note where this handout could need improvement. (5 min)

6 Questions to be answered *during* the experiment

During the experiment, we will divide the group for some time into two: One is evaluating the data at the computer while the other solves these problems. After some time, the two groups will switch.

1. When measuring water-based samples, H_2O is most often replaced by D_2O when the water is not the subject of the study. Why? The signal of the solvent has to be subtratced in both cases! (2 min)

2. Why is the sample container made of aluminum? (2 min)

3. The Vanadium standard sample at TOFTOF (hollow cylinder, 2 cm outer diameter, 0.6 mm thickness) is a "7% scatterer", meaning that it transmits 93% of the neutrons. In the moment, TOFTOF has 1000 neutron detectors with an active area of 40x3 cm each in 4 m distance from the sample. Estimate the efficiency of the monitor detector using the *Monitor rate* and *Signal Rate* given by the control program. (5 min)

4. To calculate the energy of neutrons in meV with a well-known wavelength given in Å, one can use a formula
$$E \approx \frac{a}{\lambda^2} \,. \tag{18}$$
Determine a numerical value for a. How big is the initial energy E_i of the neutrons in the current experiment? (5 min)

5. What is the maximal energy transfer from the neutron to the sample? (1 min)

6. What is the maximal energy transfer from the sample to the neutron? (1 min)

7. Draw at least six scattering triangles (as shown in Fig. 4) for these points in the dynamical range:

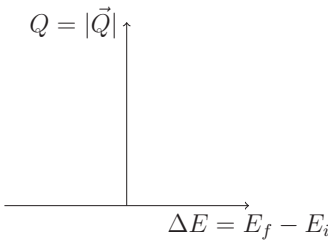

- Elastic scattering with a scattering angle of 7.5°; with a scattering angle of 140° (the first & last detector at TOFTOF)
- Same scattering angles with neutron energy gain
- Same scattering angles with neutron energy loss

(6 min)

8. Locate those points in this dynamic range plot:

   and determine which area in this plot is accessible in the current scattering experiment. (5 min)

9. How can you distinguish coherent and incoherent scattering in the diffraction pattern? Which information can you extract from the spectra when they are caused by coherent or incoherent scattering, respectively? (2 min)

10. Why do we measure Vanadium? (three reasons; for one it is important that Vanadium scatters neutrons incoherently, for two it is important that the Vanadium signal does not have a quasielastic broadening) (6 min)

11. Assume that the scatterers in your sample are partially trapped. They diffuse inside a "cage" until they find a hole through which they can escape. How do the intermediate scattering function $I(Q,t)$ and the scattering function $S(Q,\omega)$ look like? (5 min)

7 Constants

$$m_n = 1.675 \cdot 10^{-27}\,\mathrm{kg} \tag{19}$$

$$h = 6.626 \cdot 10^{-34}\,\mathrm{J}\cdot\,\mathrm{s} = 4.136 \cdot 10^{-15}\,\mathrm{eV}\cdot\,\mathrm{s} \tag{20}$$

$$\hbar = 1.055 \cdot 10^{-34}\,\mathrm{J}\cdot\,\mathrm{s} = 6.582 \cdot 10^{-16}\,\mathrm{eV}\cdot\,\mathrm{s} \tag{21}$$

$$e = 1.602 \cdot 10^{-19}\,\mathrm{C} \tag{22}$$

References

[1] S. König, W. Pfeiffer, T. Bayerl, D. Richter, and E. Sackmann, *Journal de Physique II* **2**, 1589 (1992).

[2] National Institute of Standards and Technology, "Neutron scattering lengths and cross sections" (1992) http://www.ncnr.nist.gov/resources/n-lengths/list.html.

[3] L. C. Pardo Soto, S. Busch, and F. Kargl: "FRIDA online manual" (2008) http://iffwww.iff.kfa-juelich.de/~wuttke/doku/doku.php?id=frida:frida1:frida-1.

[4] C. Smuda, G. Gemmecker, and T. Unruh, *Journal of Chemical Physics* **128**, 194502 (2008).

[5] T. Unruh, Jürgen Neuhaus, and Winfried Petry, *Nucl. Instrum. Methods Phys. Res. A* **580**, 1414 (2007).

[6] J. Wuttke and F. Kargl, "FRIDA data analysis version 1.2" (2006) http://sourceforge.net/projects/frida.

Contact

TOFTOF

Phone: 089/289-14881
Web: http://www.frm2.tum.de/wissenschaftliche-nutzung/spektrometrie/toftof/index.html

Giovanna Simeoni

Forschungsneutronenquelle Heinz Maier-Leibnitz (FRM II)
und Physik Department E13
Technische Universität München
Phone: 089/289-14975
e-Mail: giovanna.simeoni@frm2.tum.de

Humphrey Morhenn

Phone: 089/289-14969
e-Mail: hmorhenn@frm2.tum.de

1. **Soft Matter**
   From Synthetic to Biological Materials
   Lecture manuscripts of the 39th IFF Spring School March 3 – 14, 2008
   Jülich, Germany
   edited by J.K.G. Dhont, G. Gompper, G. Nägele, D. Richter, R.G. Winkler (2008),
   c. 1000 pages
   ISBN: 978-3-89336-517-3

2. **Structural analysis of diblock copolymer nanotemplates using grazing incidence scattering**
   by D. Korolkov (2008), III, 167 pages
   ISBN: 978-3-89336-522-7

3. **Thermal Nonequilibrium**
   Thermal forces in fluid mixtures
   Lecture Notes of the 8th International Meeting on Thermodiffusion,
   9 – 13 June 2008, Bonn, Germany
   edited by S. Wiegand, W. Köhler (2008), 300 pages
   ISBN: 978-3-89336-523-4

4. **Synthesis of CMR manganites and ordering phenomena in complex transition metal oxides**
   by H. Li (2008), IV, 176 pages
   ISBN: 978-3-89336-527-2

5. **Neutron Scattering**
   Lectures of the JCNS Laboratory Course held at the Forschungszentrum Jülich and the research reactor FRM II of TU Munich
   edited by R. Zorn, Th. Brückel, D. Richter (2008), ca. 500 pages
   ISBN: 978-3-89336-532-6

6. **Ultrafast Magnetization Dynamics**
   by S. Woodford (2008), 130 pages
   ISBN: 978-3-89336-536-4

7. **Role of Surface Roughness inTribology: from Atomic to Macroscopic Scale**
   by C. Yang (2008), VII, 166 pages
   ISBN: 978-3-89336-537-1

8. **Strahl- und Spindynamik von Hadronenstrahlen in Mittelenergie-Ringbeschleunigern**
   von A. Lehrach (2008), II, 171 Seiten
   ISBN: 978-3-89336-548-7

9. **Phase Behaviour of Proteins and Colloid-Polymer Mixtures**
   by C. Gögelein (2008), II, 147 pages
   ISBN: 978-3-89336-555-5

10. **Spintronics – From GMR to Quantum Information**
    Lecture Notes of the 40th IFF Spring School March 9 – 20, 2009
    Jülich, Germany
    edited by St. Blügel, D. Bürgler, M. Morgenstern, C. M. Schneider,
    R. Waser (2009), c. 1000 pages
    ISBN: 978-3-89336-559-3

11. **ANKE / PAX Workshop on SPIN Physics**
    JINR, Dubna, Russia / June 22. – 26, 2009
    Org. Committee: A. Kacharava, V. Komarov, A. Kulikov, P. Lenisa, R. Rathmann,
    H. Ströher (2009), CD-ROM
    ISBN: 978-3-89336-586-9

12. **Entwicklung einer Nanotechnologie-Plattform für die Herstellung Crossbar-basierter Speicherarchitekturen**
    von M. Meier (2009), 135 Seiten
    ISBN: 978-3-89336-598-2

13. **Electronic Oxides –**
    Correlation Phenomena, Exotic Phases and Novel Functionalities
    Lecture Notes of the 41st IFF Spring School March 8 – 19, 2010
    Jülich, Germany
    edited by St. Blügel, T. Brückel, R. Waser, C.M. Schneider (2010), ca. 1000 pages
    ISBN: 978-3-89336-609-5

14. **4th Georgian-German School and Workshop in Basic Science**
    Tbilisi, Georgia / May 3 – 7, 2010
    Org. Committee: E. Abrosimova, R. Botchorishvili, A. Kacharava, M. Nioradze,
    A. Prangishvili, H. Ströher (2010); CD-ROM
    ISBN: 978-3-89336-629-3

15. **Neutron Scattering**
    Lectures of the JCNS Laboratory Course held at Forschungszentrum Jülich and the research reactor FRM II of TU Munich
    edited by Th. Brückel, G. Heger, D. Richter, G. Roth and R. Zorn (2010),
    ca 350 pages
    ISBN: 978-3-89336-635-4

16. **Ab *initio* investigations of magnetic properties of ultrathin transition-metal films on *4d* substrates**
    by A. Al-Zubi (2010), II, 143 pages
    ISBN: 978-3-89336-641-5

17. **Investigation of a metal-organic interface realization and understanding of a molecular switch**
    by O. Neucheva (2010), 134 pages
    ISBN: 978-3-89336-650-7

18. **Reine Spinströme in lateralen Spinventilen, *in situ* Erzeugung und Nachweis**
von J. Mennig (2010), V, 95 Seiten
ISBN: 978-3-89336-684-2

19. **Nanoimprint Lithographie als Methode zur chemischen Oberflächenstrukturierung für Anwendungen in der Bioelektronik**
von S. Gilles (2010), II, 169 Seiten
ISBN: 978-3-89336-686-6

20. **Macromolecular Systems in Soft- and Living-Matter**
Lecture Notes of the 42nd IFF Spring School 2011 February 14 – 25, 2011 Jülich, Germany
edited by J. K.G. Dhont, G. Gompper, P. R.Lang, D. Richter, M. Ripoll, D. Willbold, R. Zorn (2011), ca. 1000 pages
ISBN: 978-3-89336-688-0

21. **The spin structure of magnetic nanoparticles and in magnetic nanostructures**
by S. Disch (2011), V, 342 pages
ISBN: 978-3-89336-704-7

22. **Element-selective and time-resolved magnetic investigations in the extreme ultraviolet range**
by P. Grychtol (2011), xii, 144 pages
ISBN: 978-3-89336-706-1

23. **Spin-Transfer Torque Induced Dynamics of Magnetic Vortices in Nanopillars**
by V. Sluka (2011), 121 pages
ISBN: 978-3-89336-717-7

24. **Adsorption von Phthalocyaninen auf Edelmetalloberflächen**
von I. Kröger (2011), vi, 206 Seiten
ISBN: 978-3-89336-720-7

25. **Time-Resolved Single Molecule FRET Studies on Folding/Unfolding Transitions and on Functional Conformational Changes of Phosphoglycerate Kinase**
by T. Rosenkranz (2011), III, 139 pages
ISBN: 978-3-89336-721-4

26. **NMR solution structures of the MIoK1 cyclic nucleotide-gated ion channel binding domain**
by S. Schünke (2011), VI, (getr. pag.)
ISBN: 978-3-89336-722-1

27. **Neutron Scattering**
Lectures of the JCNS Laboratory Course held at Forschungszentrum Jülich and the research reactor FRM II of TU Munich
edited by Th. Brückel, G. Heger, D. Richter, G. Roth and R. Zorn (2011), ca 350 pages
ISBN: 978-3-89336-725-2

28. **Neutron Scattering**
Experiment Manuals of the JCNS Laborator Course held at Forschungszentrum Jülich and the research reactorFRM II of TU Munich
edited by Th. Brückel, G. Heger, D. Richter, G. Roth and R. Zorn (2011), ca. 180 pages
ISBN: 978-3-89336-726-9

29. **Silicon nanowire transistor arrays for biomolecular detection**
by X.T.Vu (2011), vii, 174 pages
ISBN: 978-3-89336-739-9

30. **Interactions between parallel carbon nanotube quantum dots**
by K. Goß (2011), viii, 139 pages
ISBN: 978-3-89336-740-5

31. **Effect of spin-orbit scattering on transport properties of low-dimensional dilute alloys**
by S. Heers (2011), viii, 216 pages
ISBN: 978-3-89336-747-4

32. **Charged colloids and proteins: Structure, diffusion, and rheology**
by M. Heinen (2011), xii, 186 pages
ISBN: 978-3-89336-751-1

33. **Scattering Methods for Condensed Matter Research: Towards Novel Applications at Future Sources**
Lecture Notes of the 43rd IFF Spring School 2012
March 5 – 16, 2012 Jülich, Germany
edited by M. Angst, T. Brückel, D. Richter, R. Zorn ca. 1000 pages
ISBN: 978-3-89336-759-7

34. **Single-Site Green Function of the Dirac Equation for Full-Potential Electron Scattering**
by P. Kordt (2012), 138 pages
ISBN: 978-3-89336-760-3

35. **Time Resolved Single Molecule Fluorescence Spectroscopy on Surface Tethered and Freely Diffusing Proteins**
by D. Atta (2012), iv, 126 pages
ISBN: 978-3-89336-763-4

36. **Fabrication and Utilization of Mechanically Controllable Break Junction for Bioelectronics**
by D. Xiang (2012), 129 pages
ISBN: 978-3-89336-769-6

37. **Contact Mechanics and Friction of Elastic Solids on Hard and Rough Substrates**
by B. Lorenz (2012), iv, 121 pages
ISBN: 978-3-89336-779-5

38. **Ab initio Calculations of Spin-Wave Excitation Spectra from Time-Dependent Density-Functional Theory**
by M. Niesert (2012), 146 pages
ISBN: 978-3-89336-786-3

39. **Neutron Scattering**
Lectures of the JCNS Laboratory Course held at Forschungszentrum Jülich and the research reactor FRM II of TU Munich
edited by Th. Brückel, G. Heger, D. Richter, G. Roth and R. Zorn (2012),
ca 350 pages
ISBN: 978-3-89336-789-4

40. **Neutron Scattering**
Experiment Manuals of the JCNS Laborator Course held at Forschungszentrum Jülich and the research reactorFRM II of TU Munich
edited by Th. Brückel, G. Heger, D. Richter, G. Roth and R. Zorn (2012),
ca. 175 pages
ISBN: 978-3-89336-790-0

Schlüsseltechnologien / Key Technologies
Band / Volume 40
ISBN 978-3-89336-790-0